January 2015

Establishing Repeatable Operation of a Centrifugal Compressor Research Facility for Aerodynamic Investigations

Matthew Dolan
Purdue University

Recommended Citation

Dolan, Matthew, "Establishing Repeatable Operation of a Centrifugal Compressor Research Facility for Aerodynamic Investigations" (2015). *Open Access Theses*. 1105.
https://docs.lib.purdue.edu/open_access_theses/1105

PURDUE UNIVERSITY
GRADUATE SCHOOL
Thesis/Dissertation Acceptance

This is to certify that the thesis/dissertation prepared

By Matthew Dolan

Entitled

ESTABLISHING REPEATABLE OPERATION OF A CENTRIFUGAL COMPRESSOR RESEARCH FACILITY FOR AERODYNAMIC INVESTIGATIONS

For the degree of Master of Science in Mechanical Engineering

Is approved by the final examining committee:

Nicole Key
Chair

Steven Wereley

Sameer Naik

To the best of my knowledge and as understood by the student in the Thesis/Dissertation Agreement, Publication Delay, and Certification Disclaimer (Graduate School Form 32), this thesis/dissertation adheres to the provisions of Purdue University's "Policy of Integrity in Research" and the use of copyright material.

Approved by Major Professor(s): Nicole Key

Approved by: Ganesh Subbarayan 6/30/2015
Head of the Departmental Graduate Program Date

ESTABLISHING REPEATABLE OPERATION OF A CENTRIFUGAL COMPRESSOR RESEARCH FACILITY FOR AERODYNAMIC INVESTIGATIONS

A Thesis
Submitted to the Faculty
of
Purdue University
by
Matthew Philip Dolan

In Partial Fulfillment of the
Requirements for the Degree
of
Master of Science in Mechanical Engineering

August 2015
Purdue University
West Lafayette, Indiana

ACKNOWLEDGMENTS

First, I am so thankful grateful for the opportunity Prof. Nicole Key has given me and for her support, leadership, and understanding throughout my years. Her vision for lab is a unique one and I'm very appreciative for the chance to have been a part of it. John Fabian also deserves a huge thanks for his daily guidance since I started and ability to calm me down during the stressful weeks. I would also like to thank everyone at Rolls-Royce involved with this project for their wisdom, insight, and sponsorship. Mark Whitlock especially has been a huge support. I am so thankful for Rob McGuire and feel incredibly lucky to have learned from him. I am also incredibly thankful to Reid, Natalie, Lou, Bill, Dave, Nick, Nyansafo, Trey, and James for all being amazing labmates. Their daily support, friendship, and unending humor made this lab a family, one that I'm going to miss. Special thanks to Bryce and Jeanne, the best climbers I know, for being my teammates. Our fun exploits to the conversations about anything have convinced me that I've had two of the best teammates ever. My parents Kim and Maurice and brother Michael have been huge sources of support. I can't express how much they mean to me and how much they contributed to my success. A huge thanks to my friends John, Katie Y., Theresa, and RJ, for their encouragement, patience, and our amazing experiences. Finally, I want to thank Katie C. At the end of the day, when I would just curl into a ball, she would curl around me and tell me it will be alright. I can't thank her enough.

TABLE OF CONTENTS

LIST OF TABLES

LIST OF FIGURES

Figure Page

NOMENCLATURE

Symbol	**Description**
2D	Two Dimensional
3D	Three Dimensional
AC	Alternating Current
ASME	American Society of Mechanical Engineers
CAD	Computer-Aided Design
CFD	Computational Fluid Dynamics
CMM	Coordinate-Measuring Machine
CSTAR	Centrifugal STage Aerodynamic Research
CSV	Comma Separated Values
d	Diameter
DC	Direct Current
h	Enthalpy
hp	Horsepower
hz	Hertz
inH2O	Pressure Unit, Inches of Water
LDV	Laser Doppler Velocimetry
m	Mass
$\dot{m}$	Mass Flow Rate
N	Rotational Speed
P	Pressure
psia	Pressure Unit Pounds per Square Inch, Absolute

Symbol	**Description**
psig	Pressure Unit Pounds per Square Inch, Gage
PTC	Performance Test Code
PVC	Polyvinyl Chloride
Rc	Pressure Ratio
Re	Reynolds Number
RH	Relative Humidity
RPM	Revolutions per Minute
RTD	Resistance Thermometer
V	volts
v	Velocity

Greek

β	Ratio of Venturi’s Throat to Inlet Diameters
γ	Ratio of Specific Heats
ε	Expansibility Factor
η	Efficiency
μ	Viscosity
ρ	Density

Subscript

act	Actual
c	Corrected
mech	Mechanical
o	Total
ref	Reference

Subscript

s	Isentropic
t	Venturi Throat

ABSTRACT

Dolan, Matthew P. M.S.M.E., Purdue University, August 2015. Establishing Repeatable Operation of a Centrifugal Compressor Research Facility for Aerodynamic Investigations. Major Professor: Dr. Nicole L. Key, School of Mechanical Engineering.

The objective of this research has been to analyze the steady state performance of a new centrifugal compressor research facility. The CSTAR (Centrifugal STage for Aerodynamic Research) compressor has been designed to be placed as the last stage in an axial compressor and its performance in this flow regime was measured.

Because the compressor was designed as a research vehicle, unique instrumentation throughout the flow path provides a detailed look at its steady state performance. Rakes at the inlet and deswirl section quantify the overall performance but other instrumentation is used to understand the component performance. Static pressure taps along the shroud, within the diffuser, and through the turn-to-axial show the static pressure rise. Additionally, rakes at the inlet and exit of diffuser also characterize the performance of the wedge diffuser and the impeller.

Additionally, capacitance probes located at the knee and exducer of the impeller non-intrusively measure the size of the tip clearance during facility operation. An investigation into these measurements resulted in a standard procedure for in-situ calibration and installation to produce repeatable and accurate clearance measurements. Finally, the feasibility of future Laser Doppler Velocimetry measurements acquired through the shroud window was tested and was found to be achievable with the use of beam translators to ensure that measurement volumes are created after beam refraction through the windows.

Inlet conditions of the facility have been investigated and fluctuations of the ambient conditions have been mitigated with a large settling chamber to ensure repeatable and stable operation. The current instrumentation was utilized to determine the compressor performance. Measurements of the steady performance parameters along with those of the internal flow field are documented.

CHAPTER 1: INTRODUCTION

1.1 Motivation

Compressors play an integral role in today's aviation and power generation industry. Utilized across many fields, they are common in a wide variety of applications including jet engines, automotive engines, ship propulsion, gas distribution, and air conditioning. Because of their prevalent use, it has become increasingly important to increase operating efficiency and optimize performance. Higher efficiencies are being sought along with higher power-to-weight ratios. Due to the complex aerodynamics governing the compressor flow field, these results are not easy to achieve.

Computational models of the flow field are used to achieve improved designs. However, experimental studies in compressor aerodynamics are required to develop and validate higher fidelity models.

1.2 Centrifugal Compressor Components and Performance

Centrifugal compressors consist of four main flow sections: the inlet, impeller, diffuser, and collector, shown in Figure 1.1 [1]. The inlet is the entrance region to the compressor and typically conditions the flow for the downstream components. Sometimes stationary vanes are placed here to remove swirl from the flow since a uniform flow profile is ideal. Work by Brasz [2] shows a negative effect of these inlet guide vanes (IGV) on compressor efficiency. Off-design conditions show additional total pressure loss through the IGV but also additional losses outside of this region.

The impeller is comprised of a rotating set of blades that impart energy to the flow and increase the pressure of the fluid. A centrifugal compressor also turns the flow also radially allowing a pressure rise to be accomplished through centrifugal effects. The centrifugal effects provide a more significant pressure rise in a single stage compared to an axial stage which can only impart pressure rise due to diffusion. Studies by Echart [3] reveal the complex flows that develop through this region. Velocity profiles within the impeller show uniform inlet profiles develop a different shape at the knee where the flow beings to turn more radially. A large separation region begins at the shroud on the suction surface of the blade which develops as the air flows downstream. This is characterized by low velocities in this region and high fluctuations of the unsteady measurements. Earlier work by him in [4] also revealed this jet wake phenomenon, illustrated in [5], Figure 1.2. The jet/wake condition is characterized by this low velocity region, the wake, on the suction surface of the blade and a high velocity, low total pressure loss region, the jet, on the pressure side of the blade. Krain [6] also finds a similar flow pattern jet/wake flow pattern developing within the flow passage. Results also show that this dominating flow effect experiences little variation in the flow profile caused by upstream potential fields of the diffuser. Though impellers can be covered with a rotating outer casing, they are typically covered by a stationary one called a shroud because of the performance advantages associated with this design [7].

Following the impeller is a set of stationary vanes called the diffuser. The diffuser is used to transform some of the large dynamic pressure exiting the impeller to static pressure and increase the overall pressure ratio of the compressor. With a radial outflow from the impeller, the flow will naturally decelerate as it continues in this direction due to the increasing exit area and mass conservation. Though this configuration, referred to as a vaneless diffuser, is sometimes used, it is optimal in aerospace designs to include diffuser vanes to achieve more static pressure rise in a smaller diameter [8]. Work by Skoch [9] provides insight on the flow development within the diffuser. Regions of high total pressure are experienced in the mid-passage of the diffuser exit, indicating lower losses than those by the vanes. Significant losses are also seen especially on the suction side, hub region of the vane. Measurements of the flow angle conclude the same results as the total pressure measurements. The mid-passage flow experiences less swirl and an increased radial velocity compared to those at the endwall regions. High swirl is seen at the shroud where large flow angles reveal a thin region of separation. This separation area becomes more pronounced near stall and extends further down into the passage.

Finally, at the exit of the diffuser, flow gets routed to a collector or scroll. The collector gathers all of the compressed fluid and allows it to settle prior to the next stage in the system.

Performance maps are experimentally determined to verify compressor performance. Figure 1.3 [10] shows a sample map where the compressor total pressure ratio versus mass flow rate is plotted for several speed lines. The compressor speed lines show the pressure ratio as a function of mass flow at a constant speed. To acquire these characteristics, the back pressure of the compressor is increased while maintaining the compressor speed, causing the machine to load up toward the stall/surge line. The vertical potion of the characteristic where the compressor mass flow rate does not change with backpressure represents choked flow. The surge line shows the minimum mass flow rate below which stable operation is no longer possible. Using corrected rotational speed and corrected mass flow rate allows for data acquired on days with different inlet conditions to collapse to the same total pressure ratio and efficiency on the compressor map

1.3 Effects of Tip Clearance on Centrifugal Compressor Performance

In the design of modern day compressors, the impeller tip clearance plays a large role in the overall performance. The tip gap allows the high pressure fluid from the pressure side of the blades to pass through the gap to the suction side of the next blade. Extensive research has been performed to understand the effect of this phenomenon on compressor performance since it is a significant source of loss in efficiency and stall margin.

An analytic approach to quantify the effect of tip clearance on compressor performance was taken by Senoo and Ishida [11] where the pressure loss due to tip leakage flow is estimated. The model is based on the principle that as blades are loaded by curvature, the tangential fluid velocity closer to the center of the curve is smaller than that on the outer edge. Because of the pressure differential caused by the gradient of velocities across the channel, drag is induced proportional to the flow rate and the velocity difference between the suction side and pressure side. Tip leakage allows fluid to flow into the channel at the blade surfaces, thus effecting the velocity gradient and the accompanying drag force. The blades are also loaded by the rotation of the impeller, also causing drag related to the flowrate and the difference in velocities. Blade spacing also influences drag, the effect of which is proportional to the blade angle, number of blades, tangential velocity, and flowrate. Combining the effect of these phenomena, the power loss through the compressor per unit length can be found and an equation for the fluid momentum loss derived.

In the tip clearance annulus, the unfavorable pressure gradient across the blades results in fluid passing between passages and an accompanying pressure loss. In this region, inefficiencies are caused because the blade shear force must make up for the fact that there is no surface to rotate the fluid. This results in a power loss related to the shear force estimated at the blade tip with a circumferential velocity equal to that of the fluid in the passage. The drag and additional shear losses affect the work input coefficient and this prediction estimates a linear reduction in compressor efficiency with the ratio of tip clearance-to-blade height. Using a quasi-three dimensional flow analysis, values of the blade pressures and the velocities can be estimated and the derived equation used to estimate the pressure and efficiency loss due to tip clearance.

This analytic approach to determine the effect of tip clearance was initially compared with the results from two impellers where the tip clearance could be altered by axially moving the shroud. Using the derived equations at the measured compressor conditions, the efficiency drop as a function of the tip clearance was compared to the experimental data and is shown in Figure 1.4. The first impeller with more complex geometry does not match the predicted response but shows a reduced effect at larger tip clearances. The second impeller, which featured simpler geometry, agreed well with the derived equations and followed the same linear trend for three different flow conditions. Additional experimentation by Skoch [12] agrees with the linear loss model derived, though it is clear that this performance degradation is hardly always linear.

Despite this rigorous analytical approach, experimental results are crucial to understanding the aerodynamics effects of tip leakage on compressor efficiency. The effects of tip clearance have also shown a large effect or the surge and stall characteristics which is difficult to predict analytically. Changes in compressor stability were noted through experiments by Eisenlohr and Chladek [13]. As tip clearance increases, the surge margin of the compressor increases due to the change in the aerodynamics. At lower clearances, a reduced total pressure loss results in an increase in the passage velocity and flow direction. The higher momentum flow is accelerated more radially, decreasing swirl and changing the incidence angle on the vaned diffuser. For higher tip clearances, lower mass flows are required to reach the flow angle associated with stall, increasing the stall margin. In addition to the passive control of stall margin, active control of surge was studied by Sanadgol [14] by modulating the tip clearance in real time to dampen surge.

Work by Brasz [15] was performed on a 7060 RPM centrifugal compressor to experimentally characterize tip leakage effects on performance. To vary the clearance of the machine, shims were used to axially shift the shroud. Three equally spaced weld rods acted as rub pins during testing and were used to determine the running tip clearances over the impeller. As expected, experimental compressor performance declined with increasing tip clearance due to the increased loss but experienced an increase in surge margin. Trends show nonlinearities where, at lower clearance ratios, the effect of increased tip gap is larger. These results disagree with the loss model developed by Senoo and Ishida [16] that suggested a linear loss relationship with clearance ratio but show the same trends as the first impeller of that study. The results suggest an additional loss mechanism not accounted for in the analytic model. In addition to the total pressure loss caused by the tip clearance gap, the leakage flow also has an unfavorable effect associated with secondary flows. Hub and shroud secondary flows cause fluid to migrate from the pressure to the suction side of the passage, which is opposite to the tip clearance flow moving over the blade. These two opposing flows mechanisms cause a wake near the suction side of the surface that reduces the effective area of the passage.

Though tip leakage flows significantly alters the flow field within the impeller, changes in diffuser aerodynamics are also experienced. A centrifugal compressor with a 46-bladed backswept impeller was analyzed by Kunte et al. [17] to experimentally study the effects of tip clearance on diffuser performance. Three measurement techniques were used to characterize the flow. First, a pitot probe inserted at the diffuser inlet provide steady total pressure. Second, dynamic 3-component probes were used at the diffuser exit plane to provide unsteady pressures that fluctuate with each blade passing. Third, particle image velocimetry was used to capture the flow development at three different planes within the diffuser.

The nominal clearance of 0.25 mm inlet diffuser profile showed a small reduction of pressure toward the suction side of the plane but an otherwise strong total pressure profile. When the tip clearance was increased to 0.65 mm, the maximum pressure was reduced by 1.2% and a change in the pressure profile resulted. The high tip clearance indicated that the high pressure region was shifted more toward the suction side of the blade. The effect of the larger tip clearance propagated to the exit of the diffuser where the nominal profile experienced significant separation on the pressure side covering approximately half the flow path. The exit Mach profile of the increased clearance case showed higher core velocities, indicating that the diffuser was properly diffusing the flow. With the fluid moving faster, the Mach number increase by 2% and less static pressure was recovered. PIV measurements showed that the separation region moved further into the diffuser with the higher tip clearance case, leading to the higher momentum fluid in the passage. Not only did the diffuser maximum flow velocity increase, but the high speed fluid was also shifted toward the suction side of the blade. Overall, higher pressure losses and less static pressure rise indicated that the effect of tip leakage flows also negatively affects the diffuser.

Tip clearance effects on diffuser performance were also experimentally studied by Jaatinen-Varri et all [18] on a compressor utilizing a vaneless diffuser. The inlet of the diffuser showed a significant change in the velocity profiles caused by an increase in the tip clearance. At larger clearance, the influence of the tip clearance is seen on the flow angle in this region. With increasing clearance, the secondary flow region is increased and to satisfy continuity, the velocity must increase at the hub due to the decrease in effective flow area. This increased momentum at the hub causes the flow to be directed more radially. In addition, because of the increased velocities at the hub region, increasing the strain rate on the flow and thus causing higher losses. The effect of the larger tip clearance is felt even at the diffuser exit where the flow angle near the shroud is almost 10° less from the middle of the passage to the shroud. This indicates increasing tangential velocity with larger tip clearances.

Experiments by Schleer et al. [19] also studied the effect of tip clearance on instability using a single-stage centrifugal compressor with a design point pressure ratio of 2.8 featuring a backswept impeller and a vaneless diffuser. Both unsteady and steady pressure measurements along the shroud were used to analyze the stability of the compressor for two tip clearance configurations. The study showed the smaller tip clearance not only increased the pressure rise in the machine, but it also shifted the stall inception to lower mass flow rates, indicating overall better compressor performance. Stable operation shows a significant drop in static pressure at the inlet due to the initial acceleration of the fluid, but unstable flow conditions featured an increase in pressure, indicating that the fluid is not moving as quickly and is encountering a recirculation zone. The recirculation zone is a result of a flow separation at the impeller inlet in which energized fluid is moved upstream. During stable operation, the pressure rise through the machine differs significantly between the two tip clearance cases, beginning at the radial turn of the impeller, and shows a stronger growth in the smaller clearance. These increases persist through the exducer region and then increase at the same rate in the diffuser.

Unsteady pressure measurements at the inlet of the impeller showed a change in tip clearance flow trajectory as a function of loading. At high mass flow rates, trajectory was directed toward the mid passage due to the high momentum fluid entering the impeller. As the mass flow is decreased, lower velocities are experienced in the meridional plane and the tip clearance flow becomes directed at a lower angle toward the compressor inlet and the pressure surface. When this tip leakage vortex becomes parallel to the inlet plane, an inlet tip recirculation zone develops. This conclusion is indicated also by the increased steady inlet pressures. The reduced tip clearance configuration resulted in lower unsteadiness throughout the compressor flow field. Similar tip clearance trajectories were captured but at lower magnitudes. With lower tip clearances, the tip leakage flow rates became smaller and the compressor was able to perform at lower mass flow rates until the clearance vortex became parallel to the inlet plane, indicating the onset of stall.

1.4 Research Objective

The objective of this research is to quantify the performance of a high-speed centrifugal compressor and to establish repeatable operation of the facility. Designed by Rolls Royce, the Centrifugal STage for Aerodynamic Research, or CSTAR, compressor runs at a design speed of 22,500 RPM, and it has been instrumented significantly. The intrusive instrumentation provides unique access into the flowfield and accommodates for measurements in regions of the flow path that are typically difficult to access. Though intrusive instrumentation provides insight on the aerodynamics of the compressor, it can alter the flow field as shown by Hongwei [20] and Filipenco [21] Nonintrusive instrumentation is also utilized to provide measurements of the compressor's performance without affecting its flow field. The results uncover some of the complex aerodynamics present in centrifugal compressors.

Other aspects of the facility were investigated to ensure repeatable compressor operation. To consistently remain at a constant corrected speed, temperature fluctuations at the inlet were minimized, ensuring that the compressor remains at a stable operating condition. A settling chamber was used to equalize incoming air and dampen oscillations in the ambient conditions. To measure impeller tip clearances, nonintrusive capacitance probes were used and procedures for calibration and installation were established. Through the establishment of a repeatably performing facility, the compressor performance was quantified and significant insight on its aerodynamics was gained.

Initial measurements of the current configuration will provide a reference for all other future changes to the compressor geometry. Future alterations include changes to the tip clearance and diffuser geometry. It is important to have these initial baseline measurements to quantify the performance differences caused by changes to the configuration. This initial configuration has a tip clearance gap to ensure a low risk of a tip rub during this shakedown phase. After the initial performance is determined, this clearance gap can be adjusted and reduced for optimal performance to uncover differences in the flow field with varying tip clearance.

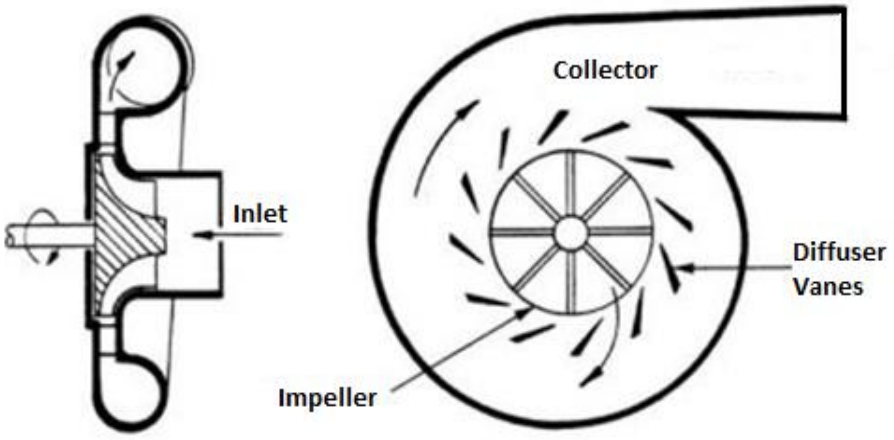

Figure 1.1: Compressor Flow Sections, [1].

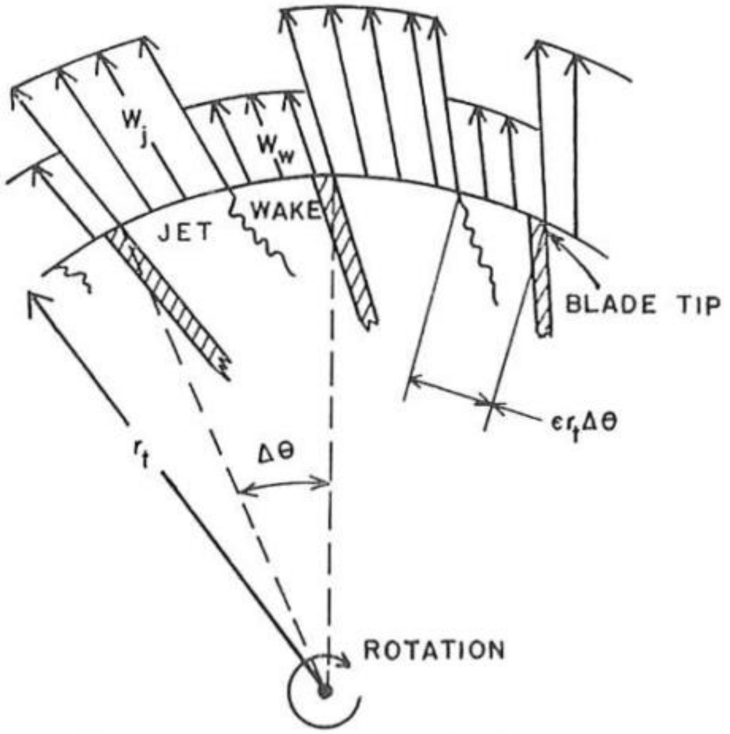

Figure 1.2 Jet/Wake Model, [5]

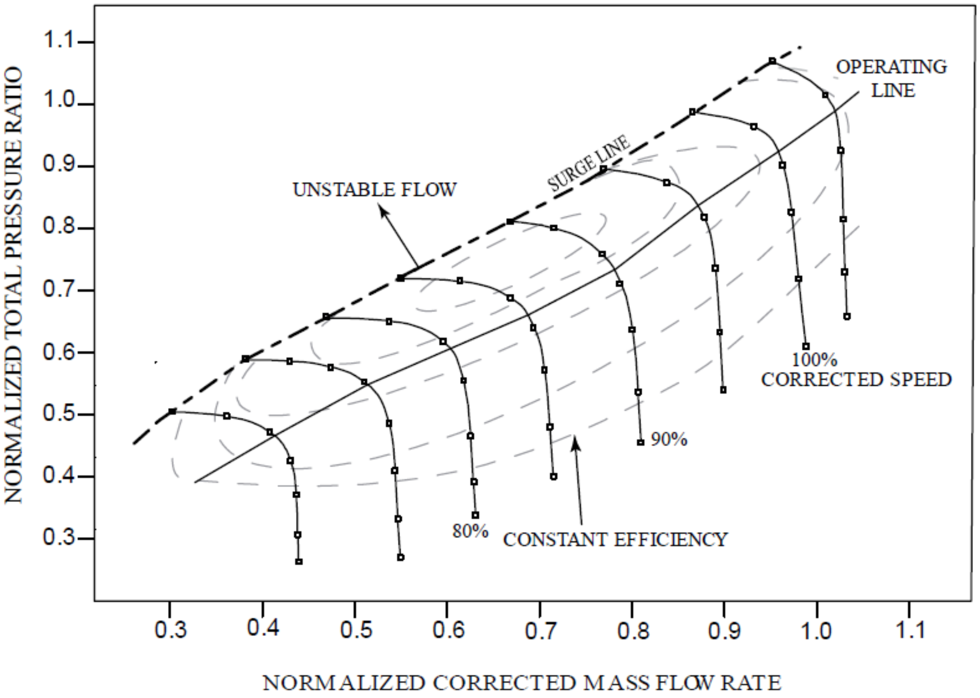

Figure 1.3: Typical Compressor Map, [10].

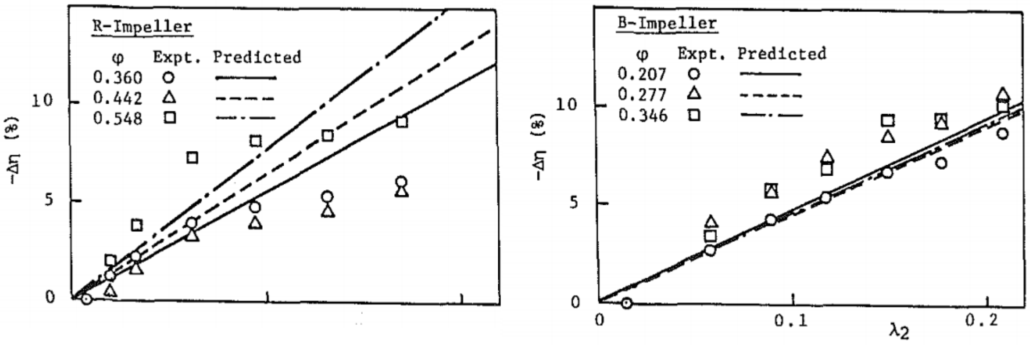

Figure 1.4: Efficiency Loss Due to Tip Leakage Effects, [11].

CHAPTER 2: CSTAR COMPRESSOR

The CSTAR research compressor is located at Zucrow Laboratory at Purdue University. The compressor and drive system are housed within a 21 by 15 foot test room with the control and data acquisition system in an adjacent room. A bedplate is used to secure the compressor and drive system and isolate vibrations from the rest of the building. An overhead view of the compressor facility is shown in Figure 2.1 along with an isometric view of the test cell in Figure 2.2 with a human figure for scale [22].

2.1 Facility Driveline

A multicomponent drive system is utilized to provide the necessary power to turn the compressor’s impeller. The main components of this driveline are a 1400 hp electric motor, a speed increasing gearbox, and the drive shaft attached directly to the compressor.

2.1.1 Motor and Gearbox

The first mechanism in the driveline is an ABB AC electric motor, shown in Figure 2.1. This motor is capable of rotating at a maximum speed of 1792 RPM and provides 1400 hp at this speed. Across the speed range, the motor provides a constant torque of 4101 ft-lbf resulting in a linear increase of motor power output with speed. A variable frequency drive powers the motor, providing a maximum of 480 VAC at full speed at a

60 Hz frequency. This drive is powered by a transformer which converts the 21000 VAC to the 480 VAC at 60 Hz to the drive system and is cooled by a water and glycol mixture. A pedestal located at the control station is used to control the motor speed to within 0.01% of the full speed range through feedback from the motor encoder.

A gearbox is used to increase the shaft speed and interface between the drive and compressor. The gearbox was manufactured by Cotta Transmission and uses three intermediate shafts to provide an overall gear ratio of 30.46:1, resulting in a maximum output shaft speed of 54,000 RPM. The low-speed gear interfaces with the drive system via a gear coupling, and the output interfaces with the compressor shaft via an internal spline. In addition to driving the compressor, the gearbox also provides structural support for the compressor. The compressor is cantilevered from a gearbox pilot surface and secured using six equally spaced bolts on the compressor drive housing flange.

2.1.2 Compressor Driveline

Figure 2.3 shows the components used to interface the gearbox and impeller. A flexible coupling transfers torque from the gearbox to the main shaft. Because it is flexible, this coupling is also capable of accommodating for slight misalignments between the main shaft and the gearbox output. Supporting the main shaft is a rear roller bearing that is connected to the drive housing. This bearing constricts radial motion of the main shaft, while allowing it to freely rotate and expand axially to compensate for contraction at high speeds. Supporting the front of the main shaft is a deep groove ball bearing that protects against shaft axial motion. Because the front of the shaft interfaces with the backface of the impeller, axial movement at this location could cause the impeller to make contact with the shroud so the forward bearing is utilized to avoid this. This front bearing is housed within a squeeze film damper cage. The squeeze film damper cage utilizes viscous damping from the supplied oil to reduce compressor vibrations in both the axial and radial directions. A thin film of oil surrounds the front bearing, and as the outer journal is moves, the fluid pressure changes accordingly and forces the journal back to the center position. This damper is located within, and supported by, the drive housing.

2.2 Flow Path and Instrumentation

2.2.1 Ambient Inlet

Outdoor ambient air is drawn through the primary inlet ducting toward the compressor shown in Figure 2.4. Air first passes through a filter material to stop particulates, as small as 7 micron, from entering the system and then passes through a 19 inch diameter bellmouth. The bellmouth ensures a uniform flow into the 8 inch inlet aluminum ducting. A United Sensor PAC-T-8-K-Kl-Mini pitot probe measures total temperature, total pressure, and static pressure at the duct inlet. This probe is situated at the duct centerline and located two pipe diameters downstream after the bellmouth to ensure that the fully developed free stream properties are measured. A hygrometer is located 5 in upstream of the pitot probe to provide relative humidity readings and it is flush-mounted with the side of the inlet ducting to reduce flow disturbances. These two instruments provide the necessary measurements to calculate the inlet air properties needed for the subsequent flow meter.

2.2.2 Venturi Flowmeter

An ASME-standard long-form venturi flowmeter is located 5 pipe diameters downstream of the hygrometer to ensure a uniform flow at its inlet. This distance is in accordance with ASME flow test measurement code PTC 14.5 [23], which has been followed for the design and installation of this flowmeter. The dimensions of the venturi are shown in Figure 2.5. As the cross-sectional area is reduced, the air is accelerated. This causes a pressure difference between the inlet and the location with the smallest radius, the throat, which can be related to the mass flow. Four equally spaced pressure taps are located around its inlet and are used to measure the upstream pressure prior to the venturi's contraction. Four additional equally spaced static taps are located at the throat and are used to determine the pressure difference caused by the contraction. Following the throat, the venturi gradually expands the air back to the ducting diameter. This expansion section is 2.4 feet long with endwalls angled at 3.5 degrees from the centerline to ensure a uniform velocity profile leaving the flow meter.

2.2.3 Inlet Plenum

The venturi is followed by another 5 foot length of 8 inch diameter piping and two 90 degree bends which are used to deliver the flow to the compressor's inlet. These bends cause secondary flows which result in a significant amount of non-uniformities at their exit. The remainder of the ducting to the inlet is dedicated to conditioning the flow to resolve these nonuniformities. This occurs in the inlet plenum, a section view of which is shown in Figure 2.6. The beginning of the plenum is used to mitigate both issues of reducing non-uniformities and expanding to the appropriate inlet diameter. A wide angle diffuser is implemented immediately after the final 90 degree bend to expand the flow as far in front of the compressor inlet as possible and allow the flowfield to become uniform. A flow spreader within the wide angle diffuser ensures the flow is uniformly distributed. This flow spreader is essentially a cone perforated with several hundred holes that separates the flow into separate stream tubes extending all the way to the outer radius of the plenum. Two sets of honeycomb screens are utilized following the spreader to further ensure a uniform profile upstream of the compressor. Two total temperature and pressure rakes positioned after the second honeycomb are used to verify to that the flow upstream of the compressor has indeed been sufficiently settled.

2.2.4 Compressor Inlet

After significant flow conditioning in the plenum, the air is delivered to the compressor. A section view of the compressor is shown Figure 2.7 and highlights the compressor’s flow path. The transition from the plenum to the compressor inlet is accomplished using the compressor’s bellmouth to ensure a smooth transition to the impeller. In addition to the reduction of the outer diameter, an inner diameter must be introduced to the flow to create an annulus to match the inlet of the impeller and this is accomplished with a nosecone.

Four sets of rakes provide the total pressure and total temperature profiles just prior to the impeller. Two total pressure rakes located at 30 degrees and 210 degrees, forward looking aft, and two total temperature rakes located at 150 degrees and 330 degrees, all with five elements, measure the inlet flow before its entrance into the impeller, Figure 2.8. One static pressure tap located at the same axial location as the rakes can be used to determine the impeller inlet Mach number distribution within the annulus. Following the rakes are two sets of static taps on the shroud, one located 0.1 in axially upstream of the impeller and the second located 0.25 in downstream of the blade leading edge, as shown in Figure 2.9. At each of these planes, three static taps located at top dead center, 120 degrees and 240 degrees show the circumferential uniformity at the inlet of the impeller.

2.2.5 Impeller

Air then enters the forward looking aft counter-clockwise rotating impeller. This impeller is comprised of 15 full blades that stretch from the inlet to the exit of the impeller and 15 splitter blades that begin at 30% of the shroud passage. Through this impeller, the flow is directed from the axial inlet to a radial exit. The design corrected speed is 22,500 RPM. The shroud governing the outer flow path can be repositioned axially by mounting a shim at its seat, as shown in Figure 2.10. An increase in shim thickness results in an axial shift forward of the shroud, opening up the tip clearance and significantly changing the flow physics in this region. This capability facilitates future testing of the effect of tip clearances on compressor performance in this compressor.

Though initial tests are performed with an estimated 0.014 in clearance, this gap is intended to be reduced to 0.005 in to improve impeller performance.

Located on the shroud are 18 static taps that are used to measure the growth of static pressure through the impeller passage, Figure 2.11. At top dead center on the shroud, these taps are located every 10% of the flow passage up to 90%. There is then one at 95% and a total of 7 at 99% of the passage, the exit of the impeller. These final 7 taps are clocked at different angles to show the average pressure distribution upstream of the diffuser. They are equally spaced to cover an entire diffuser inlet passage and their locations relative to the diffuser vanes are shown in Figure 2.12.

2.2.6 Backface Bleed

Once the air radially exits the impeller, it has two paths to travel. The first, which only allows a small amount of mass flow through, is the backface bleed path. Because the impeller, a rotating piece of machinery, must be interfaced with the stationary housing, some air will seep through to the impeller's rear face. A labyrinth seal located near the drive shaft reduces the amount of air lost through this region. The seal induces pressure losses through tight constrictions that expand to large cavities. This loss mechanism causes the necessary drop to reduce the pressure from that of the impeller backface to that of ambient, where this bleed air is ejected. To determine the pressure on this face, six static pressure taps are located within this flow section at different radii, three at 90 degree and three at 270 degrees circumferentially, forward looking aft.

Figure 2.13 shows a section view of the backface bleed path at the circumferential location of the pressure taps.

2.2.7 Diffuser

Air that does not escape through the backface bleed lines enters the diffuser region which further increases the static pressure of the air. The flow first passes through the vaneless space, which is region of transition between the rotating impeller and the stationary wedge diffuser. A wedge-shaped vane slows the flow and recovers static pressure. The diffuser region is heavily instrumented. At the leading edge of four of these vanes are sets of rakes to determine the flow stagnation properties in this region: two three-element total temperature rakes and two four element total pressure rakes, Figure 2.14. The rake elements are located within removable vane passages, shown in Figure 2.15, with both the pressure tubing and thermocouple wires routed to the outside of the shroud . By using removable cartridges, the vane passages could easily be instrumented and any changes could be performed without removing and disassembling the entire diffuser assembly. Three static pressure taps are located at the throats of two diffuser passages to characterize the flow at the inlet of the diffuser.

The exit of the diffuser is also heavily instrumented. Three static pressure taps at the exit of two passages show the distribution of static pressure across the passages. Figure 2.16 shows the outside of one of these passages, revealing the locations of the pressure taps along with the placement of the tubulations routing the pressure lines outside of the shroud. Eight of the diffuser passages are also equipped with four element total pressure exit rakes. Each rake is located at one of four relative vane passage locations. Two rakes at 11.9%, 35.7%, 59.5%, and 83.4% of the diffuser passage provide a detailed look at the diffuser exit flow parameters and can be used to determine the efficiency of the diffuser design. Though all of these rakes are located within different passages to minimize flow disturbances and blockage within a particular passage, Figure 2.17 shows a model view of the rakes' locations as if there were all in the same passage to show the relative position of the measurements.

2.2.8 Turn to Axial

Air is routed back to axial following the diffuser using a 90 degree bend. This bend is shown in Figure 2.18 and transitions the flow from the radial direction at the exit of the diffuser to the axial direction. In addition, it is used to merge air exiting from the 34 vane passages and mix the flow to provide a uniform profile at the exit. Six static pressure taps are located at one circumferential location in this passage, three along the inner wall of the turn and three along the outer wall. These taps are used to not only understand the pressure distribution within this transition zone but also to determine whether or not the flow is separating.

The axial flow begins moving through the deswirl, an annular region which is used to settle the flow and transition it to a more uniform spanwise and circumferential profile. Five total pressure rakes, with five elements each, provide the total pressure profile immediately after the turn to axial. Four total temperature rakes at the exit of this annulus determine the spanwise temperature profiles before the flow is accumulated in the collector. This instrumentation is shown in the section view of the deswirl region in Figure 2.19.

2.2.9 Exhaust

The collector is a large settling chamber for the compressed air to equalize before exhausting to ambient. Settled flow within the collector then moves upward through a six inch diameter pipe where it is then exhausted to ambient through one of two paths. The first path is through a three inch pipe that is regulated via a manual ball valve that is set prior to operation. During initial testing, the manual ball valve handle was set at 40 degrees from horizontal which allowed the compressor to easily throttle into choke as desired. The second path goes upwards, moves through a 90 degree bend and is reduced to a three inch diameter area to interface with the pneumatically actuated FieldVue Vee-Ball rotary control throttle valve. This ball valve is controlled externally through an electrical signal from the data acquisition program. It throttles the flow down to the ambient pressure and in turn increases the upstream pressure at the exit of the compressor. This allows different operating conditions along the speed line to be achieved. Flow is then diffused into a six inch diameter pipe and exhausted to ambient, where it is directed upwards so that there is no reingestion of the hot exhaust air.

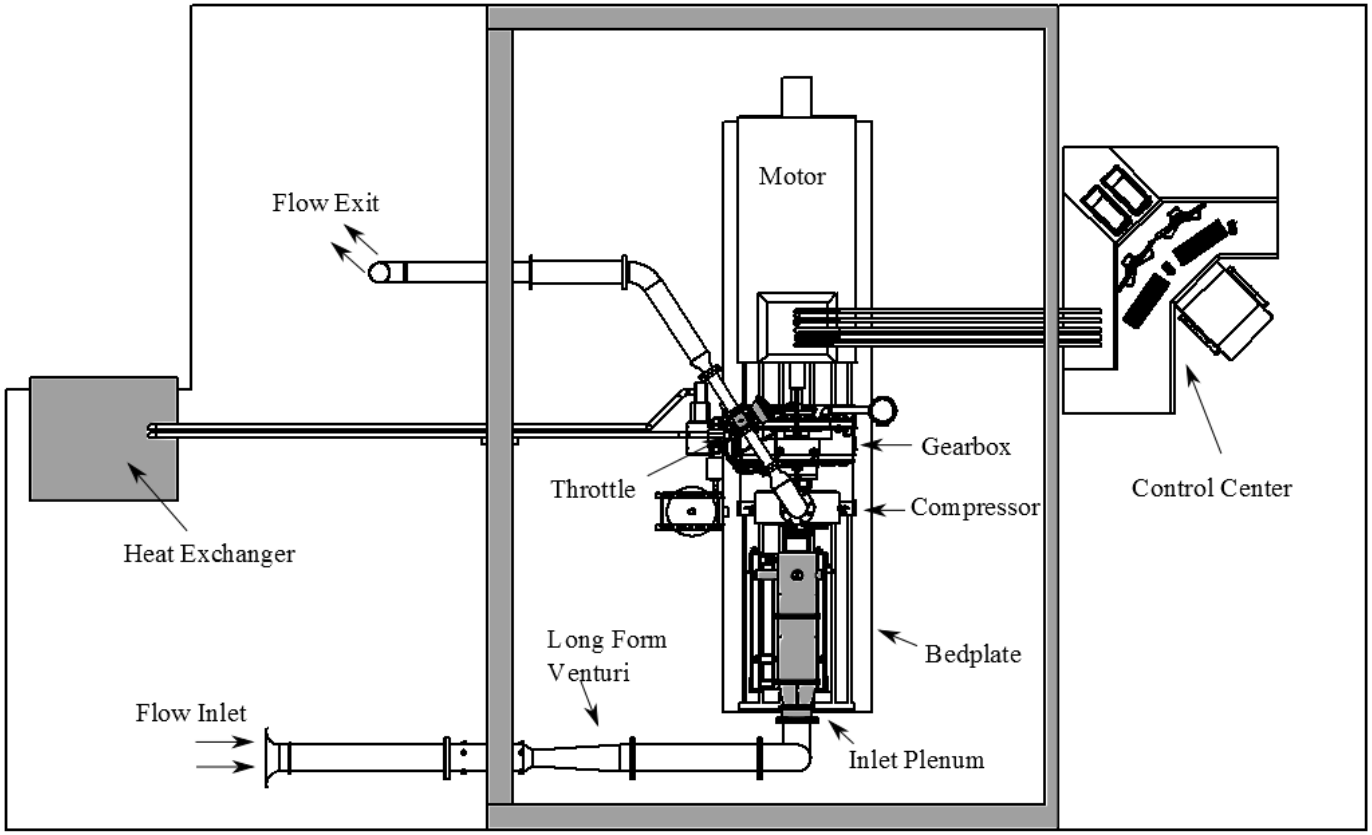

Figure 2.1: Overhead View of Compressor Facility.

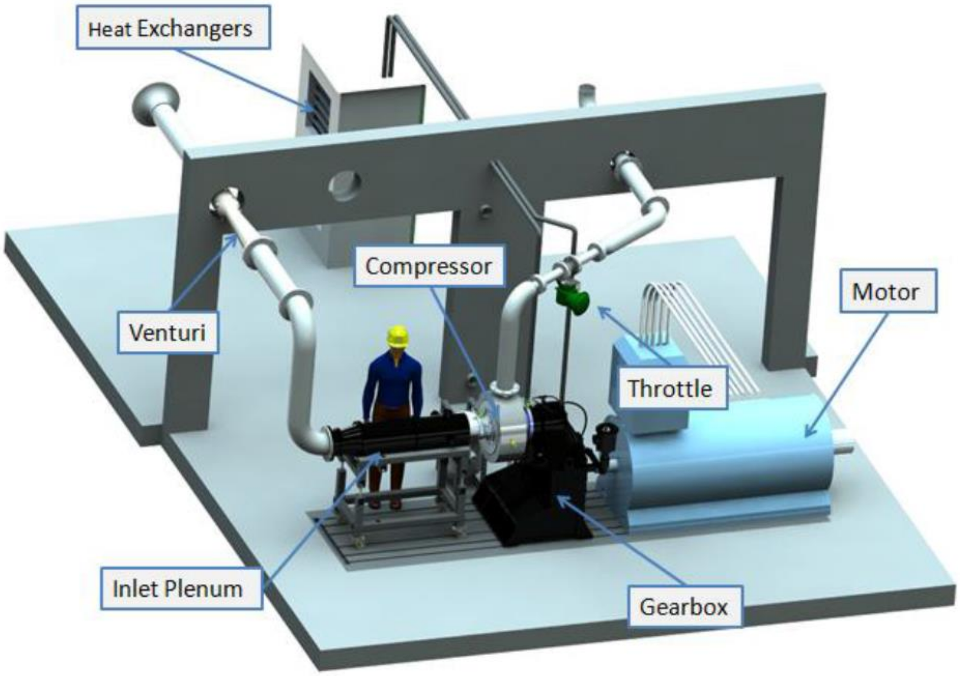

Figure 2.2: Isometric View of Compressor Facility, [22].

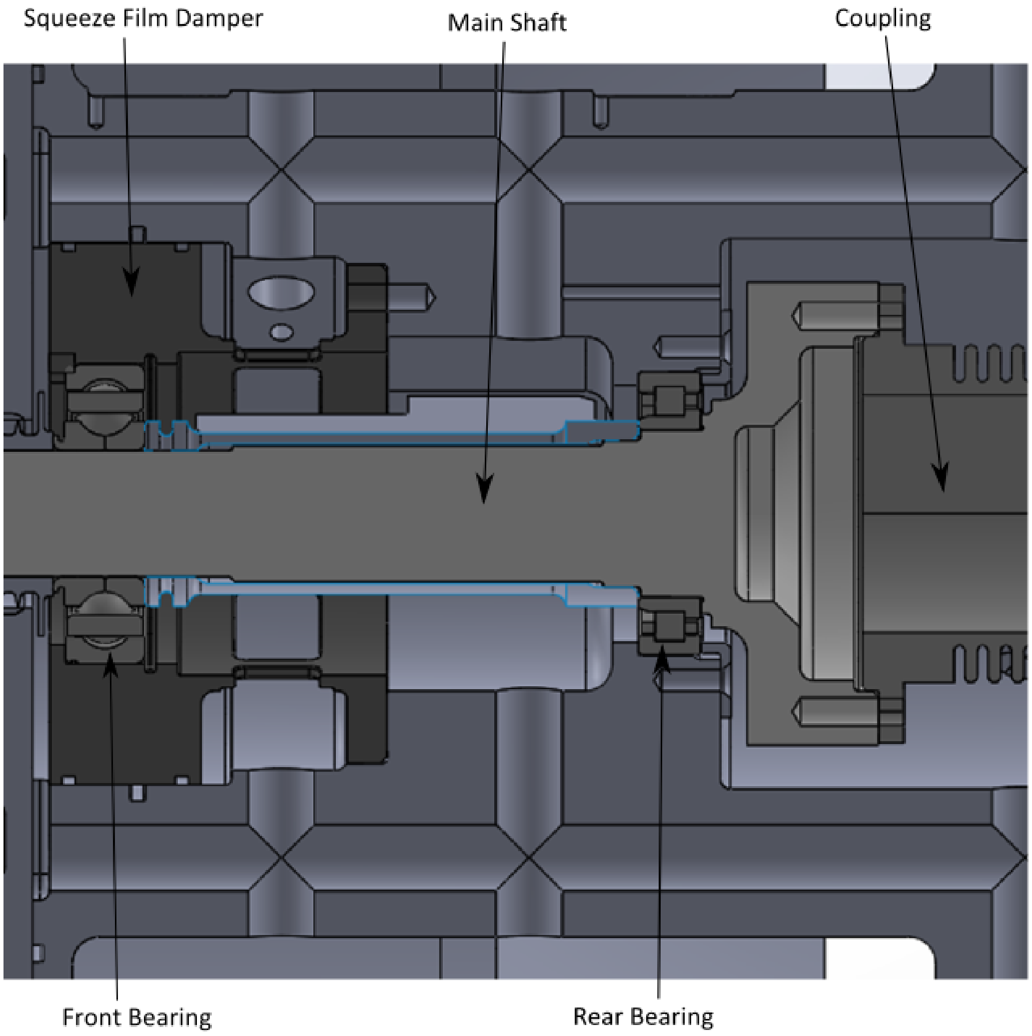

Figure 2.3: Compressor Driveline Components.

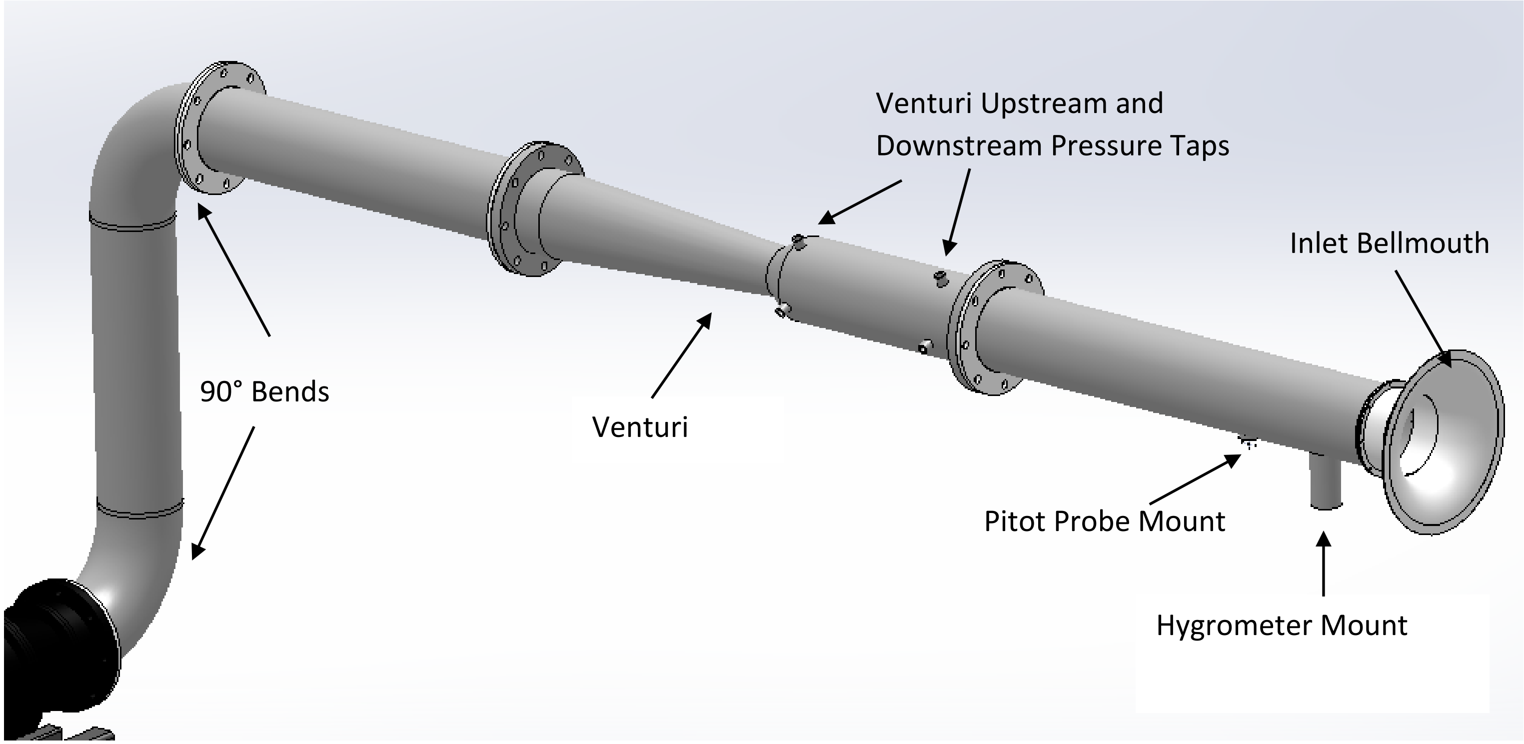

Figure 2.4: Inlet Piping.

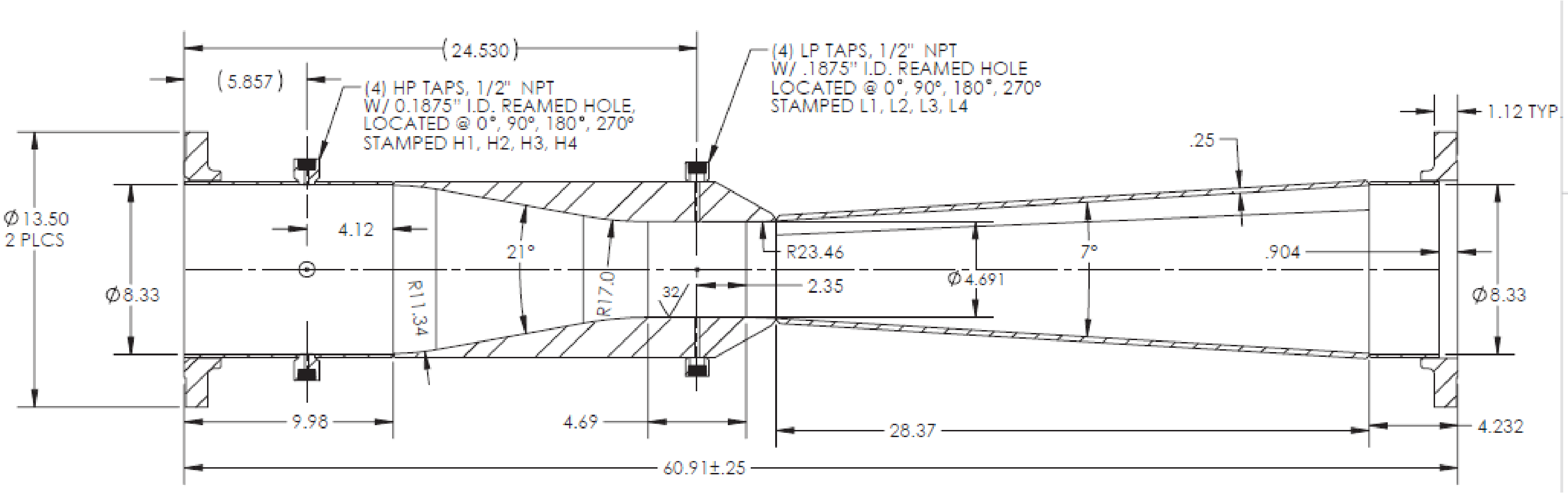

Figure 2.5: Dimensions of Long-Form Venturi Flowmeter in Inches.

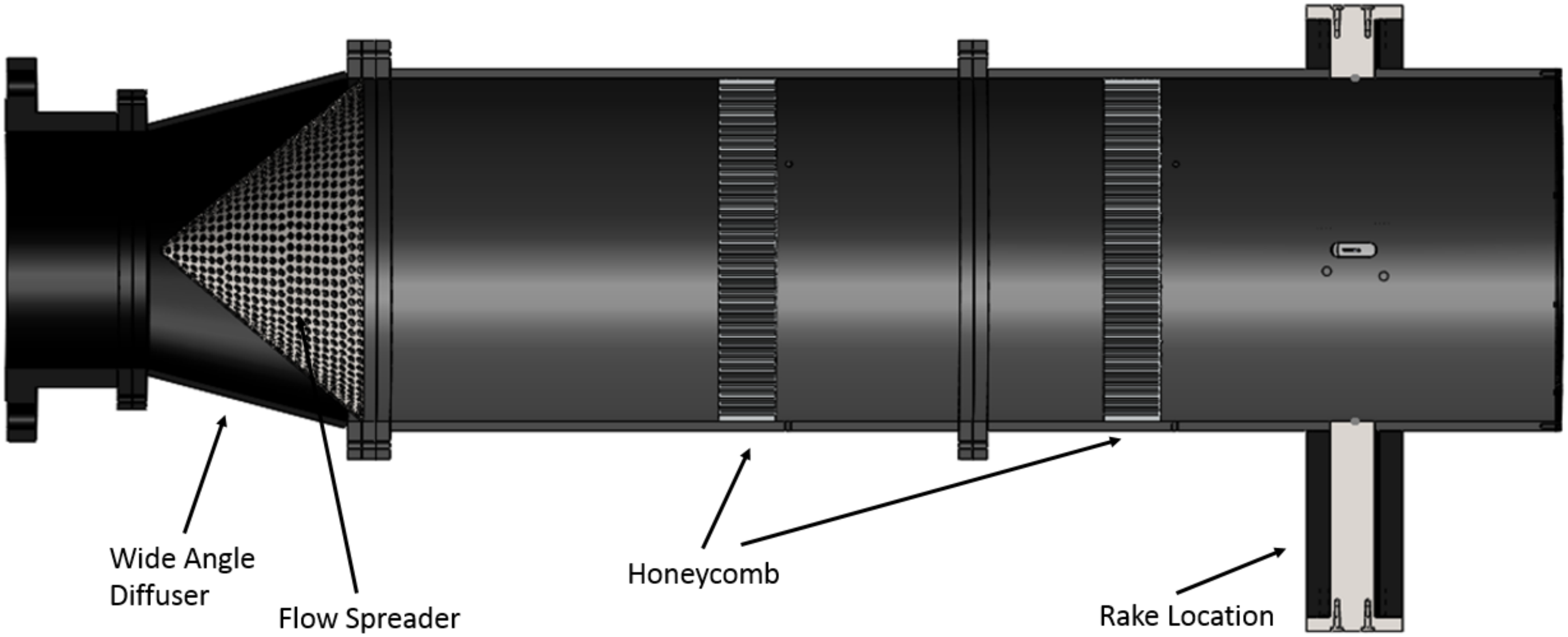

Figure 2.6: Inlet Plenum.

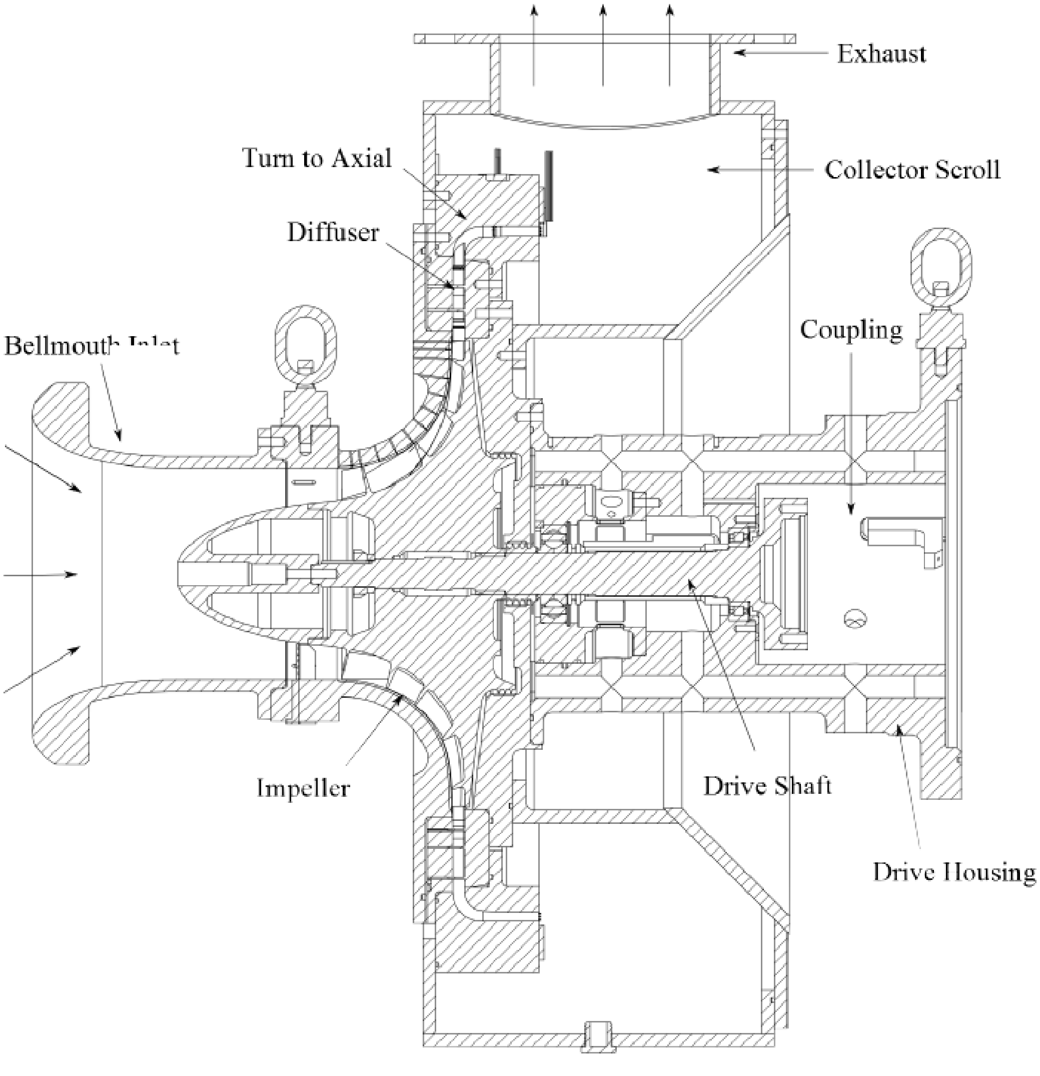

Figure 2.7: Compressor Cross Sectional View.

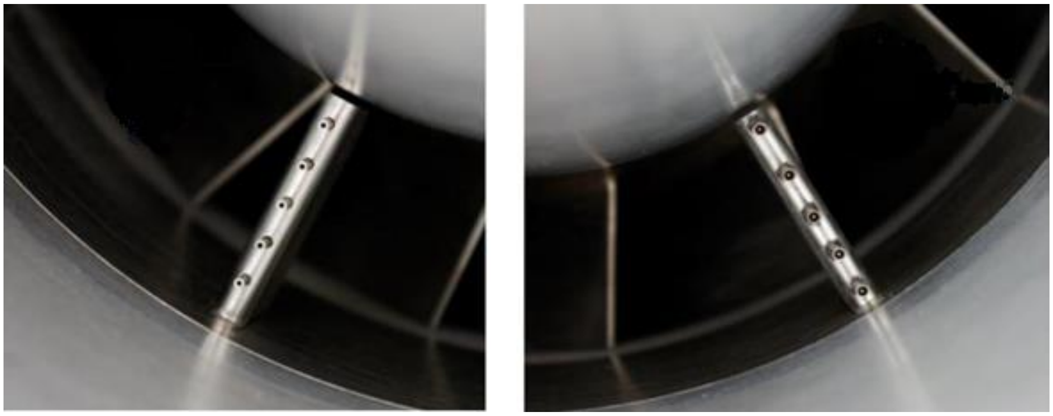

Figure 2.8: Inlet Total Pressure Rake at 210° and Inlet Total Temperature Rake 150°.

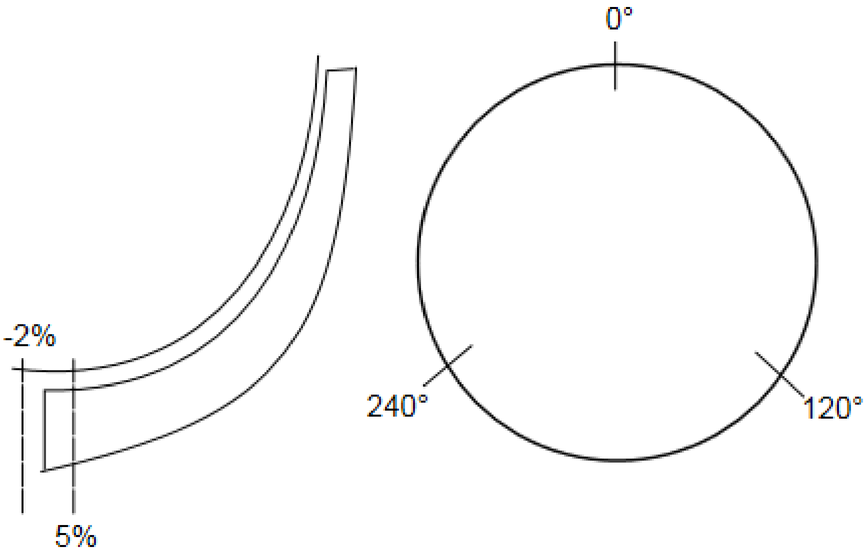

Figure 2.9: Locations of Shroud Static Taps.

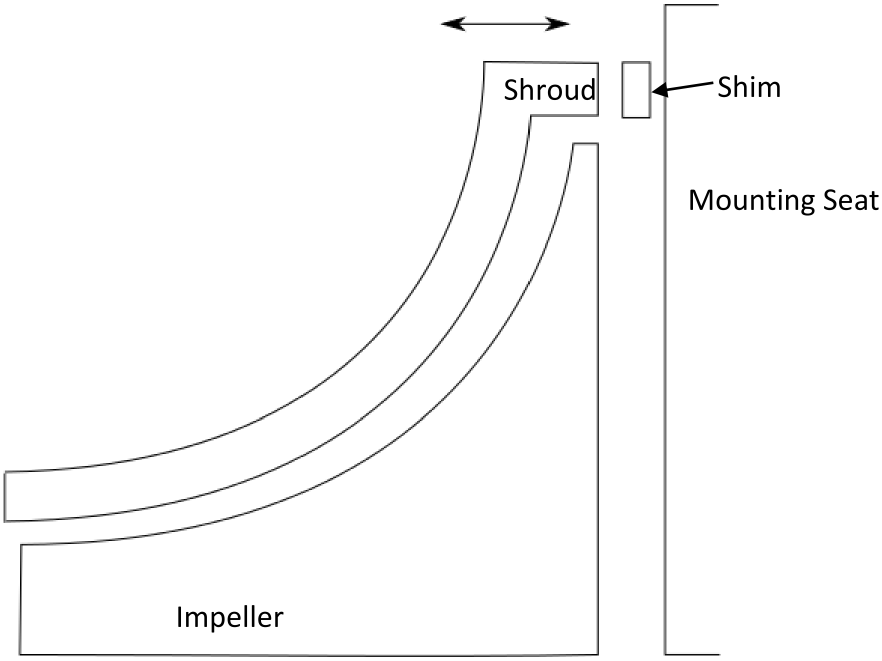

Figure 2.10: Axial Shift of the Shroud.

Figure 2.11: Shroud Static Pressures, [22].

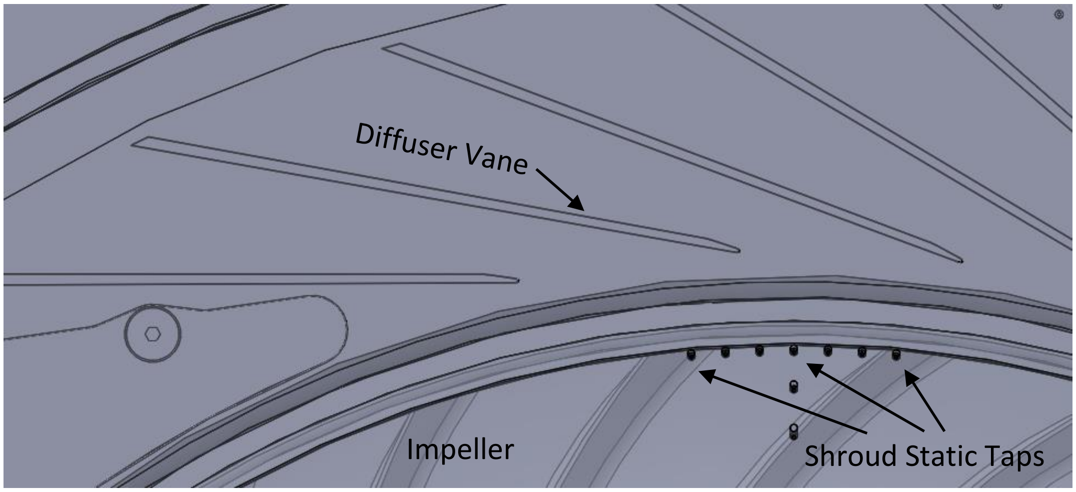

Figure 2.12: Impeller Exit Static Pressure Tap Locations Relative to the Diffuser Vanes.

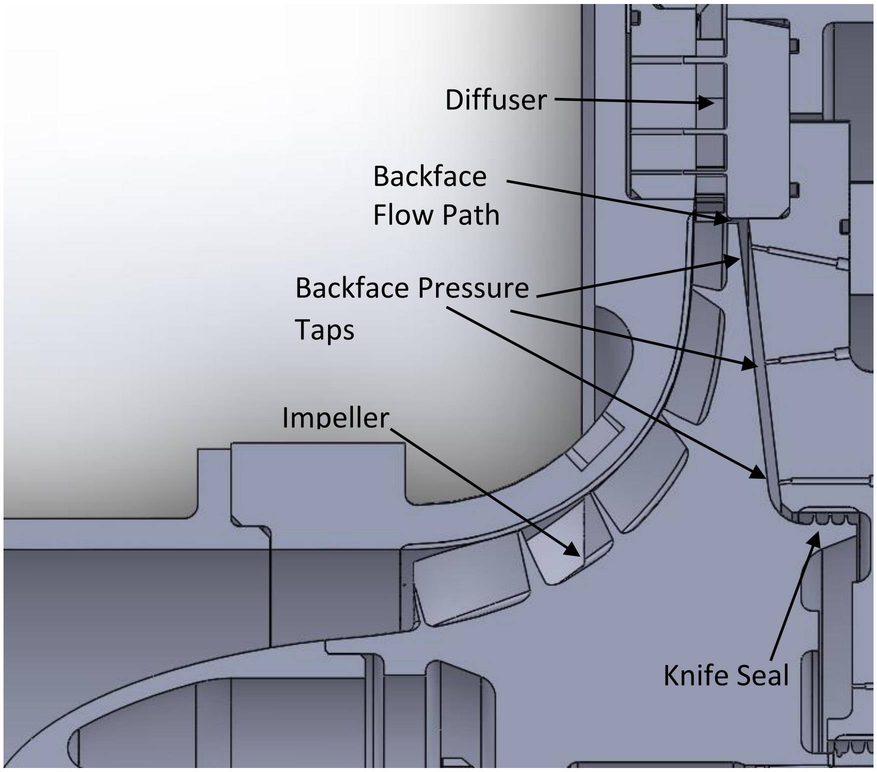

Figure 2.13: Impeller Backface Flow Path.

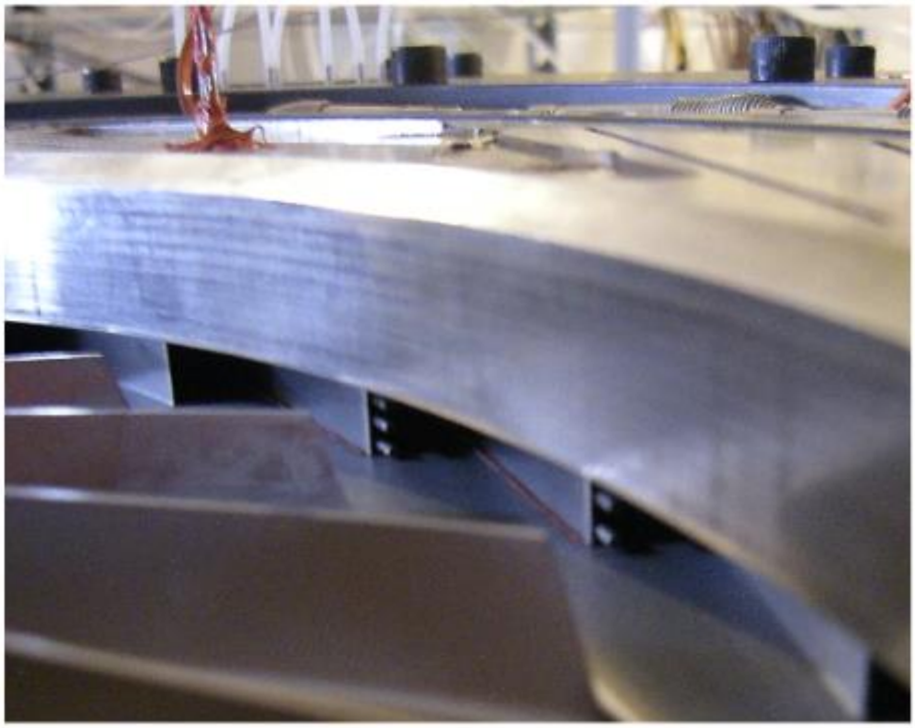

Figure 2.14: Diffuser Inlet Total Temperature and Total pressure Rakes.

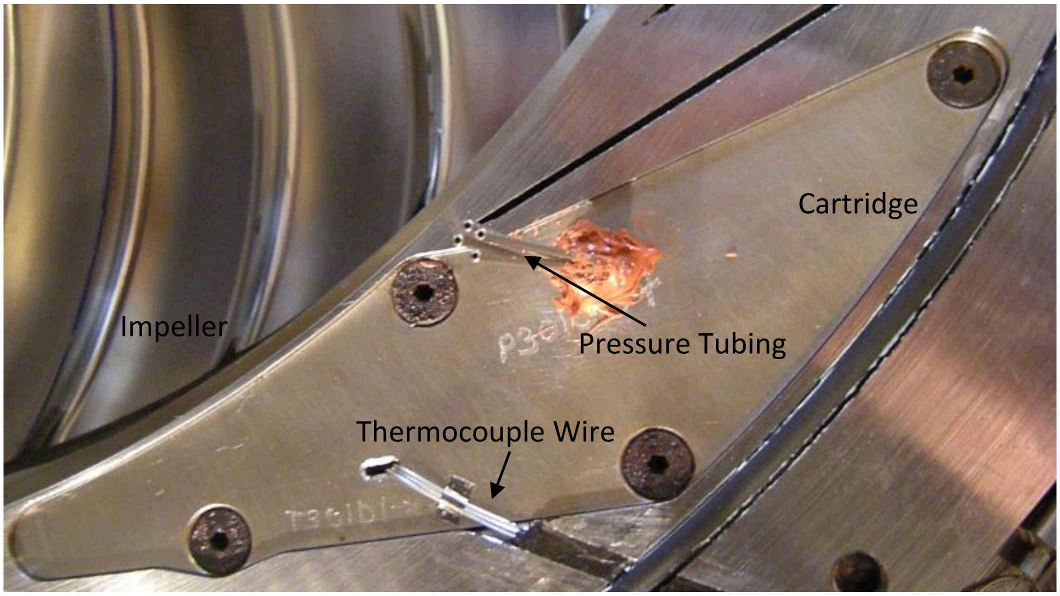

Figure 2.15: Removable Diffuser Cartridge with Rake Instrumentation.

Figure 2.16: External View of the Diffuser Vane Passage Static Taps.

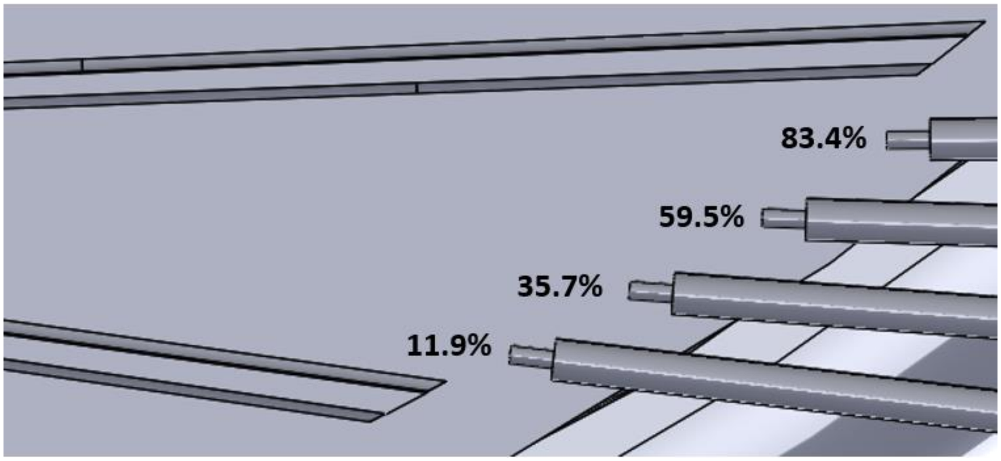

Figure 2.17: Locations of the Diffuser Exit Rakes in Percent Passage.

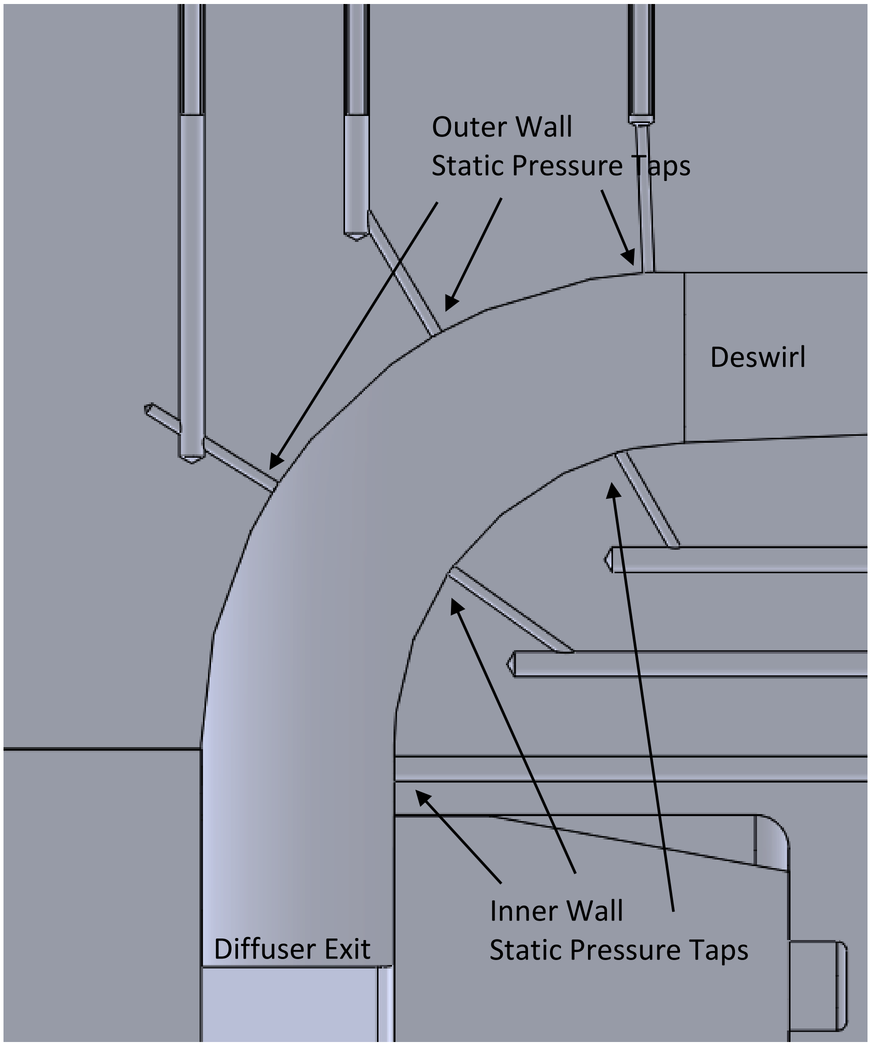

Figure 2.18: Turn to Axial Pressure Taps.

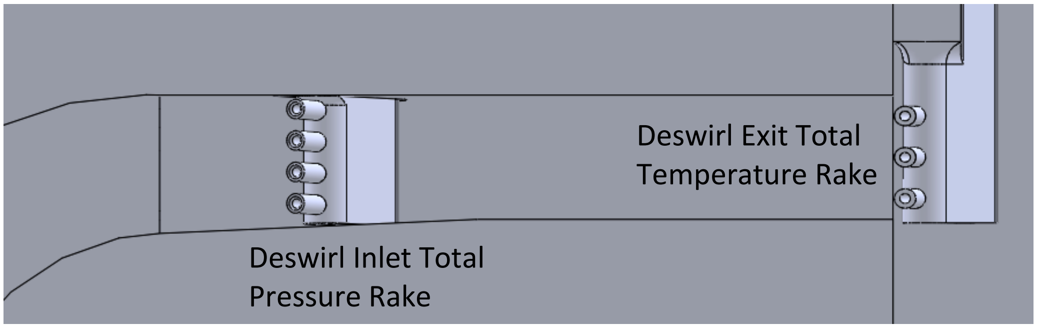

Figure 2.19: Deswirl Flow Path.

CHAPTER 3: MEASUREMENTS AND CALCULATIONS

The instrumentation utilized to quantify the performance of all aspects of the compressor is described below. This section will explain in detail the different measurement devices used along with the calculations of the parameters that define the compressor performance. After describing the measurement devices, the rig instrumentation will be discussed.

3.1 Data Acquisition

All instrumentation is monitored by a dedicated computer running a primary LabVIEW VI. This VI communicates with the instrumentation described below to provide real-time analysis of the compressor performance, allowing operators to analyze performance measurements as the compressor is running and set the compressor operating condition.

3.1.1 Voltage Measurements

Within the main VI, two National Instruments PCI-6035E data acquisition cards provide voltage measurements of the compressor instrumentation. These data acquisition cards are installed directly into the two PCI slots located on the performance monitoring computer's motherboard. Both are capable of providing up to 16 analog input single-ended measurements, meaning that they are all referenced to a common ground. These channels have 16 bit resolution and can be configured to read ±10 V, ±5 V, ±1 V, or ±0.1 V full scale range. These configurations allow for more accurate measurements of some of the low voltage signals that are received by the instruments. All channels are capable of reading up to 200,000 samples per second simultaneously and are estimated to have ±108.5 µV of uncertainty due to drift with time, temperature drift, and estimated noise.

Each card also has 2 analog output channels that are capable of providing up to 10V output with 8.127 mV of uncertainty at a rate of 10 kHz. This higher uncertainty is in part a result of a decreased resolution of 12 bits for these channels. Two National Instruments CB-68LP unshielded connector blocks interface the voltage measurements using screw terminals. SH68-68 shielded cables connect the CB-68LP connector blocks to the data acquisition cards.

3.1.2 Temperature Measurements

An Agilent 34980A Multifunction Switch/Measure Mainframe is used to measure temperatures relating to the compressor performance. This versatile measurement unit uses an internal DMM that is capable of measuring thermocouples, RTDs, voltage, resistance, frequency, and current. It is interfaced with the LabVIEW performance code via an Ethernet connection, providing remote access to the module over which commands can be sent and measurements gathered. The measurement method is a continuously integrating multislope analog-to-digital converter. This method supplies the unknown voltage being read to an integrator over a specified period of time, then applies a known reference voltage to the same integrator until the sum of the outputs is zero. Knowing the integration time and the reference voltage, the output voltage is calculated with high accuracy. The 34980a has 6.5 digits of resolution and 0.004% uncertainty due to this technique. Different modules are interfaced with the mainframe with different capabilities and specification.

The lab's current setup utilizes two 34921A multiplexer modules to collect compressor temperatures. Similar to the CB-68LP, two 34921T connector blocks with screw terminals provide easy access for the positive and negative leads of measurement wires to interface with the module. Though this measurement unit is capable of high accuracy measurements through the integration technique, the process makes it a slow analog-to-digital conversion method and, as such, this module is only capable of sampling 100 channels per second. Each module is equipped with 40 channels, capable of input voltages up to 300V, and features an internal thermocouple cold junction reference. Despite the convenience of the internal cold junction, this reference is not sufficiently accurate and adds significant uncertainty to the measurement. The internal cold junction is measured with a MAXIM DS1631U integrated circuit thermometer with an accuracy of ±0.5 degrees Celsius, which is not acceptable for the goals of this research. A different reference measurement is used to circumvent this issue. Because of the versatility of the measurement unit, it is capable of also measuring resistance thermometers (RTDs), which are capable of providing significantly higher-accuracy temperature measurements. An Omega SA1-TH-44031-40-T RTD with an uncertainty of ±0.1 degrees Celsius is placed in the center of the 34921T measurement block on one of the channels. This more accurate measurement is then used as a cold junction reference for the thermocouples channels.

In addition to the large uncertainty resulting from the internal cold junction, another large portion of the uncertainty results from the thermal gradient within the connector block, listed as ±0.5 degrees Celsius. The typical configuration involves mounting the connector block directly onto the 34921A module, which is then inserted in the 34980A mainframe. The components within the measurement unit produce a significant amount of heat and with the module situated directly behind the mainframe, there is significant conduction through the connector block. Four Y1135A 1.5 meter extension cables, two for each module, were purchased to avoid this issue and reduce the temperature gradient through the block. These extension cables interface between the module and the measurement block and allow it to be situated away from the mainframe.

All thermocouple measurements from the compressor are routed via Omega TT-T-20-SLE T-type thermocouple wire with special limits of error. The special limits of error option reduces the estimated error through the wires to 0.9°F (0.5°C).

3.1.3 Pressure Measurements

Because so many pressures are measured throughout the compressor, many different pressure measurement devices are utilized. The majority of these measurements are collected by the Scanivalve DSA 4000 enclosure which houses the versatile and accurate Scanivalve DSA 3016 Rack Mounted Digital Sensor Array. The 19-inch rack-mounted enclosure is capable of housing 8 DSA 3016 modules and communicates with LabVIEW via Ethernet. A processor housed in the enclosure controls communication with all the modules and also converts each measurement to engineering units. Each module houses 16 channels and are each individually capable of measuring 2 different pressure ranges each. The ranges currently utilized are summarized in Table 3.1 along with each module's associated uncertainty and overpressure range. The modules have 16 bit resolution in the analog-to-digital converter and are capable of sampling up to 625 samples per channel per second. Each channel has a personal lookup table stored in flash memory to quickly convert the voltage reading to engineering units and is thermally compensated to account for thermal drift. Additionally, the modules are capable of a quick zero at any point during operation. This command exposes both sides of the sensor to the reference pressure, determines the measurement voltage based on this reading, and compensates for this offset.

To interface compressor pressures to the DSA modules, Scanivalve NYLN-063 nylon tubing is used. The tubing lengths of approximately 25 feet ensure that no spurious pressure fluctuations effect the steady measurements. Because the DSA modules are equipped with 1/16th inch tubulations and the compressor is equipped with

0.042 inch tubulations, Scanivalve TC063-04R stainless steel reducing connectors are used to increase the size of the tubing from the compressor to the sensors.

Though different modules are capable of having different reference pressures, the current configuration has all pressures referenced to a common one. A settling plenum located outside the test cell dampens any changes in pressure and provides a relatively isolated reference that is not influenced by sudden changes in the environment. Because the absolute, not the gage, pressure is required for all calculations, this reference pressure must be determined. This is done using a Mensor CPT 6100 Digital Pressure Transducer. This high accuracy transducer has a range of 14.3 to 14.7 psia and provides the reference pressure for all the pressure transducers utilized. The CPT 6100 has a full scale accuracy of 0.01% resulting in a reference pressure uncertainty of 0.005 psi. Like the DSA enclosure, this module has temperature compensation that accounts for any thermal drift. This device communicates via an RS232 serial interface to provide calibration data, but it otherwise uses a 0 to 5V voltage output to communicate the sensed pressure. This voltage is measured by one of the PCI 6035E data acquisition cards, which averages the DC voltage signal over 100 samples to reduce measurement noise. A second Mensor is also used with a span of 0 to 0.36 psig with the same full scale accuracy to measure the total pressure upstream of the venturi. This second signal is also measured using the first PCI 6035E card.

The isolated settling plenum used to stabilize the ambient pressure is also the reference for two Scanivalve DSA 3217 Digital Sensor Arrays which share many of the same features and capabilities as the DSA 4000 enclosure discussed above. The 16 channel pressure transducers are calibrated to 30 psig with 0.05% full scale accuracy, resulting in an uncertainty of 0.015 psi. Each have a dedicated static IP address used to communicate via Ethernet with the LabVIEW program. These sensors also have 16 bit resolution and are capable of zeroing any DC offset and compensating for thermal drift. They sample at 500 samples per channel per second, slightly lower than that of the enclosure.

Aside from the two Mensor units, one other type of pressure transducer is used to determine high accuracy measurements of the system. Three Rosemount 3051C pressure transducers are used to determine inlet pressures upstream and within the venturi. Two of these units are calibrated to measure a range of 5 inH2O differential and the remainder calibrated to measure a range 50 inH2O differential, all with a performance uncertainty 0.14% of the full span. This low-power device is powered by a 12V power source and provides an output from 1V to 5V within the calibrated range. The outputs of these three sensors are all interfaced with the LabVIEW program through the first PCI 6035E card. As with the Mensor voltage measurement, the Rosemount voltage output is averaged over 100 samples to mitigate any line noise.

The final pressure transducer utilized is not as much for performance quantification as it is for performance monitoring. An Omega PX319 High Performance Pressure Transducer is placed in the beginning of the exhaust piping to monitor for surge. This lower accuracy pressure transducer has an uncertainty of 0.25% of its 200 psig range, resulting in uncertainty of 0.5 psi, but it has a response time of less than 1 millisecond. The output is a 0 to 5V signal that is continuously monitored via the second PCI 6035E data acquisition card and plotted in real time. A sudden drop in exhaust pressure measured by this signal will notify the operator that the compressor has fallen into surge.

The Omega HX94 Relative Humidity and Temperature Transmitter is flush mounted with the flow and used to measure the water content of the air. This sensor is housed in a stainless steel enclosure to withstand the elements and equipped with both a relative humidity and temperature reading to determine the humidity ratio of the flow. A thin film polymer capacitor is used to measure the relative humidity of the air between 3% and 95% RH within 1% uncertainty. The polymer absorbs water from the air based on the relative humidity which causes a change in the capacitance of the polymer. This change is measured and converted to a 0 to 1V signal output corresponding to the humidity. Because of this lower voltage output, this signal is interfaced with the first PCI 6035E card, with the appropriate channel configured to read 1V full scale range to increase the measurement resolution. This unit is powered by a 24V voltage source.

3.1.4 Speed Measurements

A Laureate Frequency, Rate & Period Meter measures the compressor’s rotational speed. The panel mount tachometer is capable of receiving two input signals and individually monitoring both on its 6-digit LED display. It is capable of reading both PNP and NPN outputs and has nine different configurable voltage ranges that are used to distinguish spurious signals. The device is calibrated to within an uncertainty of 2 pulses per minute which results in a compressor rotation speed uncertainty of only 0.06 RPM. The first channel is capable of sampling frequencies up to 1 MHz and the second up to 250 kHz. An adjustable gate time, the time over which the device counts pulses, is configurable up to 200 seconds and has been chosen to be 0.5 seconds, as this length has been determined to provide accurate frequency readings through signal testing. This device measures the output of the motor encoder and internally multiples it by an appropriate scale factor to determine the compressor rotational speed. That scale factor was determined to be 1.78486, calculated below) knowing the motor encoder count of 1024 pulses per revolution and the gearbox ratio:

$$X\,\frac{comp\ rev}{min}\left(\frac{1\,motor\ rev}{30.46153846\,comp\ rev}\right)\left(\frac{min}{60\,sec}\right)\left(1024\,\frac{pulses}{motor\ rev}\right)=Y\,\frac{pulses}{sec}$$

$$\rightarrow\quad X\,\frac{comp\ rev}{min}=1.78486\,\left(Y\,\frac{pulses}{sec}\right). \tag{3.1}$$

The Laurel Rate Meter has a 0 to 10V output over a configurable range, but this method is not the most accurate for performance readings. A USB connection between the meter and the computer acts as a COM port, providing serial communication that returns the RPM reading directly from the display.

A laser tachometer is also used to measure the compressor speed. A TTI LT-880 Laser Tachometer is installed upstream of the inlet rakes where the nosecone is painted black with the exception of one sliver that corresponds to the impeller’s first blade. As the nosecone rotates, a 2 mm diameter low-power laser beam of wavelength 650 nm is projected onto the surface. The dull black surface does not reflect the laser to the receiving optics but when the laser passes the unpainted metal, the light is reflected back. The fiber optic cable that emits the laser is flush mounted with the inlet and located 1.05 in away from the surface, within the 12 to 125 mm specified. Tests showed that the laser power output is highly sensitive and negatively associated with fiber bends. As such, the tachometer is placed far from but at the same plane as the compressor to maximize the bend radius of the signal carrier.

3.1.5 Capacitance Probes

As previously explained, the tip clearance of the impeller has a large effect on the performance of the compressor. Because this compressor has been designed with the ability to change the tip clearance, it is important to determine this distance to link changes within the flow field to this gap. To determine the tip clearance throughout the operating range, a capacitive displacement sensor system was utilized to non-intrusively measure tip gap throughout the operating range.

Located at about 50% of the shroud flow passage, at the knee of the impeller, three holes located at 30 degrees, 150 degrees, and 270 degrees circumferentially are used to seat the measurement probes. Further downstream, three additional holes are drilled at the same circumferential locations to determine the tip gap in the exducer. Inserted into each of these holes is a probe assembly consisting of a probe boss, cap, and a capacitance probe. This assembly is shown in Figure 3.1. The capacitance probe is an electrode housed in a quarter inch threaded casing. The probe boss is used to secure the assembly and is tapped for the insertion of the probe. This boss becomes seated within and bolted to the shroud to ensure that the probe remains in place throughout testing. The cap is flush mounted to ensure that there are no sudden changes in the flow path geometry that would affect aerodynamics and that the measurements remain non-intrusive.

A triaxial cable of concentric positive, negative, and guard lines extends from the probe. This guarded cable configuration reduces the noise that permeates the signal and is interfaced via a Lemo connector to the next component, the oscillator. The oscillator is responsible for driving the internal circuit that measures the change in capacitance with each blade passing and is shown in Figure 3.2. One module is needed for each probe and the total group of six are located approximately two feet from the compressor. These provide the probe with a 7V peak-to-peak signal to both the inner and guard lines of the triaxial cable. By providing this signal to both the inner and guard lines, changes in the cable capacitance which would affect the measurement signal are reduced. The signal provided is sinusoidal with a 2 MHz frequency that is maintained by an internal control circuit to remain constant. Precise control of the frequency ensures that the measurement is not contaminated by specious changes in the capacitance that should only be a result of the blade passing. As blades pass beneath probe, the capacitance of the electrode changes. This change in capacitance results in a modulation of the carrier signal that corresponds to the probe’s distance from the blades.

Coaxial cables carry the modulated signal from the oscillators located in test room, through the wall, and to the control station. These connect to the system demodulators, shown in Figure 3.3. The demodulator modules, which are each capable of reading one oscillator signal, convert the modulated signal frequency that has been altered by the blade capacitance to a DC voltage through a converter circuit. Two different signals are produced within the demodulators. This first is the output of the direct conversion from frequency to DC voltage. This results in a high-frequency signal resembling a half wave rectified sine wave with narrow peaks that correspond to each blade's passing and valleys corresponding to the passing of the flow passage. The voltages at the peak can then be translated to an appropriate tip clearance. A second signal from the modulator is produced by sending the blade passing signal previously explained through a rectifier and low pass filter to produce a DC voltage signal that is representative of the average tip clearance of all the blades. Unlike the blade passing signal, within the average signal individual blade pass events cannot be distinguished and provide no information on the impeller blade-to-blade variations.

The blade passing signal is then input to Super Micro Computer SC811 Chassis operating as the central processing modules. Advantech PCIE-1774 analog-to-digital converters are inserted in each of the modules and interface via a PCI Express serial bus. These converting cards are capable of each reading 4 analog voltages with 12 bit resolution at up to 30 MS/s on each channel. In the current configuration, two chassis are used to read the 6 probes. Powering the entire system is a dedicated power supply which stabilizes any possible inconsistent power from the grid.

The tip clearance monitoring program is able to determine the compressor speed based on the frequency of the voltage peaks in the blade passing signal and the number of blades within this compressor. It is also able to keep track of the individual blades, ensuring that the first blade measured on the first rotation remains the corresponding first blade on the final rotation. Though this capability ensures that the blades are consistent for a single test, there is no guarantee that the blades remain consistent from test to test. To fix this issue, the program is able to read the once per rev signal from the laser tachometer and use this to repeatably assign the correct blade number to each blade passing event. When the program recognizes the passing of the reflective section of the nosecone, it acknowledges that this is associated with a certain blade number and is able to assign all the blades accordingly.

The voltage sampled and input into the central processing modules must then be converted to a corresponding tip clearance. The change in capacitance of the probe is governed by two primary factors, the blade tip geometry and the distance to the blade tip. As the blade geometry remains constant for the compressor, any changes in capacitance will be a result of the blade tip growth. A calibration is performed to determine the relationship between the tip clearance and the demodulator output voltage. Because of the difficulty of removing and shipping the impeller out to the calibration facility, the manufacturers of the measurement system made two calibration disks intended to represent the geometry of the impeller at the probe locations. Small variations in the electronics can significantly vary the output of the signal so the plastic, electrode probe, and oscillator must be calibrated as one unit. This is important because it limits the exchanging of plastic caps between probes and does not allow swapping of probes between oscillators. The probe is backed away from the rotating blades to known increments, and the corresponding voltage is recorded. The data are then compiled to provide a distance as a function of voltage curve, one for the blade passing signal and one for the filtered average signal. During testing, the processing modules compute the tip clearances at each probe in real time.

3.2 Calculations

Measurements from the instrumentation previously discussed are used to quantify compressor performance. Nondimensionalization of the flow parameters ensures repeatable compressor performance on a daily basis and allow for experimental testing with a wide range of inlet conditions. The next section describes this process of nondimensionalization and characterizing performance.

3.2.1 Air Composition

First, the thermodynamic state of the incoming air must be determined, and this is done using the pitot probe and relative humidity sensor located just after the first bellmouth. This probe measures the total and static pressure along with the total temperature. These are collected with the 0.36 psi range Mensor, 5 inH2O range Rosemount, and the Agilent 34921A module, respectively. Knowing the total and static pressures of the flow, the static temperature can be determined if the ratio of specific heats is known. To determine this, a program called REFPROP [24], which is utilized heavily throughout the performance calculations, is used. REFPROP is a FORTRAN-based program developed by the National Institute of Standards and Technology that is used to determine thermodynamic and transport properties of fluids. This database uses high-order equations to determine the thermodynamic state and corresponding property values of fluid mixtures and has an accompanying Matlab function. Given two intensive properties and the mixture composition, this function calls the database and determines the requested property. It is called using a Matlab script in the LabVIEW interface.

REFPROP is first used when calculating the ratio of specific heats at the pitot probe. Because the program needs to know the makeup of the incoming mixture, the relative humidity is essential in determining an accurate composition that includes not only dry air but also its water component. The saturation pressure of water can be determined using the total temperature measured, eventually leading to the humidity ratio and air composition. If the temperature is above freezing, the REFPROP function determines the saturation pressure of water using the given temperature with a vapor quality of zero. If the temperature is below freezing, the database is not able to calculate its saturation pressure and so a sixth order polynomial fit recommended by Flatau et al. [25] is used. The coefficients are shown in Table 3.2 and use the temperature in degrees Celsius as a variable. With the relative humidity and the saturation pressure determined, the vapor pressure can be found by:

$$P_{vapor} = P_{saturation}\left(\frac{RH}{100}\right). \tag{3.2}$$

The humidity ratio, the ratio of water mass to dry air mass, can be found knowing the vapor pressure. This ratio is a function of the vapor pressure and air pressure and can be determined by the equation:

$$\frac{m_{vapor}}{m_{dry\ air}} = \frac{0.6219\left(P_{vapor}\right)}{P_{air} - P_{vapor}}. \tag{3.3}$$

From J. Wright [26], the composition of dry air is assumed to be made up of Nitrogen, Oxygen, Argon, and Carbon Dioxide with the molar fractions shown in Table 3.3. The composition of the inlet air, including water vapor, is determined from the humidity ratio and dry air mixture. The mixture composition, the total temperature, and static pressure are input into the REFPROP function to determine the inlet specific heat ratio.

The static temperature can be determined using the isentropic compressible gas equation:

$$\frac{T}{T_o} = \left(\frac{P}{P_o}\right)^{\frac{\gamma-1}{\gamma}}. \tag{3.4}$$

As mentioned, the specific heat ratio used was determined using the total temperature, which is not a true thermodynamic property and thus not indicative of the actual state. Because of this, the composition calculated is not the actual mixture but only an estimate. Additionally the static temperature calculated is also an estimate, albeit an accurate one because of the low sensitivity of the specific heat ratio to small changes in state.

To determine the actual properties at the inlet, the described process is iterated using the calculated static temperature and measured static pressure, though typically only a single iteration is performed. This method provides the true thermodynamic state of the incoming air and is used to calculate the density, viscosity, and specific heat ratio.

3.2.2 Mass Flow Rate

The venturi flow meter is used to measure the mass flow rate through the compressor. This flowmeter uses the pressure difference resulting from an area contraction to determine the mass flow rate. The pressure difference related to a velocity increase is determined using Bernoulli's equation, which neglects gravitation effects and assumes incompressible, inviscid flow, given as:

$$P_1 - P_2 = \frac{\rho}{2}(v_2^2 - v_1^2). \tag{3.5}$$

Equation (3.5) is valid for steady flow. Because each compressor point is measured at a steady operating condition, the mass flow rate will be steady, and this assumption is valid. Additionally, the venturi has been designed and sized to ensure that the Mach number is below 0.3, ensuring that the flow can be considered incompressible. By relating the pressure difference to velocity and knowing the dimensions of the venturi, the equation for the ideal steady mass flow is:

$$\dot{m}_{ideal} = \frac{\pi d_t^2}{4\sqrt{1-\beta^4}}\sqrt{2\Delta P \rho_{inlet}}\,, \tag{3.6}$$

with d_t as the throat diameter, β as the ratio of the throat diameter to inlet diameter, ΔP the pressure difference between the inlet and throat, and ρ_1 the inlet density.

Though this ideal mass flow rate is easy to formulate and simple to calculate, it does not capture all of the phenomena occurring in the venturi and is only valid for the ideal case. Viscous effects and the compressibility of the fluid must also be taken into account. A coefficient called the expansibility factor is introduced to account for the compressibility of the fluid. This equation relates the pressure difference, the specific heat ratio, and venturi geometry to determine the change in mass flow rate due to the air’s compressibility. Below is the analytically derived equation for the expansibility factor:

$$\varepsilon = \sqrt{\left(\frac{\gamma\left(\frac{P_2}{P_1}\right)^{\frac{2}{\gamma}}}{\gamma-1}\right)\left(\frac{1-\beta^4}{1-\beta^4\left(\frac{P_2}{P_1}\right)^{\frac{2}{\gamma}}}\right)\left(\frac{1-\left(\frac{P_2}{P_1}\right)^{1-\frac{1}{\gamma}}}{1-\frac{P_2}{P_1}}\right)}\,. \tag{3.7}$$

Another correction term is included, called the discharge coefficient, to account for the viscous effects, and it is a function of Reynolds number. The venturi was sent to Colorado Engineering Experiment Station, Inc to provide a NIST-traceable calibration of the discharge coefficient. While at the facility, the flowmeter was tested over a Reynolds number range covering that which will be experienced over the compressor mass flow range. This coefficient was determined over the flow range by dividing the mass flow rate supplied by the calculated idealized mass flow with compressibility effects included. A fourth order polynomial fit was derived relating the discharge coefficient to the Reynolds number.

Because the mass flow rate is dependent both on Reynold number and discharge coefficient, an iterative approach must be used to determine the actual mass flow rate. The mass flow rate can be related to the Reynolds number using:

$$\dot{m} = \frac{Re_t \mu \pi d_t}{4}. \tag{3.8}$$

This results in an equation with Reynolds number as the only variable. This equation with a, b, c, d, and e being the zeroth, first, second, third, and fourth order coefficients of the discharge coefficient polynomial, respectively, is:

$$\frac{\mu\sqrt{1-\beta^4}}{\varepsilon d_t \sqrt{2\Delta P \rho_1}} Re_t = \ a + b(Re_t) + c\ (Re_t^2) + d(Re_t^3) + e(Re_t^4). \tag{3.9}$$

This equation is difficult to solve analytically, but can be solved using the iterative Newton-Raphson Method, a technique that determines the roots of a zero-valued function. Using an initial guess, the slope of the function at this location is determined and used to find an estimate of the unknown variable at the function’s root. At this estimate, the slope is again determined and used to find a more accurate root estimate, and this is iterated until a stopping condition is reach. In the case of the venturi, the zero-valued function is:

$$f(Re_t) = \left(\frac{\mu\sqrt{1-\beta^4}}{\varepsilon d_t\sqrt{2\Delta P\rho_1}}\right)Re_t - a - b(Re_t) - c\ (Re_t^2) - d(Re_t^3) \\ -e(Re_t^4), \tag{3.10}$$

The Reynolds number of the ideal flowrate is determined and used as the first estimate. The iterative process to determine next estimate is shown, where n is the iteration number:

$$Re_{t,n+1} = \ Re_{t,n} - \frac{f\left(Re_{t,n}\right)}{f'\left(Re_{t,n}\right)}. \tag{3.11}$$

The process is complete when the difference in Reynolds number between iterations is less than 0.01, which usually takes around three iterations. With the Reynolds number determined, the mass flow rate can then be found.

3.2.3 Compressor Performance Parameters

The compressor performance must be nondimensionalized because conditions of the incoming ambient air change throughout the day and the seasons. To nondimensionally characterize the compressor’s performance, common Buckingham Pi groups relating the mass flow rate and wheel speed to pressure ratio have been determined and are extensively used. An updated method has been proposed by Berdanier et al. [27] to account for the effects of humidity. This method uses the speed of sound and density. Because both of these thermodynamic properties are dependent on the fluid composition, humidity is inherently taken into account. The two parameters used to define the compressor performance are the corrected speed and corrected mass flow rate:

$$N_c = \frac{N_{mech}}{a_{o,act}/a_{o,ref}} \text{ and} \tag{3.12}$$

$$\dot{m}_c = \dot{m}\left(\frac{\rho_{o,ref}a_{o,ref}}{\rho_{o,act}a_{o,act}}\right). \tag{3.13}$$

The reference conditions used are those defined in the referenced paper. The reference speed of sound is calculated assuming dry air with the gas constant of 53.351 ft lb_f/lb_m - °R, specific heat ratio of 1.4, and total temperature of 518.67 °R. The reference density is calculated using the ideal gas law, the same above properties, and a reference total pressure of 14.696 psi.

Both the total pressure and total temperature inlet rakes are area-averaged to determine the stagnation speed of sound needed for both the corrected flow and speed calculations. Area averaging is used because, as shown by Lou et al. [28], this averaging technique reduces the amount of uncertainty when compared to mass-averaging. The stream tube areas are determine using the impeller hub radius, shroud radius, and midpoints between each rake element. Using these as the representative total pressure and temperature at the inlet and knowing the fluid composition of the incoming air, REFPROP is called and calculates the total enthalpy, total speed of sound, total density, entropy, and specific heat ratio. These stagnation properties are used to determine the corrected conditions needed to characterize the compressor performance. Additionally, the static temperature and pressure are found, and the true thermodynamic properties determined using the specific heat ratio along with the static pressure measured at this inlet plane.

The exit conditions of the air must also be determined to quantify the overall compressor performance. Total temperature and total pressure rakes in the deswirl section are used to determine the exit thermodynamic state. As with the inlet, the exit rakes are area averaged over the probe elements to provide the representative stagnation exit conditions. The total pressure ratio can be determined knowing the inlet and exit total pressure:

$$Rc = \frac{P_{o,exit}}{P_{o,inlet}}. \tag{3.14}$$

Additionally, the total enthalpy at the exit is determined using REFPROP knowing total pressure, total temperature, and fluid composition, and it is used to determine the specific work performed by the compressor. The isentropic work is then calculated and used to determine the overall efficiency of the machine, using the specific entropy found at the compressor inlet and knowing the exit total pressure:

$$\eta = \frac{h_{os,exit} - h_{o,inlet}}{h_{o,exit} - h_{o,inlet}}. \tag{3.15}$$

Table 3.1: DSA 3016 Module Specifications.

Module	Pressure Range (psid)	Uncertainty (psi)	Overpressure (psi)
1	± 5	± 0.0025	10
2	± 15	± 0.0075	30
3	± 15	± 0.0075	30
4	± 30	± 0.015	60
5	± 30	± 0.015	60
6	± 30	± 0.015	60
7	± 30/± 50	± 0.015/± 0.025	60/100

Table 3.2: Coefficients of Polynomial Fit of Frozen Water Saturation Pressure in kPa as a Function of Temperature in Celsius, from Flatau et al. [25].

Polynomial Order	Coefficient
0	0.610952665
1	5.01948366E-2
2	1.86288989E-3
3	4.03488906E-5
4	5.39797852E-7
5	4.20713632E-9
6	1.47271071E-11

Table 3.3: Mole Fractions of Dry Air, from Wright et al. [26].

Molecule	Mole Fraction
N_2	0.780872685
O_2	0.209410256
Ar	0.009332056
CO_2	0.000385002

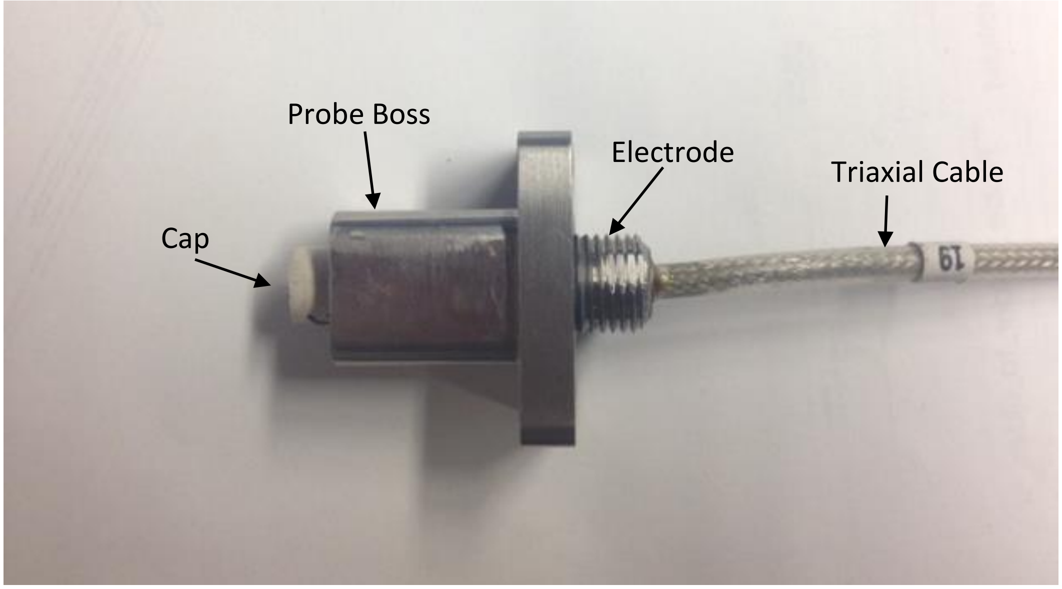

Figure 3.1: Probe Assembly.

Figure 3.2: Capacitance Probe Oscillators.

Figure 3.3: Capacitance Probe Cart.

CHAPTER 4: ESTABLISHING REPEATABLE FACILITY OPERATION

Various aspects of the facility were investigated to ensure that the compressor performance has repeatability. To reduce temperature fluctuations at the inlet, a settling chamber was constructed that mitigates the effect of ambient environmental variations. Also, a standard procedure for capacitance probe calibration and installation was established to ensure accurate measurements of the impeller tip clearance. Preparation for future measurement techniques was also considered. A ray-tracing analysis was performed on a shroud window to investigate the feasibility of LDV measurements within the impeller region.

4.1 Ray Tracing for LDV Measurements

4.1.1 LDV Measurements in the CSTAR Facility

As documented by Heckaman [22], the CSTAR facility has been designed to allow optical access for Laser Doppler Velocimetry (LDV). This measurement technique is performed by intersecting two laser beams, referred to as a beam pair. At the intersections of these beams, a fringe pattern is produced from the constructive and destructive interference of the lasers. As particles seeded into the flow enter this measurement volume, they reflect the light back to the photodetector. The frequency of the sense reflected light is a function of the distance between fringes and the speed of the particle. The difference between the fringe pattern frequency and the sensed frequency is a result of the Doppler shift caused by the particle moving through the volume. This Doppler shifted frequency is used to determine the speed of the particle in the direction of the fringe pattern. Three sets of beam pairs are needed to create fringe patterns in different directions to determine three components of the velocity vector.

Two windows were designed and structurally analyzed to allow optical access to the impeller, vaneless space, and the diffuser. Ray tracing was performed to ensure the viability of the endeavor prior to manufacturing the windows and hardware to provide optical access to the compressor flow path. Because of the compound curvature and small radii defining the geometry of the impeller window, it was necessary to determine the effect these factors had on the beam alignment.

4.1.2 Two Dimensional Probe Analysis

A program called TracePro was utilized to perform this analysis. TracePro utilizes the Monte Carlo method to determine each light ray's path through optical devices in a three dimensional environment. Though this program's CAD interface supports creation of lenses within the program, it is also capable of importing designs from other design programs such as Solidworks. As such, the windows designs were imported into the program. Solids and surfaces in TracePro can be specified with optical properties that are either defined by the user or from a large database of typical optical materials. Fused silica was used for this analysis. In addition to the imported impeller window, two

Dantec LDV probes, one with two perpendicular beam pairs and one with only one set of beam pairs, were designed in CAD to represent the basic features of the different probes. Surfaces were created on the probe faces that were separated by the appropriate distance, angled to intersect at the probe focal point, and dimensioned to the beam width. These probes were inserted into TracePro where these surfaces were chosen to emit a densely packed set of rays resulting in the same power output as that of the probe lasers.

Five locations were chosen along with flow path to check that the flow could be measured throughout the impeller passage. These locations were determined as approximate targets for the measurement volume and cover the range of window curvatures that the lasers encounter. These locations were specified with small flat plates as show in Figure 4.1. Each beam (or collection of rays) was configured to be a certain color to easily determine the intersection of the beams.

The first analysis considered only the two dimensional probe at two different orientations. The first had one beam pair aligned at a constant tangential location and the other beam pair aligned at a constant axial location. With this configuration, each beam pair was affected by only one direction of curvature and, although the appropriate lasers intersected at different measurement volumes, each pair intersected, nonetheless. The second orientation was clocked 45 degrees relative to the first orientation resulting in each beam of the pairs entering the window at a different axial and tangential location. This resulted in each beam set experiencing two different curvatures. Figure 4.2 shows the resulting beam intersections of the second orientation. The beams do not intersect with their respective pairs. Because of this issue, the first orientation was used to perform the analysis.

Figure 4.3 shows the results of the analysis. At the inlet of compressor, where the flow is primarily axial and curvature in the meridional direction is small, there is still some discrepancy in the measurement volumes. The beam pairs do not intersect at the same location but are separated by approximately 1.5 mm, resulting in a large uncertainty of the measurement volume. As the beam is directed further downstream, the decreased radius-of-curvature of the flow path causes even higher deviations in the beam intersection locations. The largest deviation is found at the third location, as expected because the curvature is highest, and is 3 mm. This discrepancy is reduced as the beam is directed toward the end of the impeller where the flow path is primarily radial. The difference of the intersections is reduced to 1 mm in this region.

4.1.3 Three Dimensional Probe Analysis

The second analysis introduced the second probe with only one beam pair needed to provide the third dimension of velocity. Like the first analysis, five points were chosen to provide approximate targets within the flow path covering the range of window curvatures. Some additional misalignments were introduced with the addition of the second probe that affected the beam alignment. In the first analysis, the two dimensional probe was centered over the window. Because it was centered, the beam pairs entered nearly normal to the glass, minimizing the distance that the laser traveled through the window. Additionally, the centering resulted in distortion of the laser beams being symmetric. This symmetry reduced issues with the beam alignment of each pair.

The additional probe had to be angled from the two dimensional probe to distinguish a third component of velocity. The angled measurements can be transformed and the third velocity component evaluated. The angle introduced between the probes in the analysis was 30 degrees, which significantly minimizes the uncertainty without requiring additional optical access. With the addition of the second probe, the first laser could no longer be normal to the window but had to come in at an angle, causing two additional difficulties. First, the beams had a longer distance to traverse through the window, causing them to refract over longer distances. Second, approaching at an angle caused the probes to lose their symmetry. Not only did the beams of each pair traverse a longer distance through the window, but they traversed uneven distances, introducing another issue that contributed to the beam misalignment.

The results of this analysis, shown in Figure 4.4, are similar to those found in the first. At the first location, the 2D probe shows an offset of 1.4 mm between the two measurement volumes. Because the other beam pair is on a separate probe, it has the mobility to ensure that its probes align with one of the measurement volumes of the 2D probe. Location 2 shows the highest difference in the measurement volume of 2 mm. This reduces to 1 mm in the exducer at the final analysis location. Present at each location is the slight misalignment caused by the antisymmetric beam refraction mentioned previously.

Because these issues persist in all configurations, it is necessary to acquire a probe attachment that will compensate for the misalignments. A beam translator attachment from Dantec can be mounted to the probes and is capable of the fine adjustment of the individual beams needed to intersect all the pairs.

4.2 Capacitance Probe Measurements

4.2.1 Initial Clearance Measurements

During preliminary testing when compressor repeatability was being established, the only clearance measurements gathered were the output low pass filtered signals that provide a DC voltage corresponding to the average tip clearance. This DC voltage was gathered on the performance computer's PCI 6035E data acquisition card, and the corresponding clearance was spline interpolated from the calibration data. Throughout testing, though they remained repeatable, the readings at each probe location varied greatly. At the exducer, the difference between the three probe measurements was more than 0.012 in, which is significant given that the desired clearance of the compressor is ultimately 0.005 in. The problem persisted at the knee, with a variation of 0.008 in between the three knee probes.

A borescope was used to verify the capacitance probes were installed flush to the flow path. After removing the inlet plenum and bellmouth, the camera was inserted into the impeller flow path at each of the probe locations. At every location, it was clearly visible that the plastic caps were either recessed or intruding into the flow. This explained the discrepancies between the different circumferential measurements at the same shroud location. The probes were made flush with the shroud surface using the view from the borescope. It was noticed that the probe depth was very sensitive to the torque on the bolts securing the boss to the shroud. First, to ensure that none of the plastic caps protruded into the flow, thick shims were placed between the shroud and each of the probe bosses. Then using the sensitivity of the depth with bolt torque, the bosses were fastened down until the cap appeared flush with the flow path.

In subsequent runs, the minimum clearance amongst all the blades was required. Because of this, the cap probe system's monitoring software was used to record the blade heights at each performance point. Within the monitoring program, data can be stored by hitting the manual record button. At each point approximately 10 seconds of blade passes are manually recorded, which corresponds to at least 1800 revolutions of data at 50% speed. With each blade clearance now captured, the minimum clearance can be determined at the tallest blade.

After visually inspecting the probes and making them flush, subsequent tests still showed some discrepancies in the clearance measurements. Though the exducer clearance range was significantly reduced to approximately 0.002 in at low mechanical speeds, the deviations in the knee were still approximately 0.006 in.

4.2.2 Shroud Uniformity

The shroud was removed to ensure that each cap was flush with the flow path. While off, the shroud was also measured to determine if circumferential variations were present at the cap probe locations. Circumferential variations in shroud geometry could cause different blade heights to be measured at different circumferential locations because of the flow path's varying distance to the impeller. To precisely determine the shape of the shroud, it was taken to Touchstone Measurement Services which used a CMM to determine the shape of the shroud at each probe location.

Measurements showed that the variations at both probe axial locations were not large enough to account for the measurement differences. A circular sweep of the shroud at the knee location determined the x and y locations of the surface corresponding to the radius and angle and the z location corresponding to the axial location. Using the original solid model, the profile of the designed shroud was determined to provide the ideal shroud radius as a function of the axial location. To compare the measured profile and the CAD profile, the axial location of the measurement was used to determine the nominal radius at this axial position. Then, using the x and y measurement data, the measured radius was calculated. The difference between the actual and nominal radius was found and this difference was determined as a function of circumferential location. As shown in Figure 4.5, measurements revealed a slight circumferential variation of less than 0.002 in and a variation of approximately 0.0007 in was found between the knee probe locations. At the probe locations, because there is no actual material and no shroud profile, the CMM lost track of the surface, as shown by the sharp peaks. The rest of the profile remains smooth, though.

Because the exducer probe radial location is very steep and the flow path is primarily radial, variations in the axial direction proved a more useful indicator of the circumferential uniformity. As with the other location, the x, y, and z data were measured and the corresponding radius calculated. Using this radius, the design shroud axial location was determined, and the difference between it and the actual measured location was found. The circumferential variation is shown in Figure 4.6 where only slight variations of approximately 0.0015 in over the entire shroud and 0.001 in variation between the probe locations exists.

4.2.3 Capacitance Probe Installation

A probe installation procedure was developed with the shroud off the compressor to ensure that the probes could be repeatably inserted to the proper depth, flush with the shroud. The flushness of the probes was controlled by three variables: cap orientation, the torque of the probe boss fastener, and shim thickness. The shroud was held upright during the development of the seating procedure to remove any changes caused by the angle of the shroud and keep it in the same orientation as it would be when mounted on the compressor. The proper probe orientation was determined and marked so that it was consistently clocked. Because the depth of the probes would also be governed by the shim thickness, all of the probe boss mounting bolts were fastened to the same torque of 20 in-lb. This value was chosen because it could be easily applied and measured using a torque wrench while ensuring that the boss was properly secured to the shroud and immovable. This torque also made each probe protrude into the flow, ensuring that shims could be used to back the probe out to the appropriate depth. To determine the required shim thickness between the boss and shroud, each probe assembly (boss, cap, and probe) was secured with the proper torque and the depth into the flow path was measured using a feeler gage. The appropriate shim was then cut and inserted and this process was iterated until each probe was flush with the shroud. Table 4.1 shows the thickness of the shims determined for each location. Repeatability tests showed that the caps remained flush with the shroud when the above procedure was followed.

This procedure resulted in close agreement in the exducer probes which varied less than 0.001 in. While the two knee probes at 30 degrees and 270 degrees were in good agreement, the third knee probe at 150 degrees showed a deviation from these of approximately 0.004 in. This probe has provided erroneous readings in the past, thus, could be damaged. This installation also revealed that the visual installation using the borescope was not accurate. After looking at the new installation, a clear difference between what looked flush, which had previously been used to set shim thickness, and what was actually flush, which could be examined, was observed

Tests in this configuration revealed a difference in blade geometry. Figure 4.7 shows the blade clearances that were measured at the 150° knee location. The carrier signal modulation is a function of two things: the distance to the blade and the tip geometry. Because the impeller could not be sent to the calibration facility, two disks (for the exducer and knee locations) with representative blades were manufactured and tested. At the knee location near the midpoint of the impeller flow path, the splitter blade thickness does not match the main blade thickness. The splitter blade is 0.38 in thick while the full blade is 0.42 in thick. When the calibration disk was made to correspond to this location, only the splitter blade geometry was used, and thus, the calibration was incomplete.

4.2.4 In-Situ Calibration Mechanism

An in-situ calibration procedure was developed to eliminate the need to send the probe back to the calibration facility and ensure that accurate measurements of both the full blades and splitter blades could be determined. This also ensured that the probes were subject to the true impeller geometry, providing the most accurate calibration. A calibration stand shown in Figure 4.8 was designed to accurately position the probes and vary the tip clearance over the range that will be experienced during compressor operation. This stand consists of two Velmex A5990TS manual rotary tables that allow for precise angular positioning with an accuracy of 100 arc-second. Additionally, a Velmex UniSlide manual linear slider with micrometer head is used for the calibration. This slider provides linear movement in 0.001 in increments to plunge the probe. Attached to the slider is the probe mounting brace which holds the probe assembly, including the boss.

To perform the calibration, the stand is firmly mounted to the front face of the compressor's collector using the quarter inch bolt holes already tapped. The probe mounting brace is then aligned with the probe locations and the angles are noted. The center of the second rotary table is aligned with the axis of the probe hole by rotating the table attached to the collector. The second table is then rotated to align the probe mounting brace coincident with the probe location. With the angles of both rotary tables noted, the slider assembly is then rotated out of the way of the shroud. The shroud is then removed from the compressor with the stand still attached to the collector. Because the calibration stand can stay attached while the shroud is removed, the uncertainty introduced by removing and replacing the stand is eliminated and the rotary table angles are ensured to remain accurate for the calibration procedure.

The rotary tables are then returned to their proper positions, locating the slider on the probe axis. The plastic cap is then made flush with the tallest blade by plunging the linear slider. To make the cap flush with the tallest blade, the probe mounting brace is moved toward the compressor till the cap hits the blade. The caps are slightly malleable so this initial plunge is typically too deep and does not create a proper zero on the blade surface. The zero is set by slowly rotating the blades past the probe and backing out the mounting brace. Tones caused by contact between the blades and the cap stop just after the probe is at the proper distance. The zero of the highest blade can then be used as a reference for subsequent measurement distances. The probe is then backed away to the first clearance location of 5 thousandths of an inch away from the highest blade. With the turntables and slider locked in place, the compressor is then spun by hand, and the voltage of this blade is used to determine the calibration curve. The probe is then backed in increments of 0.004 in. This is done up to 0.05 in, which will cover the entire range of clearances the probes will see in this configuration. Because of the different blade geometry at the knee, the results must be processed to distinguish alternating blades and calculate two calibration curves for the splitter and full blades.

4.3 Temperature Fluctuations

4.3.1 Initial Testing

During initial compressor testing, inlet temperature fluctuations were significant which made setting mechanical speed difficult because of temperature's effect on speed of sound, found in Equation (3.12). Once the compressor reached 95% corrected speed, it became increasingly difficult to hold corrected speed. Despite remaining at a constant impeller mechanical speed, the corrected speed fluctuated by 0.18% of the design speed between data points, or about 40 RPM, which is significantly out of the set tolerance of 7 RPM. These swings in corrected speed occurred in 5 seconds intervals, and fluctuations of this magnitude persisted at these high speeds.

Though low compressor speeds showed little variations in the inlet temperature, significant fluctuations of approximately 1.8°F were measured at 95% corrected speed and beyond, contributing to the variations in corrected speed. Because these fluctuations were only present at higher speeds and accordingly higher mass flow, it was thought that these issue could be caused by an ingestion problem. Initially, this ingestion was thought to be a result of the temperature differential between the room and the ambient. With all test cell doors open to cool the room, warmer air could have flowed from the test cell through the front set of doors closest to the bellmouth.

The test cell doors closest to the inlet were closed completely and the rear doors were angled to direct flow away from the bellmouth. Though the temperature fluctuations seemed occasionally reasonable in this configuration, they were still not consistently reduced. As such, it was determined that while ingestion from the room could have cause some of the fluctuations, there were additional issues still present

By eliminating interactions with room air, the conditions of the ambient environment were then examined. Winds in the area surrounding the bellmouth inlet and just outside the test cell raised concerns of temperature fluctuations caused by high speed ambient air. A look at an overhead view of the environment just outside the test cell, shown in Figure 4.9, gives insight on why these gusts consistently interacted with the inlet. Though the wind was low to nonexistent in the open field, a large tank sits approximately 30 feet away from the facility causing an area reduction for any ambient air moving through around the building. This contraction accelerates the flow, causing strong winds from the South to consistently blow through this area. With the high velocities experienced and the bellmouth pulling this air to feed the compressor, the ambient air conditions by the facility can change more quickly.

In addition, heat exchangers near the inlet were suspected of causing additional oscillations in the temperature for two reasons. First, with the strong winds impinging on the heat exchangers, shedding off the structure could cause the oscillations at the inlet of the compressor. The second disturbance is a result of the structure's function. The heat exchangers use a fan to accelerate ambient air over fins attached to the oil piping. As this air passes through the fins, the oil is cooled and its heat is transferred to the accelerated air. This heated air is then ejected from the heat exchanger on the south side of the structure to the surroundings. Interactions between this heated air and the cooler ambient could also cause the temperature fluctuations in the compressor inlet flow.

4.3.2 First Settling Chamber

A large settling chamber was constructed around the inlet bellmouth to diminish the effect of the erratic gusts at the inlet. This settling chamber allowed the flow entering the compressor time to settle and equalize. The chamber itself was made from a 3 ft diameter PVC pipe duct which was shipped in a 20 ft length. For the initial testing of the settling chamber, this duct was cut in half to test the concept and reduce the size of the structure. Though the shorter section did not move the inlet far from the heat exchanger structure, this initial configuration was tested to narrow down the cause of the fluctuations. At the inlet of the settling chamber, a large pegboard sheet was fastened that would dampen out sudden gusts and isolate the incoming flow from the ambient. At the other end, where the bellmouth interfaced with the ducting, a set of wooden doors were installed. Gaps between the door and chamber were filled with filter material to again isolate the flow. By installing these hinged doors, the filter material covering the bellmouth was easily accessible in case it needed to be changed. The chamber geometry resulted in a residence time of approximately 1.5 seconds at the design mass flow rate.

With the addition of this settling chamber, the magnitude of the temperature fluctuations was reduced, but the spurious oscillations in temperature were still present and consistently caused problems in setting the corrected speed. Figure 4.10 shows an example of the temperature fluctuations regularly measured. To capture this data, the Agilent Measurement Unit continuously scanned the inlet temperature thermocouples Though the acquisition process of using an integrating voltmeter provides high accuracy, it is relatively slow so the temperatures were gathered and written approximately every 1.5 seconds. Though this is a long acquisition time, it was short enough to capture trends in the inlet temperature profiles

4.3.3 Second Settling Chamber

In an attempt to further reduce variations and increase residence time, another truss support structure was built and the additional 10 feet ducting was attached to the section already installed. This also extended the settling chamber far beyond the heat exchanger structure, abating their effect on the inlet. This new extension is shown in Figure 4.11. Though the doors on the first configuration allowed for easy replacement of the filter material, they were not completely flush or perfectly aligned with the side of the ducting. These gaps were filled with filter material but could still allow air in that exited the heat exchangers. A new design to interface the bellmouth and ducting was created to eliminate this issue and is shown in Figure 4.12. A tarp and bungie cords were utilized to create a tight seal around the interface between the inlet ducting and chamber. This new setup allowed for not only a much better seal on this end of the settling chamber, but it also facilitated the assembly and disassembly required to change the bellmouth filter.

With this additional length of settling chamber, not only was the inlet moved far away from the heat exchanger structure, but the residence time of the chamber also was doubled to approximately three seconds, allowing the air even more time to settle. To verify the efficacy of the setup, the configuration was tested on many days. Figures 4.13 through 4.18 show the inlet temperatures gathered on the testing dates for all the elements of the inlet rake at the 330 degrees circumferential location with the compressor running at 100% corrected speed. Figure 4.18 and 4.19, which shows the ambient air temperature with time, can be used to compare the rake temperatures with ambient conditions and shows that the settling chamber successfully isolates the incoming air from changes in the field temperature. Despite large changes in the ambient temperature, the response at the compressor inlet is significantly damped and though the trends are similar, the magnitude of the rake fluctuations is significantly less than that of the outside air. The results of the tests are summarized in Table 4.2 which shows the testing date, data collection time, and the standard deviation of the elements on this inlet rake. The results show significantly reduced temperature fluctuations and indicate that the settling chamber performs well, albeit better on certain days than others. A clear trend is measured and shows fluctuations that are dependent on the time of day. Morning tests consistently show higher deviations that those of the later tests. This is because the morning sun impinges on the east-facing settling chamber and causes rapid temperature changes in the region of the supply air. As the sun is setting in the afternoon and evening, the field is somewhat protected by the shadow of the building, and as a result, this temperature is significantly more stable.

This configuration reduced the temperature fluctuations but there was still some difficulty in consistently maintaining speed. Despite not changing the set speed on the pedestal, some fluctuations in the mechanical speed were present. Any fluctuations of the motor speed were multiplied by 30 because of the intermediate gearbox, so even small fluctuations in the motor caused much larger ones on the impeller. At a constant motor speed set on the pedestal, variations up to 6 RPM were experienced by the impeller. Because of this, the corrected speed tolerance limit of 7 RPM was revisited. Speed tolerances within the lab are typically held to 0.1% of the compressor design speed, which would be in 22.5 RPM for the CSTAR compressor, but it was determined that this was higher than needed. Tests showed that with the reduced temperature fluctuations, the compressor motor speed could consistently be held to within 12 RPM or 0.053% of the design speed.

Table 4.1: Capacitance Probe Boss Shim Thicknesses.

Probe Location	Shim Thickness (thou)
1	16
2	16
3	14
4	12
5	14
6	8

Table 4.2: Standard Deviations of 210° Inlet Rake Temperature Fluctuations at Spanwise Locations.

Date	Time	Weather	Winds (mph)	9.2%	27%	44.9%	62.8%	80.6%
4/23	7:15AM	Clear	5	0.58	0.57	0.57	0.55	0.46
4/24	5:25PM	Overcast	7	0.23	0.24	0.24	0.25	0.22
4/26	10:57AM	Clouds	8	0.51	0.50	0.51	0.50	0.43
4/27	5:34PM	Clouds	20	0.31	0.31	0.31	0.32	0.27
4/28	8:20AM	Clear	4	0.33	0.35	0.33	0.34	0.30
5/01	10:40PM	Clouds	2	0.30	0.30	0.30	0.30	0.25

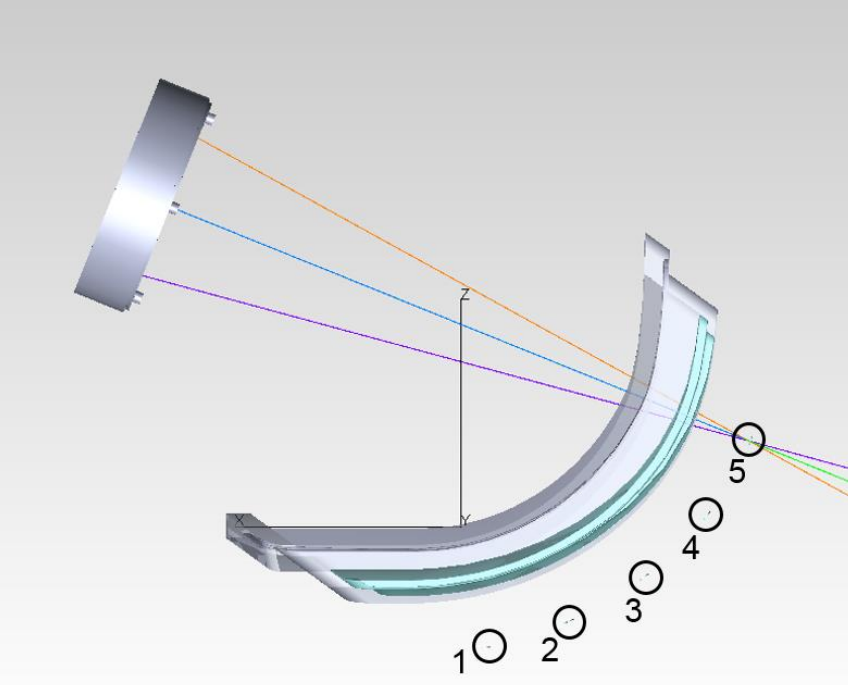

Figure 4.1: Locations of Measurement Targets for Ray Tracing Analysis.

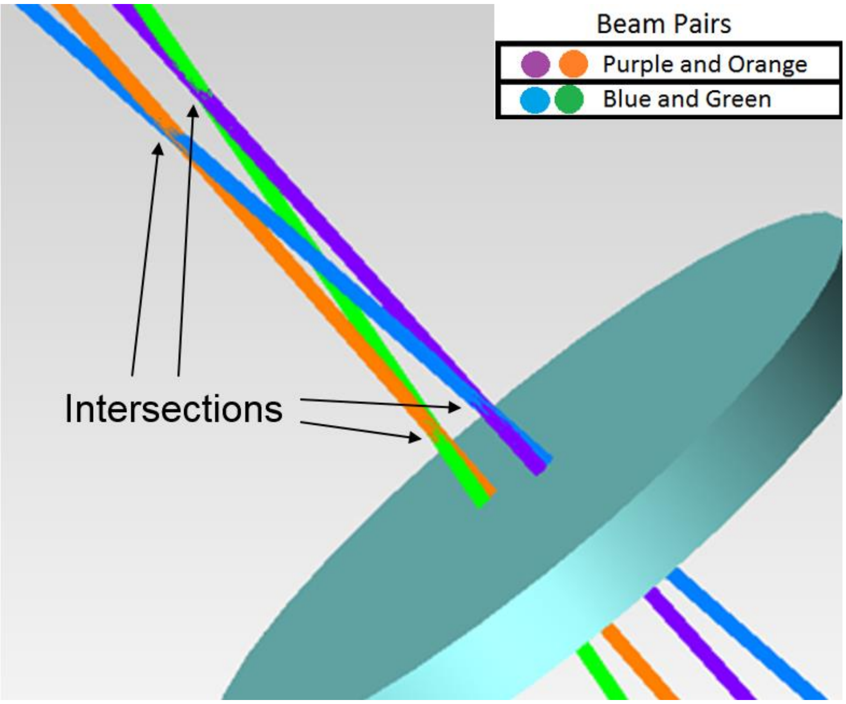

Figure 4.2: Result of 45° Probe Orientation.

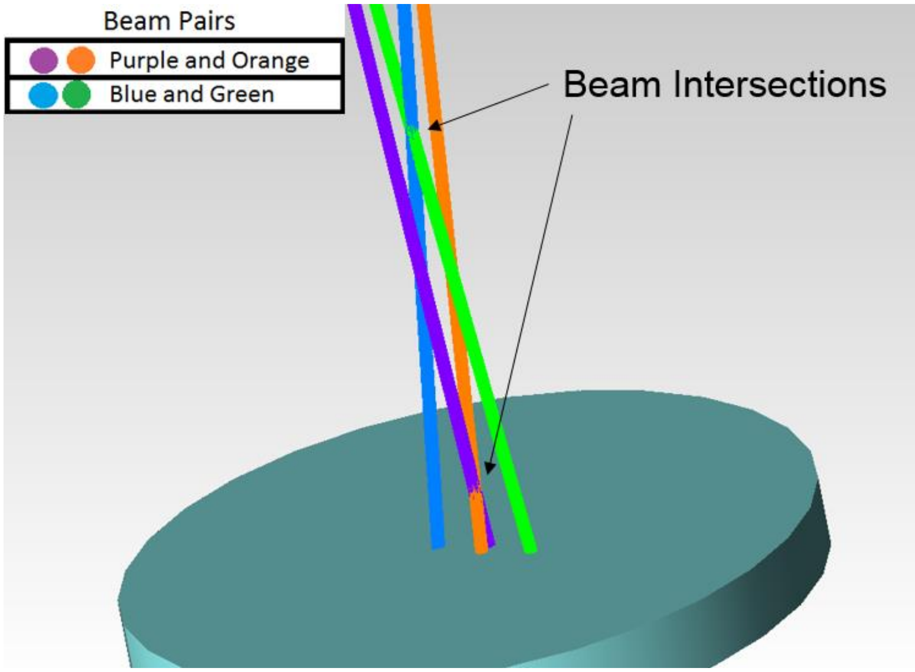

Figure 4.3: 2D Results Showing Misalignment of the Beam Pairs Through the Knee Window at the First Target Location.

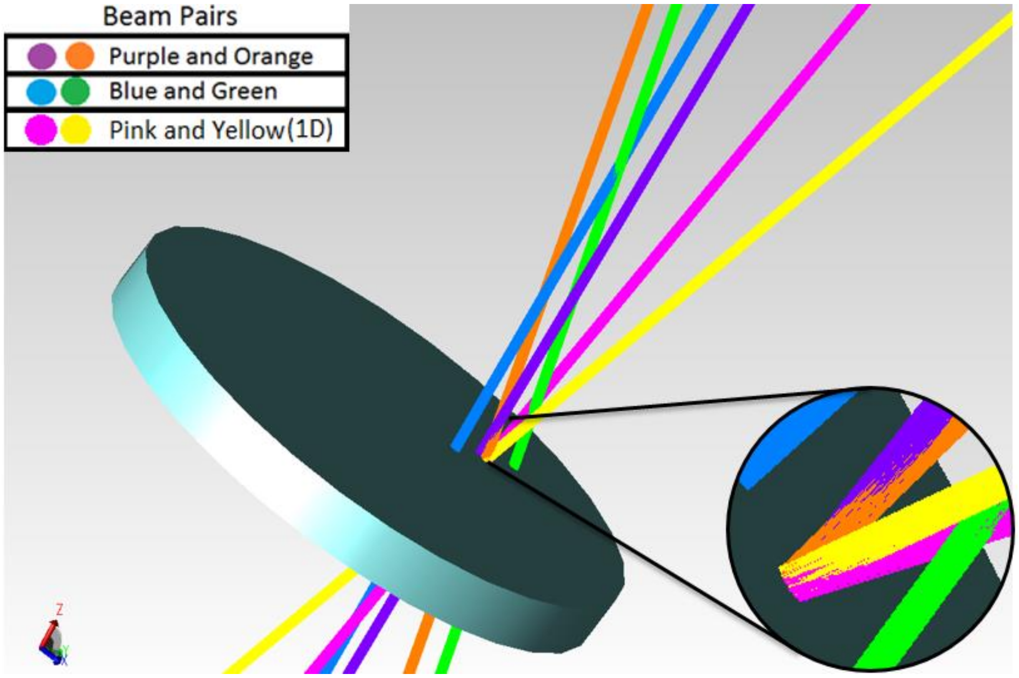

Figure 4.4: 3D Results Showing Misalignment of the Beam Pairs Through the Knee Window at the First Target Location.

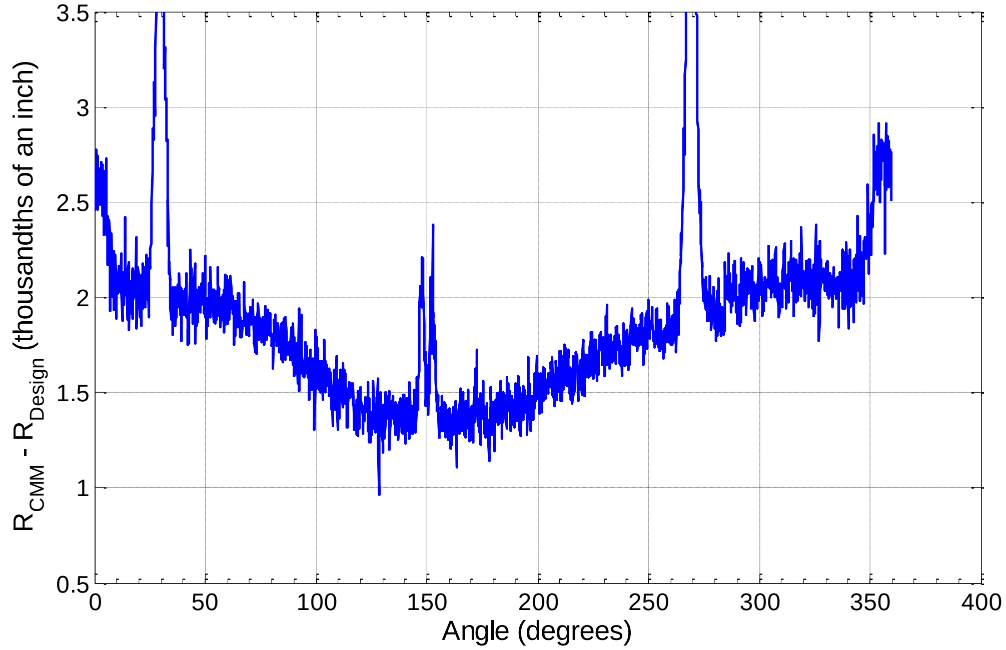

Figure 4.5: Difference between Design Radius and CMM Radius at Knee Cap Probe Location.

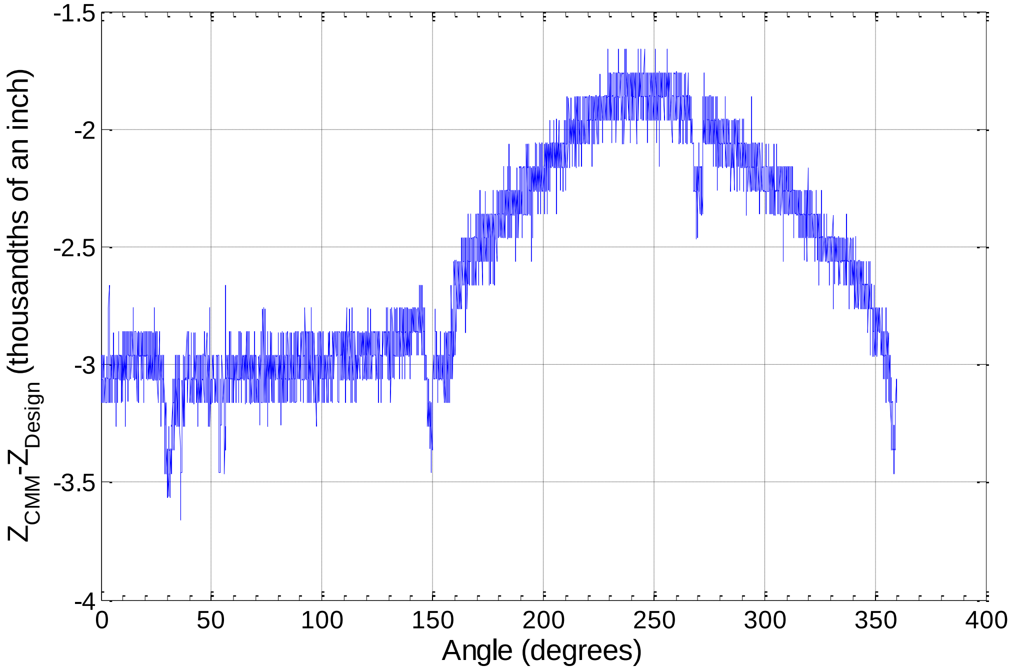

Figure 4.6: Difference in Design and CMM Axial Distance at the Exducer Cap Probe Location.

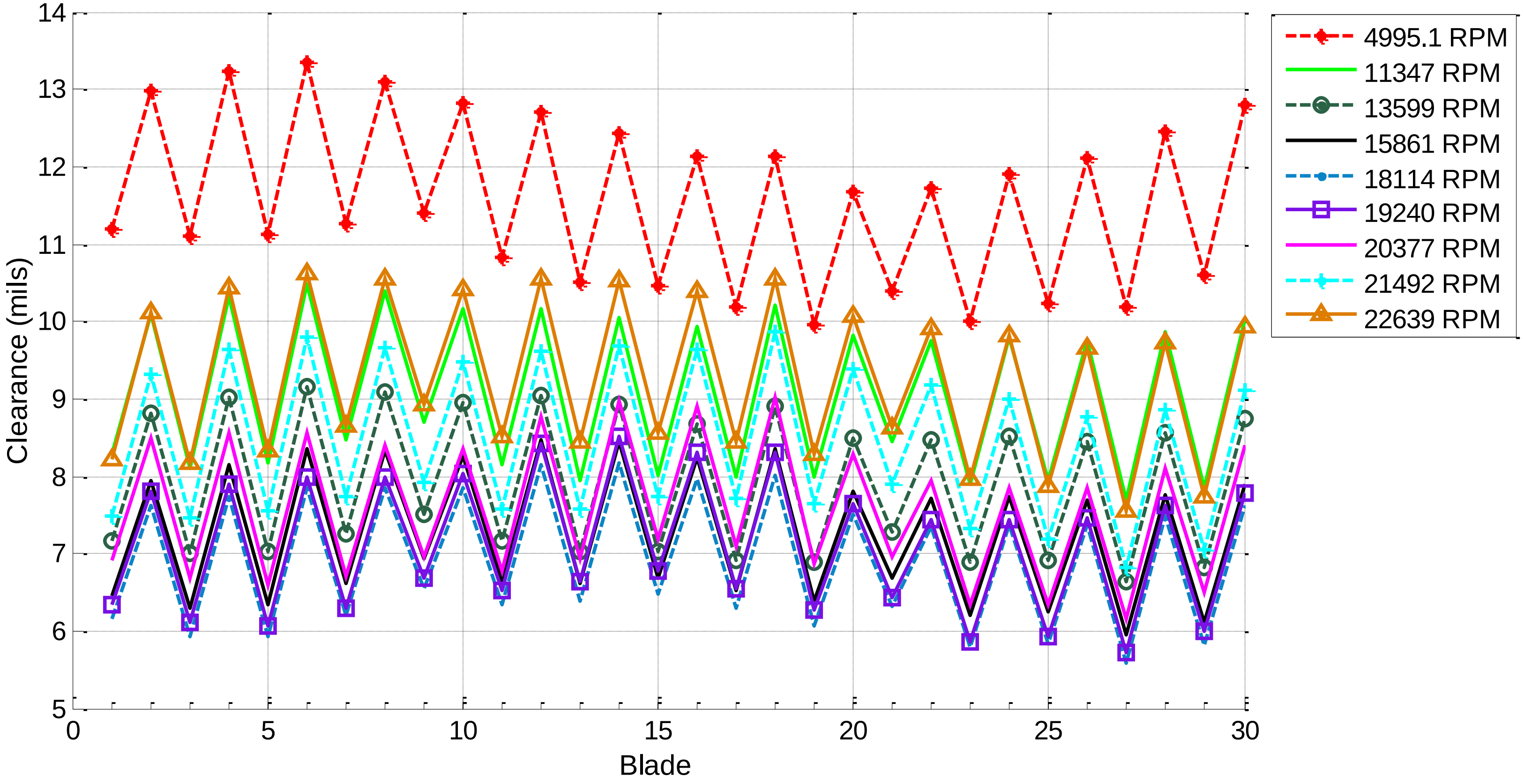

Figure 4.7: Sawtooth Pattern Observed at the 150° Knee Cap Probe Location.

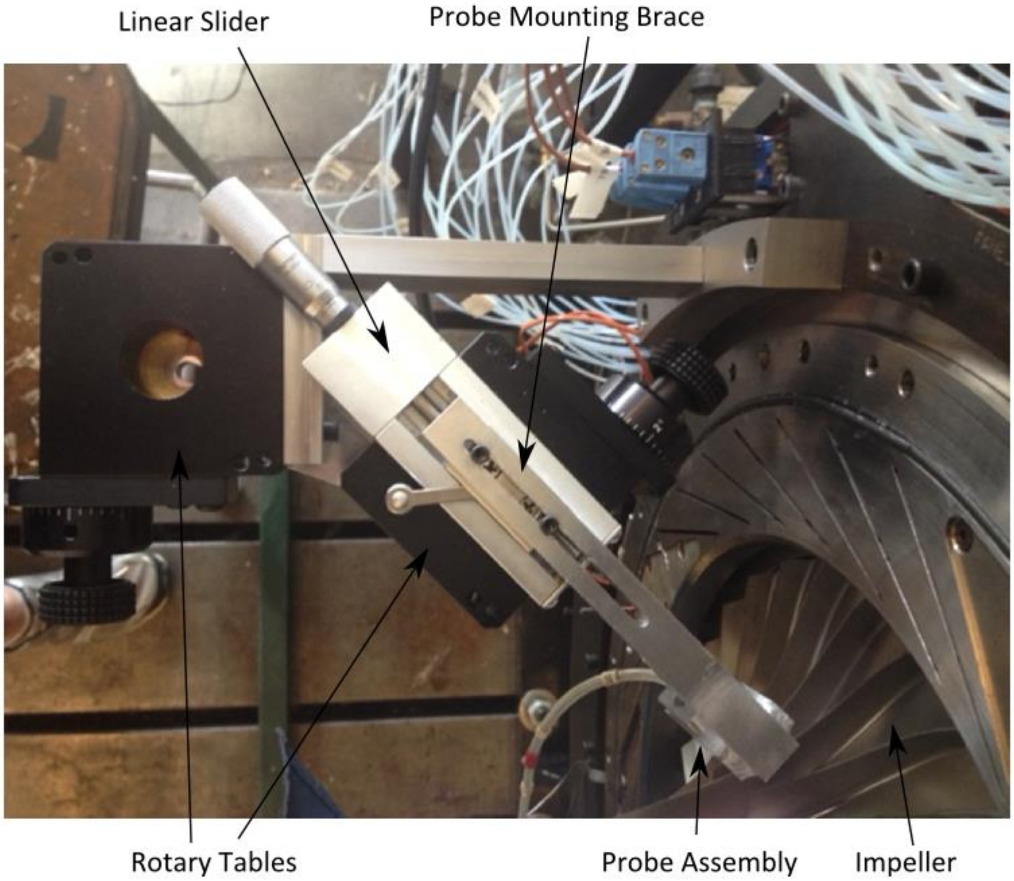

Figure 4.8: In-Situ Calibration Stand.

Figure 4.9: Ambient Test Cell Environment.

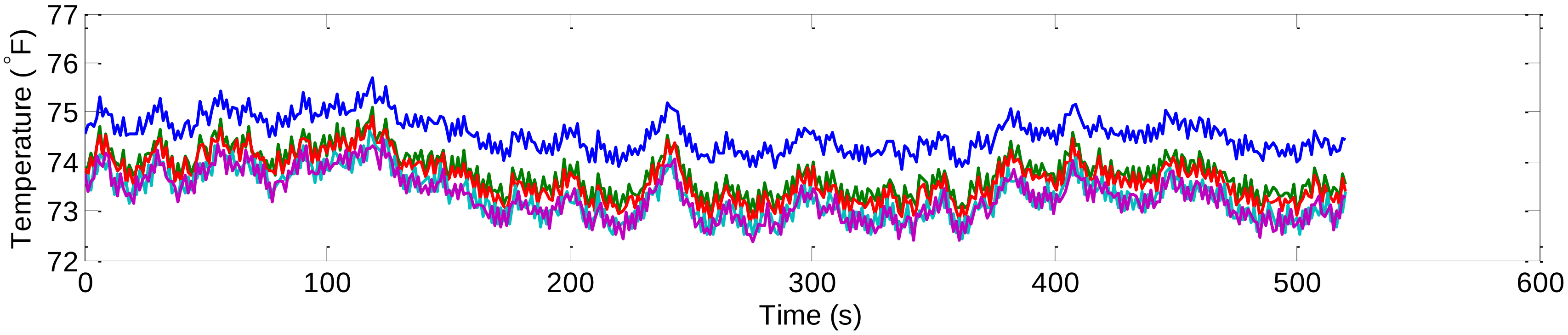

Figure 4.10: 210° Inlet Rake Temperature Fluctuations with First Settling Chamber Configuration.

Figure 4.11: Second Configuration of Settling Chamber with 20 Foot Length.

Figure 4.12: Seal between Inlet Ducting and Settling Chamber.

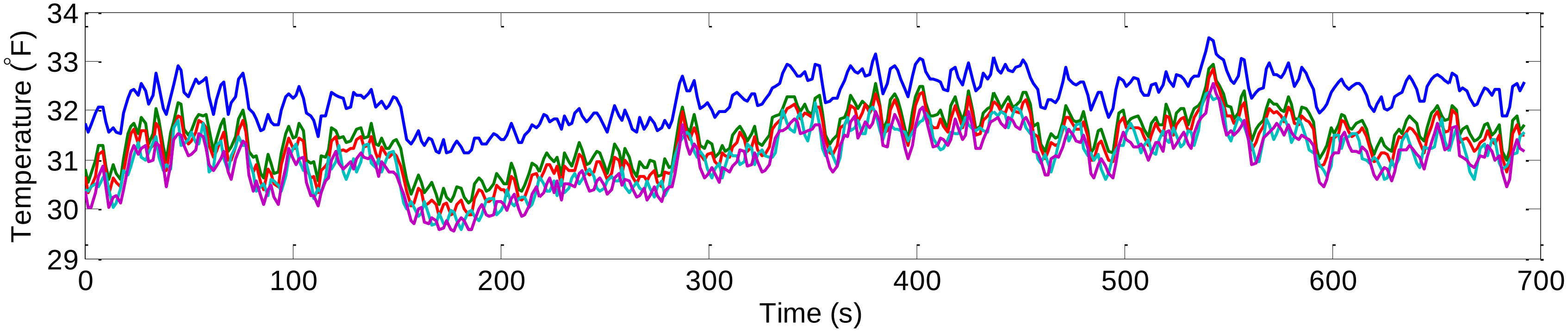

Figure 4.13: 210° Inlet Rake Temperature Fluctuations, 2nd Configuration, 4/23/15, 7:15AM.

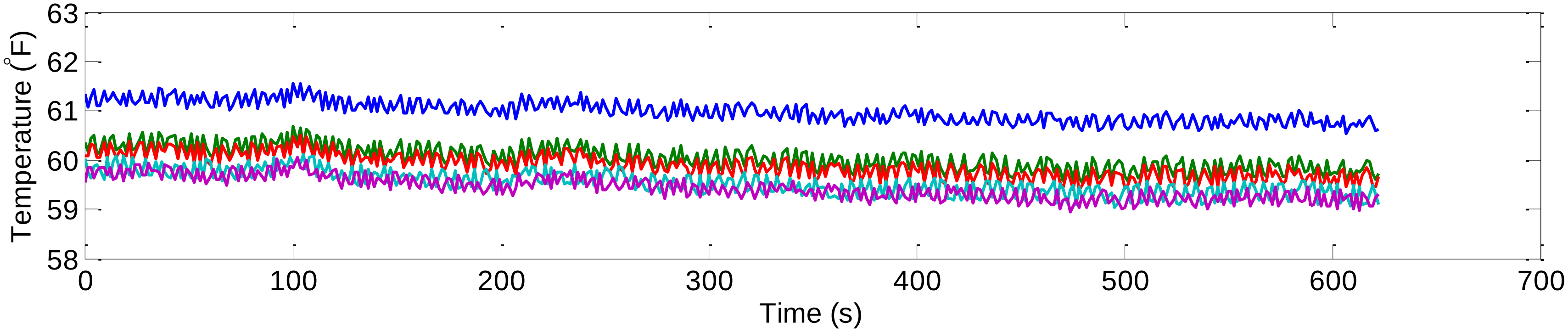

Figure 4.14: 210° Inlet Rake Temperature Fluctuations, 2nd Configuration, 4/24/15, 5:25PM.

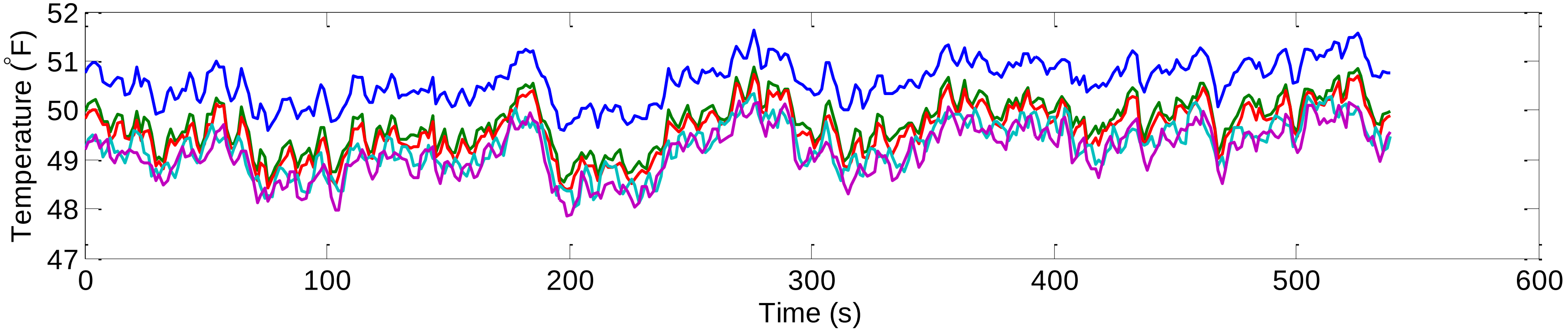

Figure 4.15: 210° Inlet Rake Temperature Fluctuations, 2nd Configuration, 4/26/15, 10:57AM.

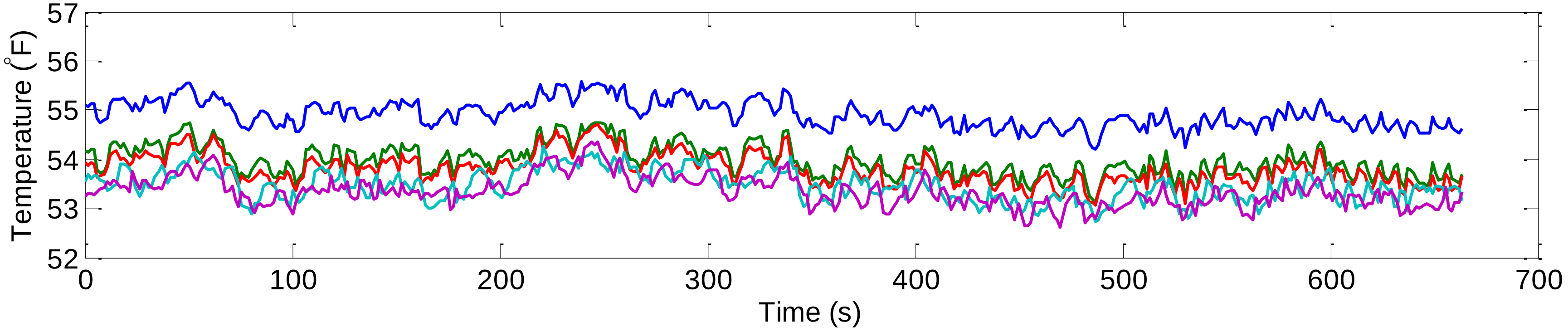

Figure 4.16: 210° Inlet Rake Temperature Fluctuations, 2nd Configuration, 4/27/15, 5:34PM.

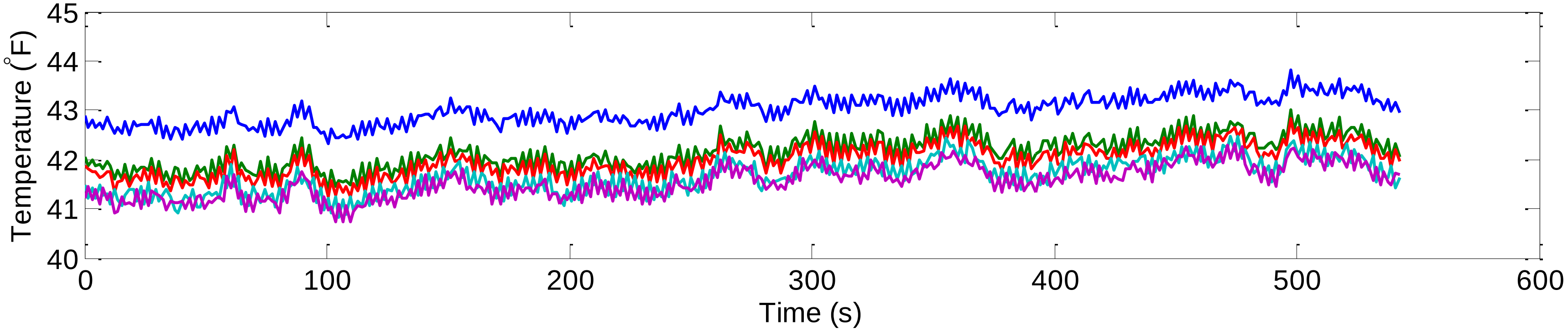

Figure 4.17: 210° Inlet Rake Temperature Fluctuations, 2nd Configuration, 4/28/15, 8:20AM.

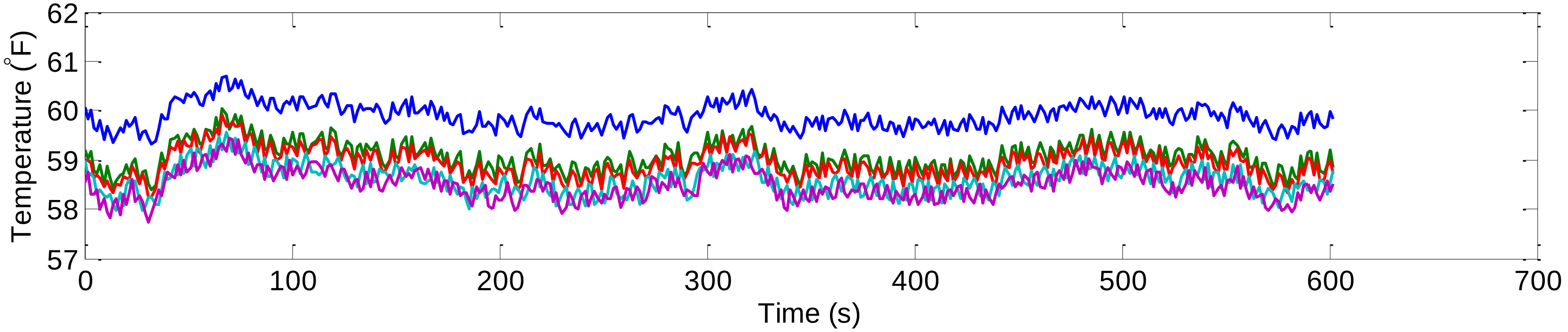

Figure 4.18: 210° Inlet Rake Temperature Fluctuations, 2nd Configuration, 5/1/15, 10:40PM.

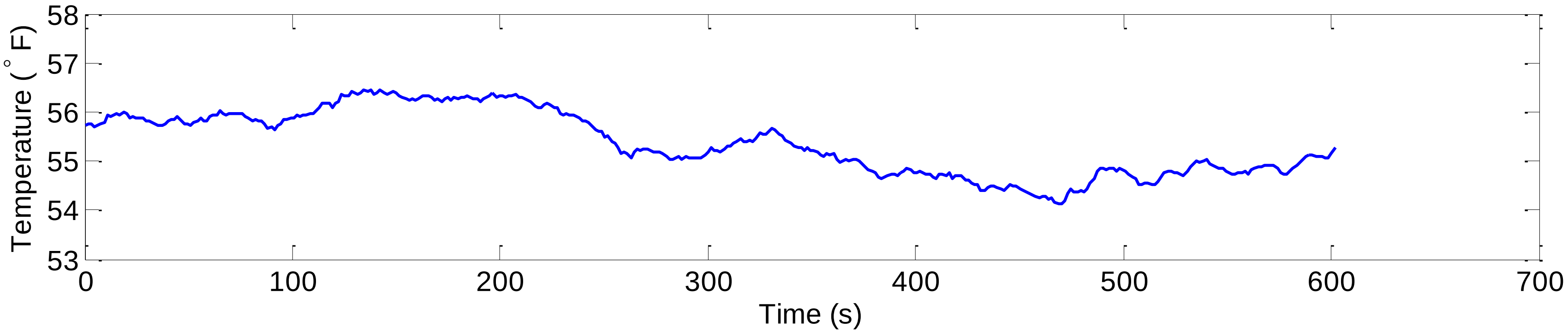

Figure 4.19: Ambient Temperature Fluctuations, 5/1/15, 10:40PM.

CHAPTER 5: COMPRESSOR PERFORMANCE

The results in the following section show measurements that quantify the compressor performance along the operating line along with the compressor performance map. Figure 5.1 shows a section view of the compressor with station numbering used throughout the results.

The steady state performance of the CSTAR compressor was determined and the compressor map of the current CSTAR configuration is shown in Figure 5.2. Speed lines at 70%, 80%, 85%, 90%, 95%, and 100% corrected speed are shown. Each speed line begins with the compressor significantly within choke. Points are then gathered by throttling the compressor until an upper limit is reached. The final points on each speed line are not the locations of stall but are at the upper limit line designated by the sponsor. Because of the possible tip rub that can occur at stall, it was desirable to remain away from that performance region and an upper limit was designated based on the predicted compressor performance. The mass flow rate and total pressure ratio are normalized because of the proprietary nature of the design.

Figure 5.3 shows the compressor efficiency as a function of the normalized mass flow. As the compressor speed increases, a reduction in the maximum efficiency occurs. A difference in peak efficiency of approximately 1.5 points is present between 70% and 100% corrected speed. This reduction could be a result of the heat loss through the shroud. More work is done on the fluid at higher rotational speeds, increasing temperatures. This increase creates a larger differential between the compressor air and ambient air temperatures, resulting in more heat transfer and a reduced isentropic efficiency.

5.1 Compressor Inlet Measurements

The temperature distributions within the plenum near the operating line at each corrected speed are shown in Figure 5.4. These temperatures are normalized by the area-averaged plenum temperature. An uncertainty bar representative of the temperature measurements is also shown in the figure. Throughout the operating range, a consistent profile occurs where the total temperature is constant at the inner radii. Despite insulation surrounding the entire inlet flow path, the temperature slightly increases at the larges radii due to the temperature gradient between the heated room and the incoming air. Figure 5.5 shows the pressure distribution within the plenum normalized by the ambient air pressure. Uncertainty is within the symbol size. A uniform distribution is shown throughout all of the operating points, indicating well-conditioned flow for the inlet of the compressor. As expected, the pressure loss through the inlet piping increases as the corrected speed increase indicated by the progressively lower plenum pressure. The flow rate and Reynolds number increase as the rotational speed increases, causing greater a pressure loss.

The compressor inlet plane conditions are used to normalize downstream measurements. The inlet plane measurements are normalized by their area average.

The total temperature distributions at the inlet plane show similar trends at 150 and 330 degrees indicated in Figures 5.6 and 5.7, respectively. The bar again shows the uncertainty of the measurement. Because of additional exposure to the hot ambient room temperature, higher total temperature occurs at the flow path walls. Both distributions show a steady increase from 0% span to 100% span of approximately 1.5°F despite insulation not only on the plenum but also surrounding the bellmouth.

Figure 5.8 shows the uniform distribution of total pressures at the inlet plane at 30 degrees, where the uncertainty is within the symbol size. Across all operating points, a similar distribution is found that indicates properly conditioned flow entering the compressor at this location. Figure 5.9 shows a different distribution at the 210 degree location total pressure rake. A consistently non-uniform entry profile is present throughout all operating points where the pressure steadily decreases with increasing distance from the hub for the first four elements. At the final element closest to the bellmouth, the pressure then increases significantly. This sudden increase in pressure at the bellmouth is not associated with a leakage.

5.2 Impeller Conditions

Figure 5.10 shows the circumferential distribution of static pressure just upstream of the impeller normalized by the area average total pressure. Mass flow increases with operating speed, and thus the velocity at the impeller inlet increase as indicated by the decrease in static pressure. Figure 5.11 shows the circumferential distribution 0.25 in downstream of the impeller leading edge. The acceleration of the fluid within the impeller further increases the velocity of the air, resulting in a greater static pressure drop at this axial location. Little diffusion has occurred at this location and thus, the static pressure remains low. At both of these locations and throughout the impeller, the uncertainty of the pressures are within the symbol size.

Additionally, static pressures are gathered along the impeller passage, shown in Figure 5.12. These data show the varying trends in pressure progression at different speeds. For low speeds between 70% and 90% corrected speed, a nearly constant slope up to 70% of the passage is evident and then the slope suddenly increases and persists for the remainder of the passage. The increase in static pressure is smoother at 100% corrected speed.

Static pressures are measured at 99% of the impeller passage and are shown in Figure 5.13. Variations in pressure with circumferential position show the effect of the downstream diffuser vanes. An increase in pressure at about -20% of the diffuser passage indicates flow deceleration. This static tap pressure is affected by the diffuser vane, which causes the flow to decelerate with an accompanying increase in the static pressure. Further across the vane passage, a drop in the static pressure is measured. This indicates that flow over this static tap is moving through the middle of the diffuser passage where the least blockage is present. Because of the reduced blockage, high velocities exist at this location along with a corresponding reduction in static pressure. Further along the vane passage, the static pressure increases, indicating the higher blockage at the diffuser entrance on the adjacent vane.

5.3 Diffuser Performance

5.3.1 Diffuser Inlet Conditions

At the inlet of the diffuser, the total temperature distributions at 30 and 210 degrees have been measured and are shown in Figures 5.14 and 5.15 with the uncertainty within the symbol size. Good agreement in the diffuser inlet profile is measured between both locations. The total temperature increases with increasing span. Unequal work is performed on each stream tube through the impeller resulting in the uneven total temperature distributions at the impeller exit despite a relatively uniform impeller inlet total temperature distribution. More work is performed on the air closest to the shroud, resulting in high temperatures at higher spans. The total temperature profile remains a consistent shape but increases in magnitude at higher speeds because of the additional work done on the flow.

The diffuser inlet total pressure profiles at 30 and 210 degrees are shown in Figures 5.16 and 5.17 with uncertainty within the symbol size. Similar to the total temperature profiles, different work performed along each streamline within the impeller causes a variation in the total pressure profile at the measurement location. In addition to the different work input, each streamline experiences different losses and regions of blockage. A combination of these effects result in the present total pressure distributions. At both locations, high total pressures occurs in the middle of the passage where the flow losses are the smallest. A drop in total pressure is consistently measured at the lowest spanwise location across the operating range because of the strong endwall losses at the hub of the impeller. Lower pressures are also experienced because less work is done at the hub, indicated by lower total temperature in this region. Additional losses at the shroud endwall result from the tip leakage flow resulting from the impeller clearance a cause higher losses and a reduced total pressure in this region. Though the trends in the two distributions remain the same, there is some slight discrepancy between the 30 and 210 degree locations. Though similar total temperature profiles indicate the same work is being done, the 30 degree location indicates a lower total pressure revealing additional losses.

The results of the shroud CMM measurements were revisited to determine the cause of these increased losses. Figure 5.18 shows the measured shroud deviation from design intent at the end of the abradable. At lower angles, the axial distance is 0.0015 in less than nominal, indicating a larger clearance. Around 100 degrees, the axial distance increases, growing closer to the nominal distance and decreasing the tip clearance. The 210 degree circumferential location shows an axial distance of 0.0005 in less than nominal, indicating that the clearance gap has closed by 0.001 in. Because of the reduced clearance gap, the losses near the shroud are reduced, explaining the difference between the total pressure distributions at the inlet of the diffuser.

Figure 5.19 shows the distribution of the static pressures at the throat of the diffuser at two circumferential locations, 30 and 200 degrees, for several points on the operating line with uncertainty within the symbol size. At the exit of the impeller, the fluid has accumulated angular momentum in the counterclockwise direction. A region of high pressure is created on the blade surface as the fluid impinges on a diffuser vane and becomes redirected within the vane passage. Conversely there is a region that is somewhat “protected’ from the impeller discharge, creating a low pressure region. This flow phenomenon is evident in the throat which shows an increasing static pressure on the pressure side of the vane passage. Despite similar trends at 30 and 200 degrees, there is a difference between the two measurement locations, with the first location typically showing lower pressure compared to the second. This discrepancy could be related to the downstream instrumentation. One of the five total pressure rakes at the beginning of the deswirl section is downstream of the 30 degree location immediately after the turn to axial. This probe introduces flow blockage within this passage and thus affects the aerodynamics upstream in the diffuser. The difference between this location and the 200 degree location, where the probe is absent, is compared in Figure 5.20.

5.3.2 Diffuser Exit Conditions

The discrepancy between vane passage static pressures persists through the diffuser. Diffuser exit static pressures within the same vane passages, shown in Figure 5.21 with the uncertainty within symbol size, indicate a larger difference between the passages at the diffuser exit. This is attributed to the downstream pressure rake which causes a blockage in the 30 degree passage. Despite the difference between the two passages, the profiles at each speed remain consistent. As the air decelerates through the diffuser, the variation across the passage reduces, resulting in a more uniform vane-to-vane static pressure profile at the diffuser exit. Additionally, the deceleration causes the intended static pressure rise which can be found by comparing to the throat static pressures. This diffusion is larger at higher speeds, increasing the static pressure by 25% of inlet pressure at 70% corrected speed to 60% of inlet pressure at 100% corrected speed.

Figure 5.22 shows the total pressure distributions at the exit of the diffuser. Eight total temperature rakes at four different diffuser passage locations monitor the spanwise diffuser exit distribution with an uncertainty within the symbol size. Consistent throughout the profiles at all speeds, the midpassage rakes at 35.7% and 59.5% passage show an overall higher total pressure than those closer to the surfaces of the diffuser vanes. The air at these location experience the least losses. The rakes located closer to the vanes show a lower total pressure profile than that of the mid passage because of the wakes. In addition to the variations measured at the different passage locations, there are variations of total pressure with span throughout all profiles. Endwall losses at the hub and shroud of the passage cause a total pressure reduction in these areas. Even greater deviations across the span occur at higher speeds. The difference between the 70% corrected speed and 100% corrected speed highlights this, where the lower speed distribution deviates approximately 3.5% of the mean total pressure and the higher speed distribution deviates approximately 4.2% of the mean total pressure.

5.4 Compressor Exit Pressures

5.4.1 Turn to Axial

Next, air enters the turn-to-axial annulus where static pressures are measured along the inner and outer radii with uncertainty within the symbol size. Figure 5.23 shows how the percentage along the passage is defined, with the 0% corresponding to the inlet of the turn to axial and 100% corresponding to the beginning of the axial section. Figure 5.24 shows this distribution, normalized by the impeller inlet area averaged total pressure. Because of the curvature of the flow direction, a lower pressure on the inner radii is measured. Between the first and second static pressure taps on the outer surface, the radius of curvature increases, causing the rise in static pressure between the two passage locations. Toward the end of the turn-to-axial passage where the final static tap is located, the flow is almost completely axial and the flow path has an increased radius of curvature than that at the second pressure tap. This radius increase results in a static pressure drop from the second location because the flow experiences less turning.

5.4.2 Deswirl

Immediately following the turn to axial are the five total pressure rakes spanning the annulus and verifying circumferential uniformity at the exit. The spanwise deswirl total pressure distributions normalized by the impeller inlet area average total pressure are shown in Figure 5.25 with their uncertainty within the symbol size. They also provide insight on the change in distribution as the flow passes through the turn to axial.

Comparing Figure 5.25 to the diffuser exit profiles in Figure 5.22, two main phenomena are observed. First, an overall total pressure loss is measured through the turn to axial section. This is caused by the irreversibilities experienced as the flow is redirected toward axial. Second, more uniform profiles are shown at all circumferential locations. This indicates that the turn to axial section provides mixing to the flow, equalizing and settling the flow.

The total temperature distributions at the exit of the deswirl section indicate uniform total temperature profiles across all speeds and are shown in Figure 5.26, with a representative uncertainty bar displayed. With no work input into the flow, ideally the total temperature within the flow path should remain the same but this is not the case. A small loss in the average compressor temperature of less than 1% of the average inlet total temperature is evident by comparing Figure 5.26 and the diffuser inlet total temperature distribution in Figures 5.14 and 5.15. This reduction is caused by heat transfer from the high temperature fluid through the shroud to the ambient air. The comparison between these figures also shows the mixing and equalization of the flow that has occurred. While the diffuser inlet showed strong increase in total temperature with span, the deswirl exit reveals significantly more uniform profiles.

5.4.3 Backface Bleed

Static pressures taps along the stationary backface show the pressure distribution as a function of the radius. Figures 5.27 and 5.28 show these static pressures at 90 degree and 270 degree circumferential location with an uncertainty within the symbol size. A similar trend at these two locations is shown where a decrease in the measurement radius shows decreasing pressure. This trend indicates the expected acceleration of the exiting flow with decreasing radius. Though the two lower radii show consistent similar values between the circumferential locations, at the 270 degrees circumferential location, the largest radii has significantly higher pressures than its counterpart at 90 degrees.

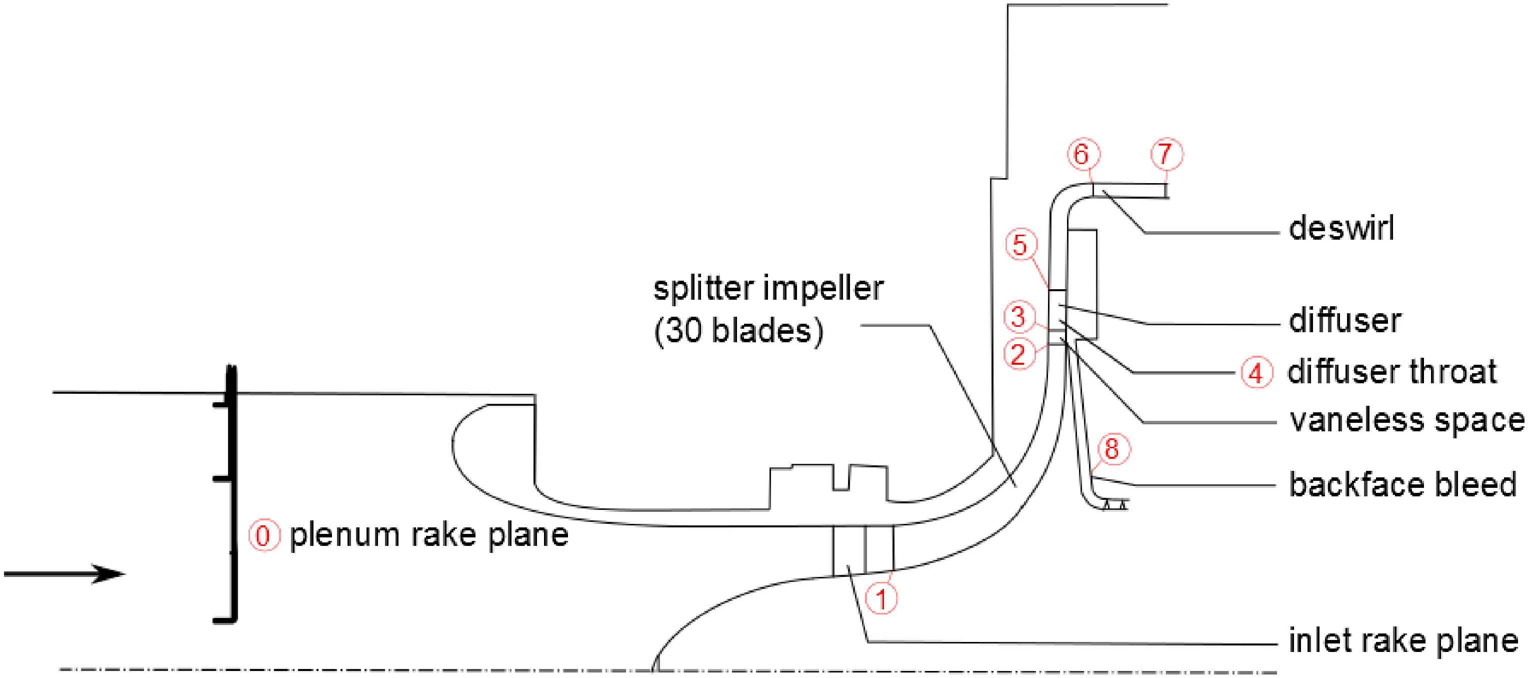

Figure 5.1: Compressure Measurement Stations.

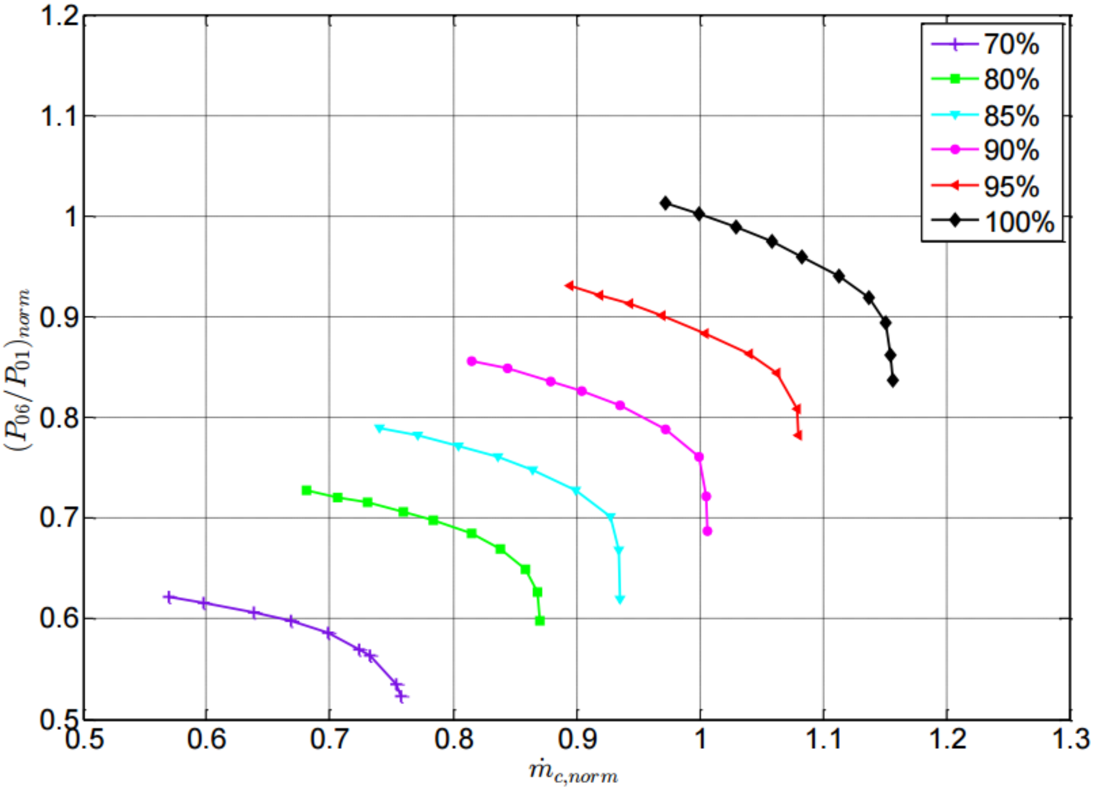

Figure 5.2: Compressor Performance Map.

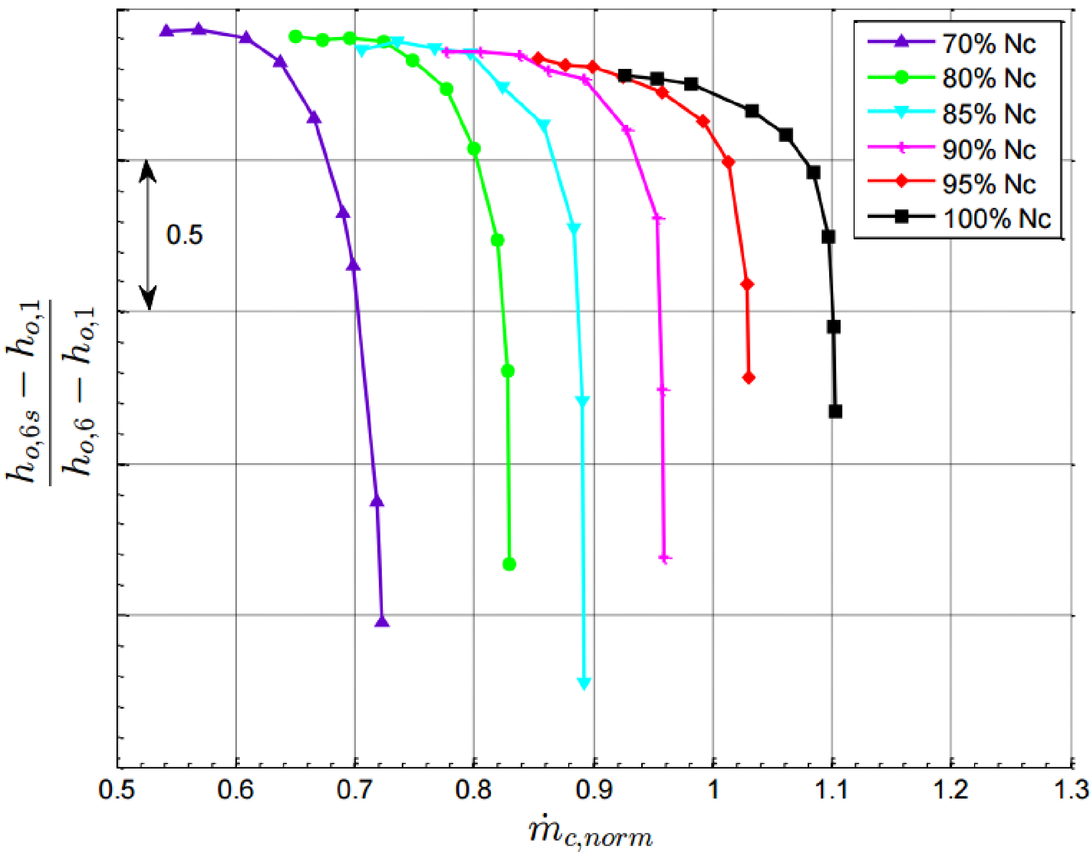

Figure 5.3: Compressor Efficiency Map.

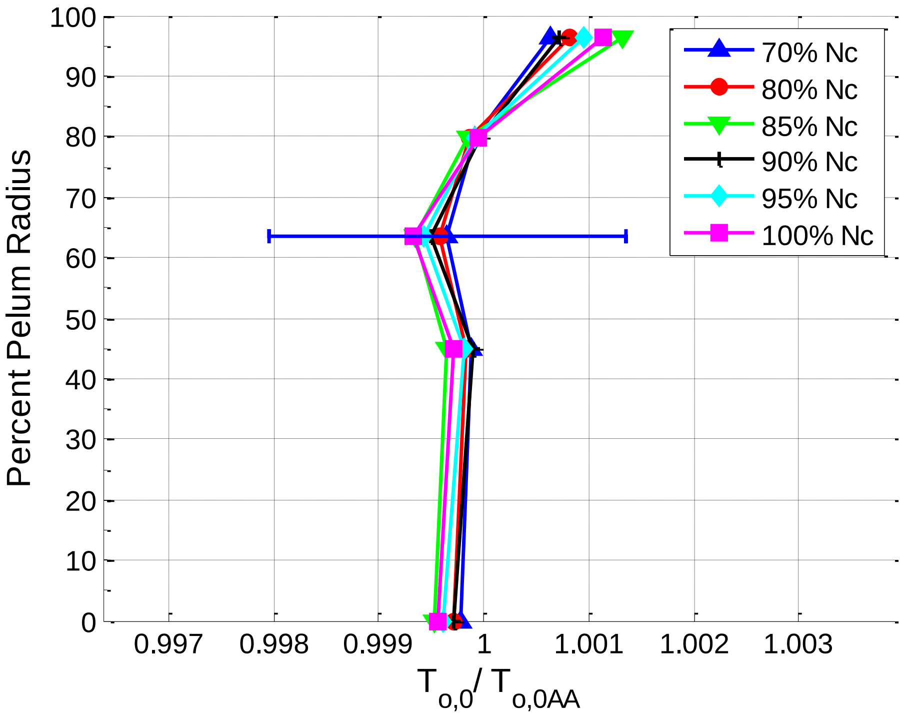

Figure 5.4: Plenum Total Temperature Distribution.

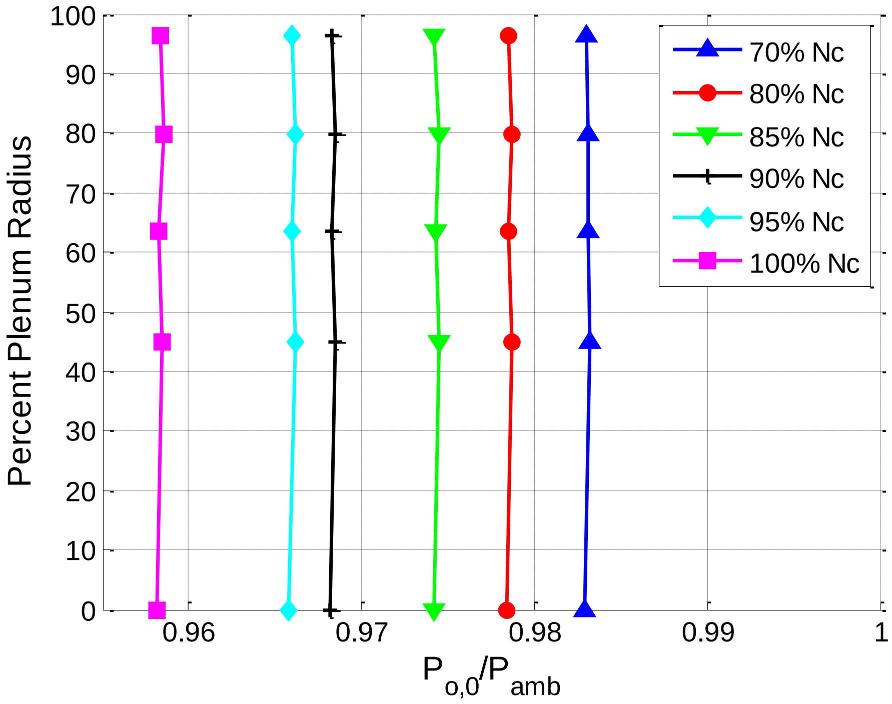

Figure 5.5: Plenum Total Pressure Distribution.

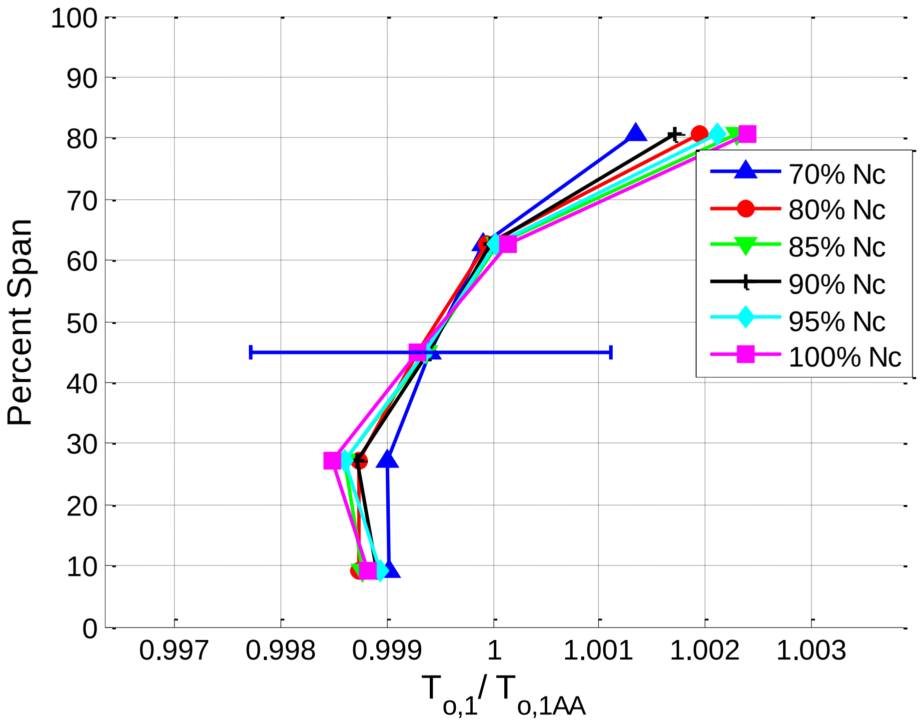

Figure 5.6: Inlet Plane Total Temperature Distribution, 150°.

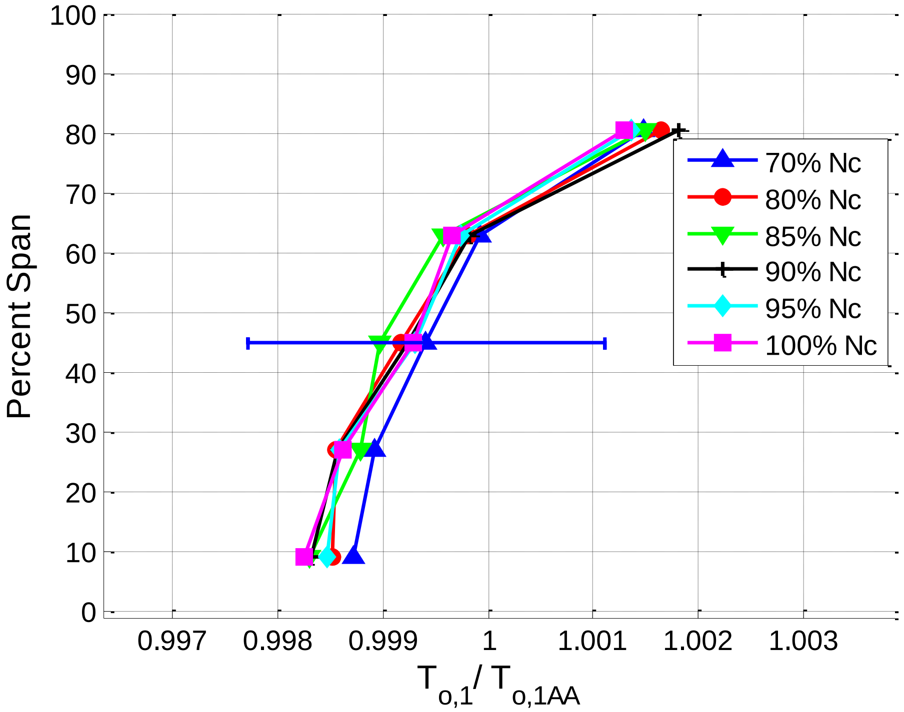

Figure 5.7: Inlet Plane Total Temperature Distribution, 330°.

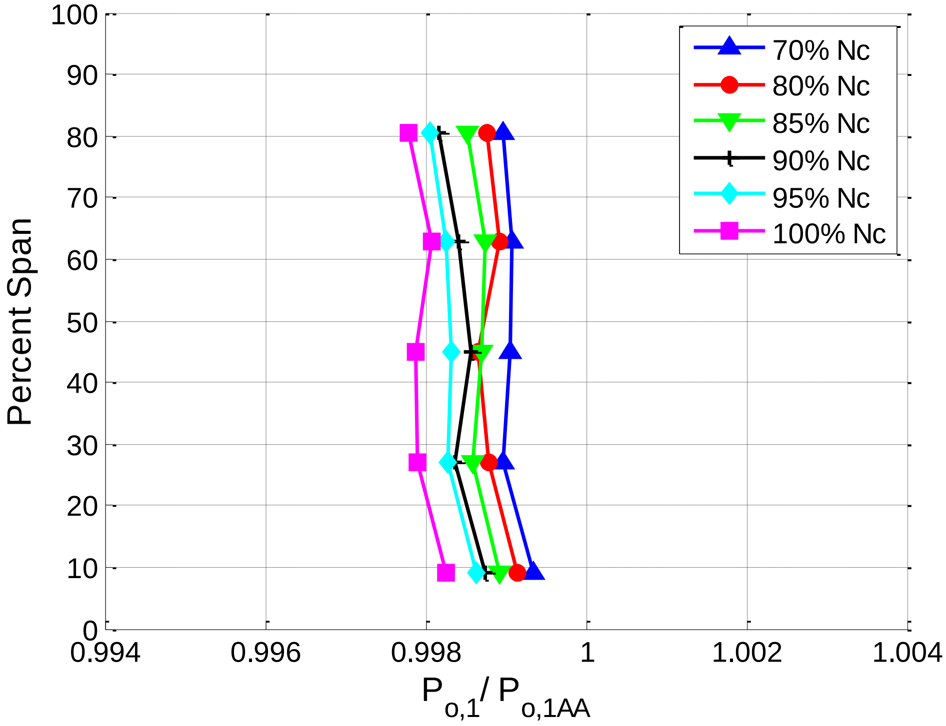

Figure 5.8: Inlet Plane Total Pressure Distribution, 30°.

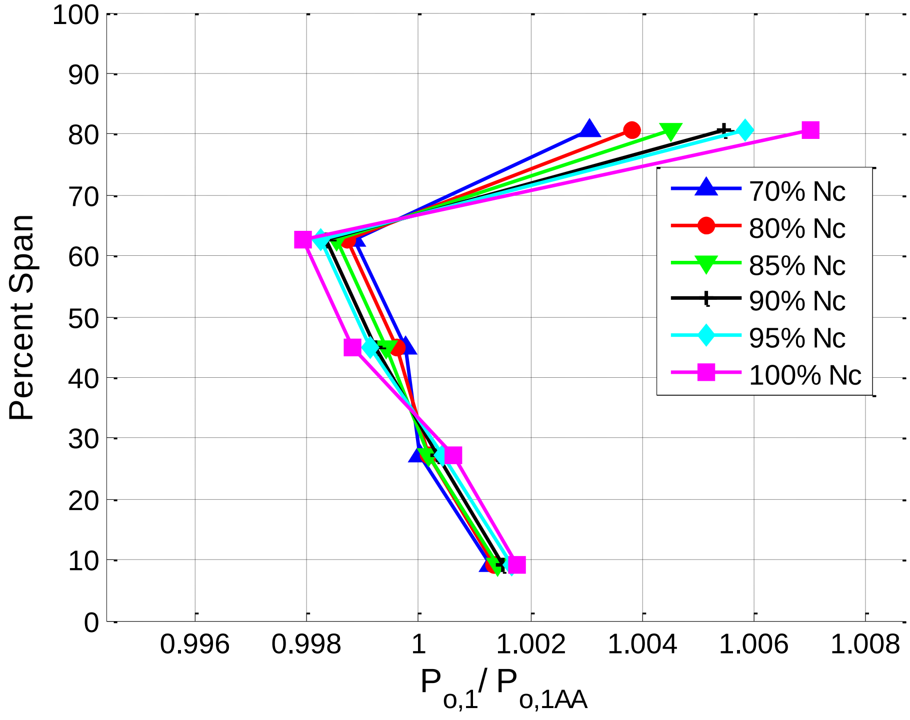

Figure 5.9: Inlet Plane Total Pressure Distribution, 210°.

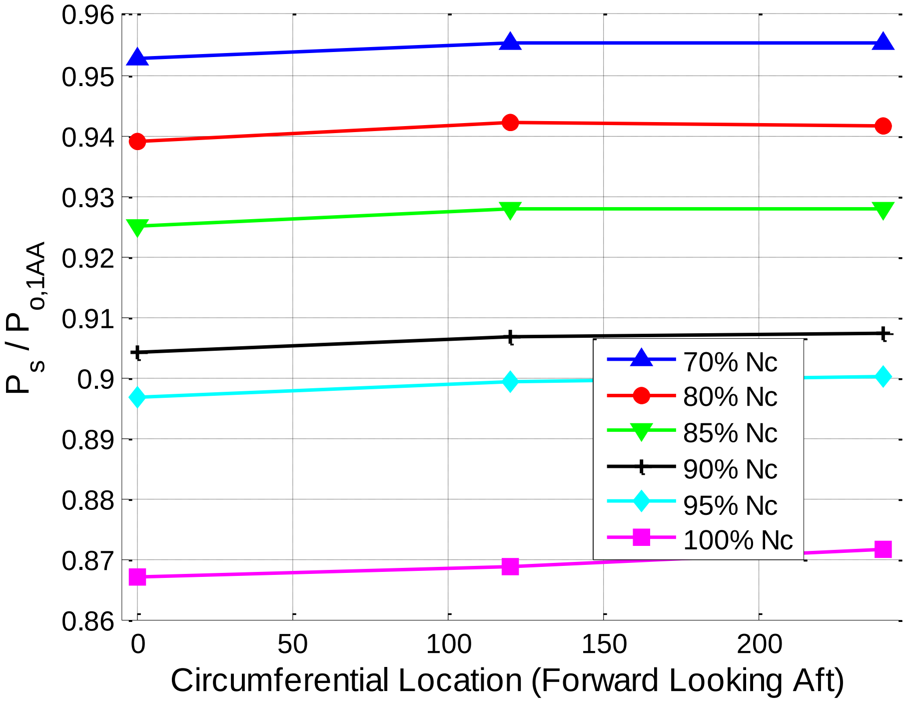

Figure 5.10: Static Pressure Upstream of Impeller.

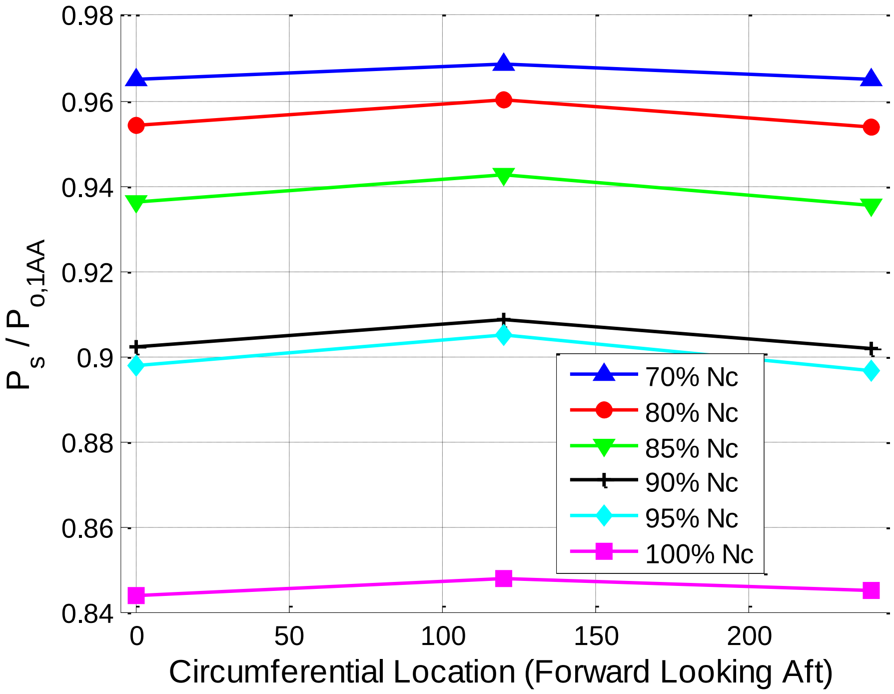

Figure 5.11: Static Pressure Downstream of Impeller Leading Edge.

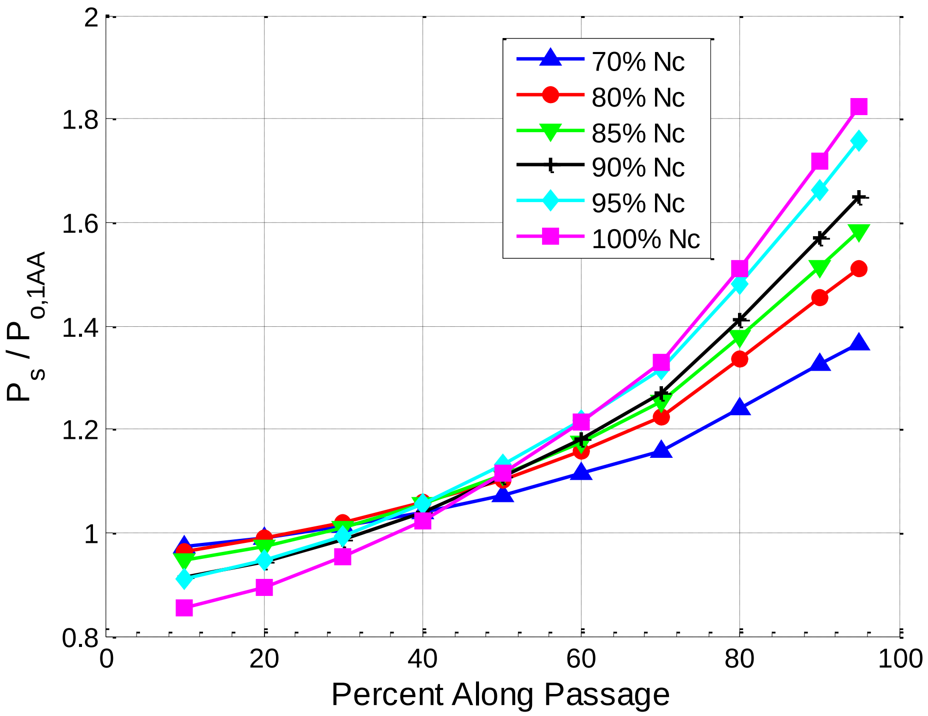

Figure 5.12: Shroud TDC Static Pressures.

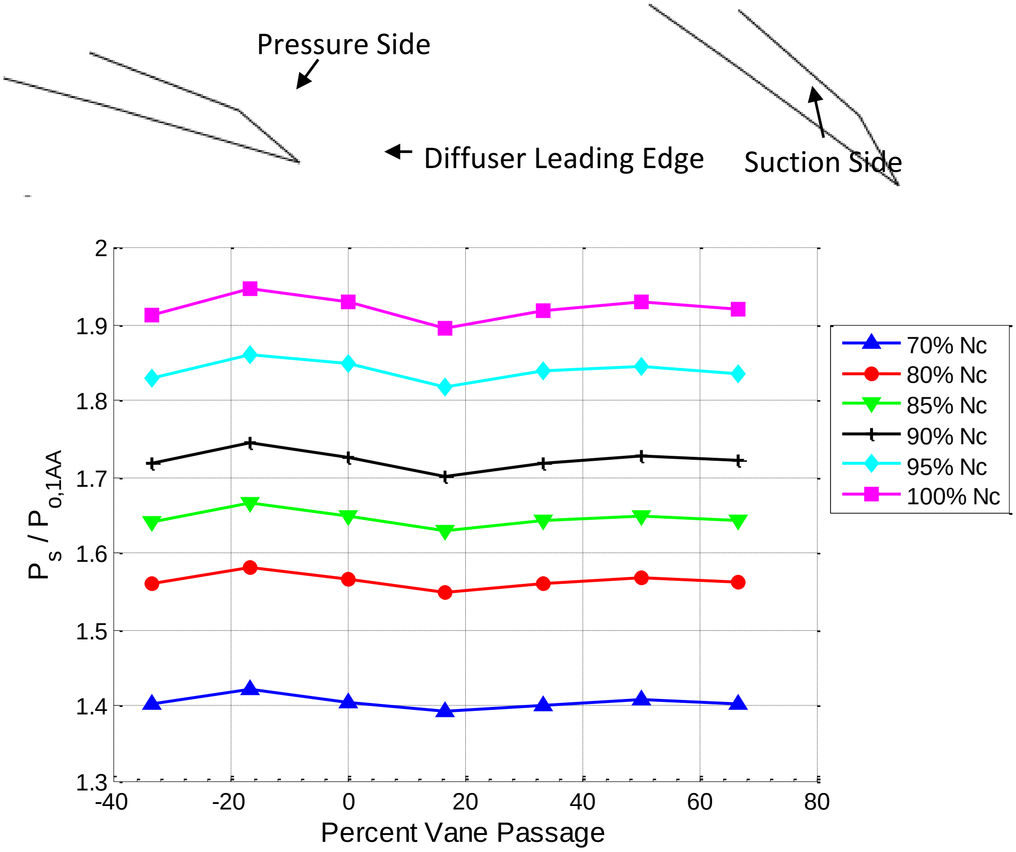

Figure 5.13: Shroud Static Pressures at 99% of the Impeller Passage.

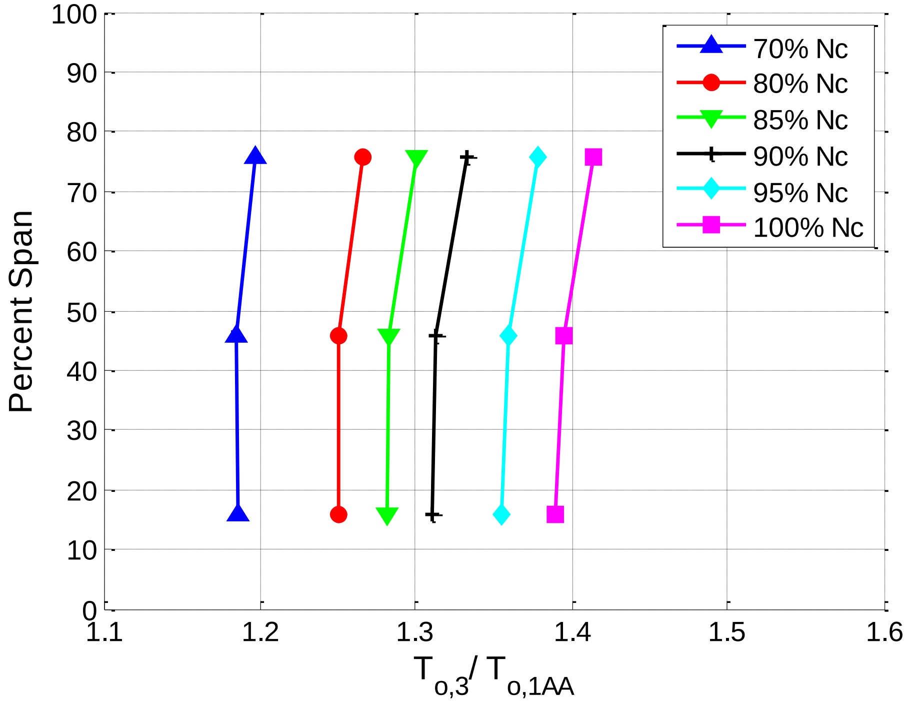

Figure 5.14: Diffuser Inlet Total Temperature Distribution, 30°.

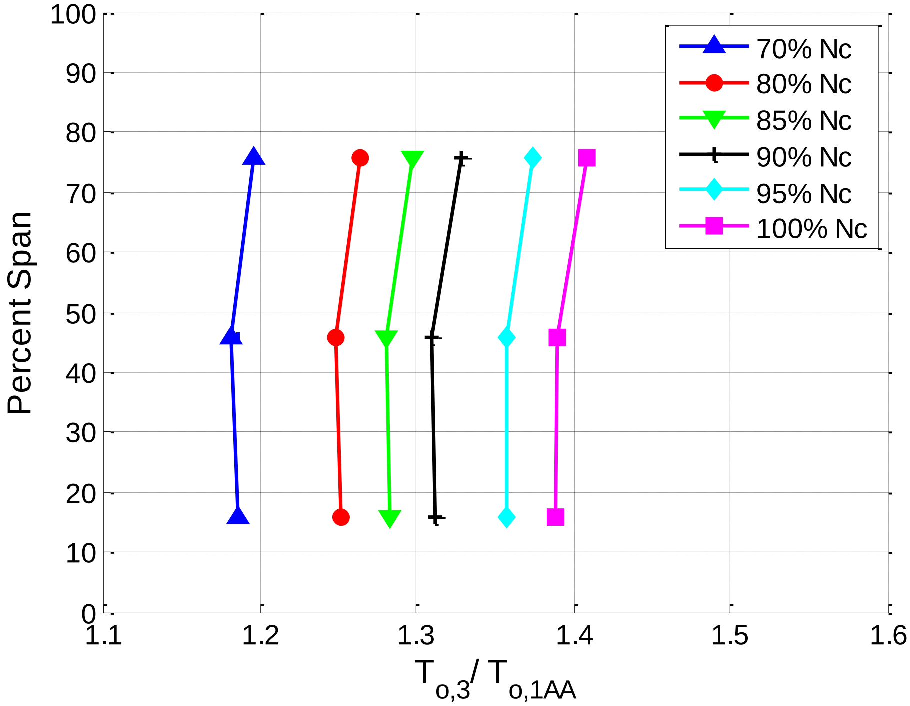

Figure 5.15: Diffuser Inlet Total Temperature Distribution, 210°.

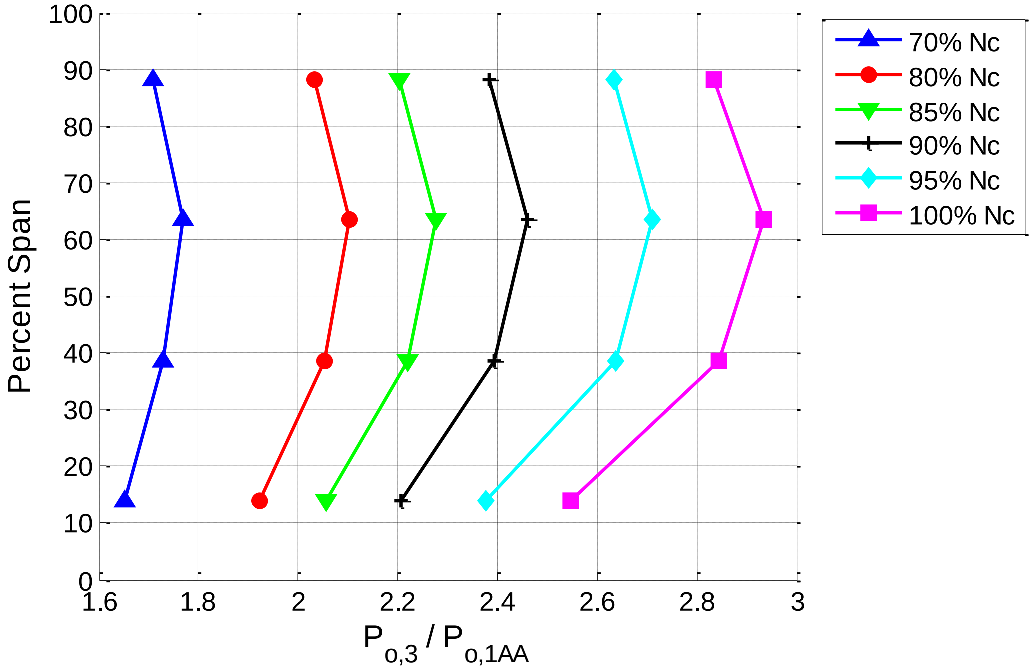

Figure 5.16: Diffuser Inlet Total Pressure Distribution, 30°.

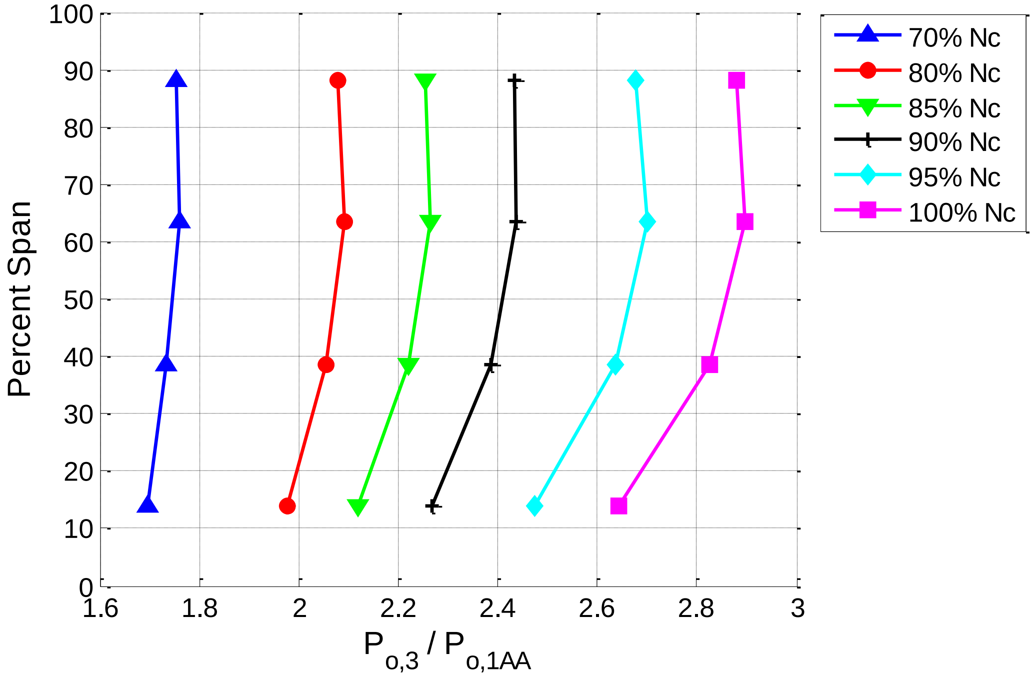

Figure 5.17: Diffuser Inlet Total Pressure Distribution, 210°.

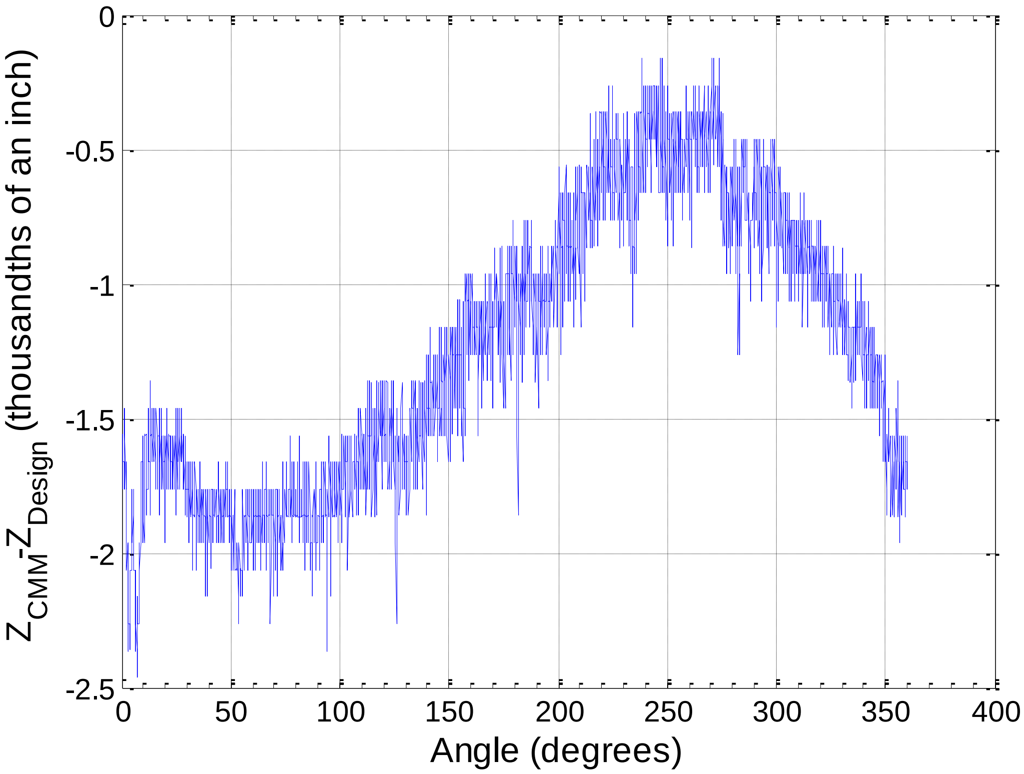

Figure 5.18: Axial Difference between Machined Shroud and Model at the Impeller Exit.

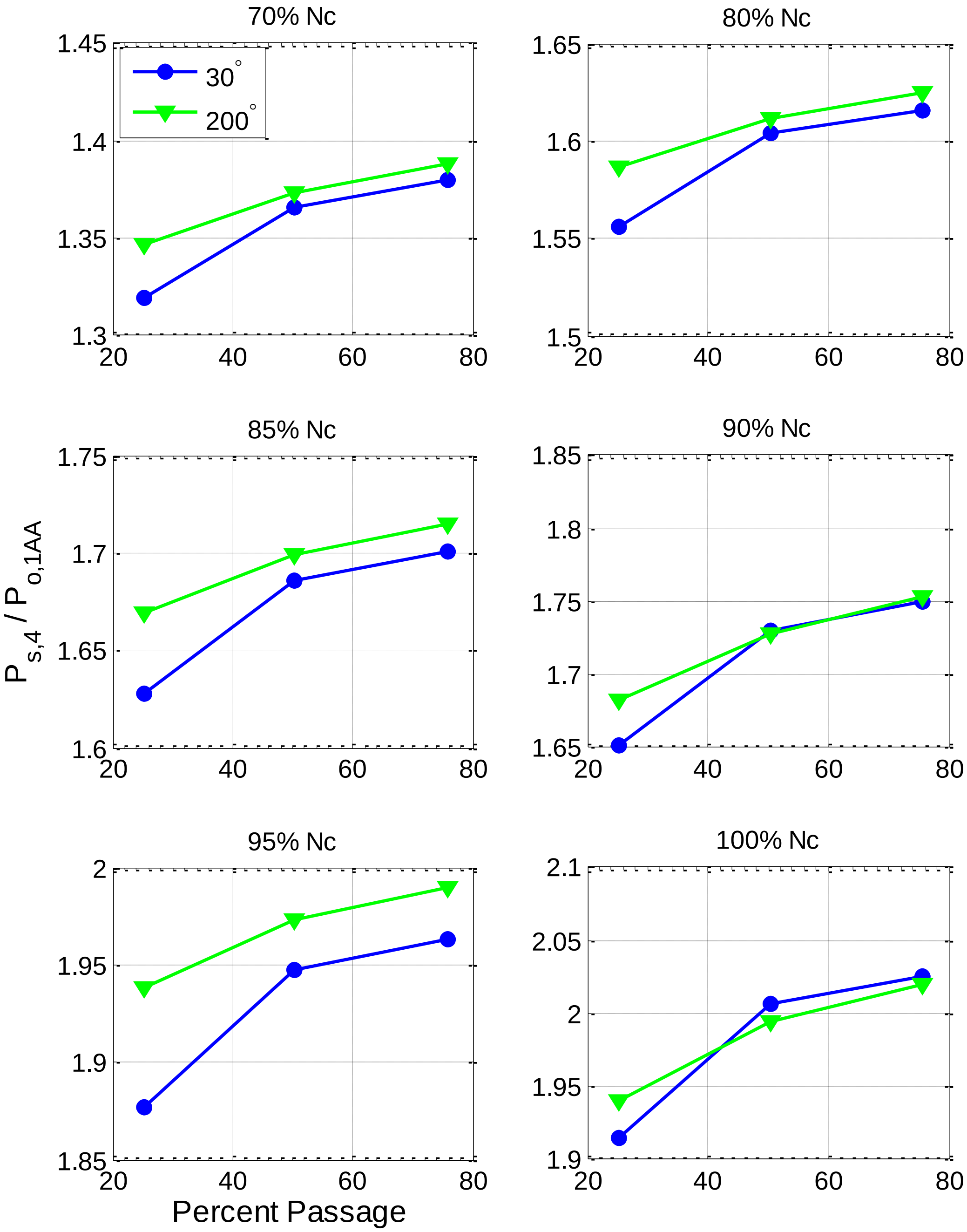

Figure 5.19: Diffuser Throat Static Pressure.

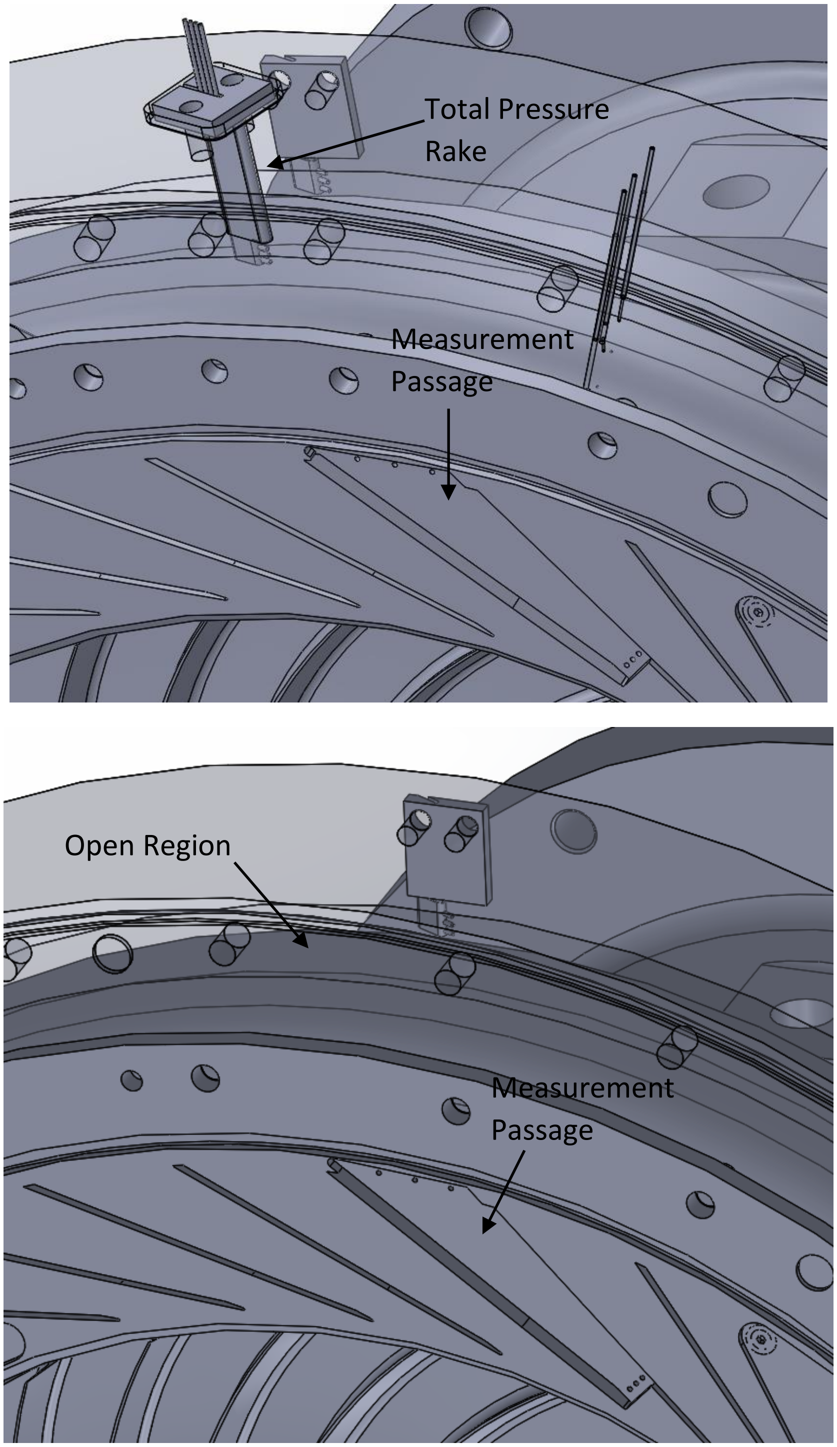

Figure 5.20: Difference between the 30° Diffuser Passage and 200° Passage.

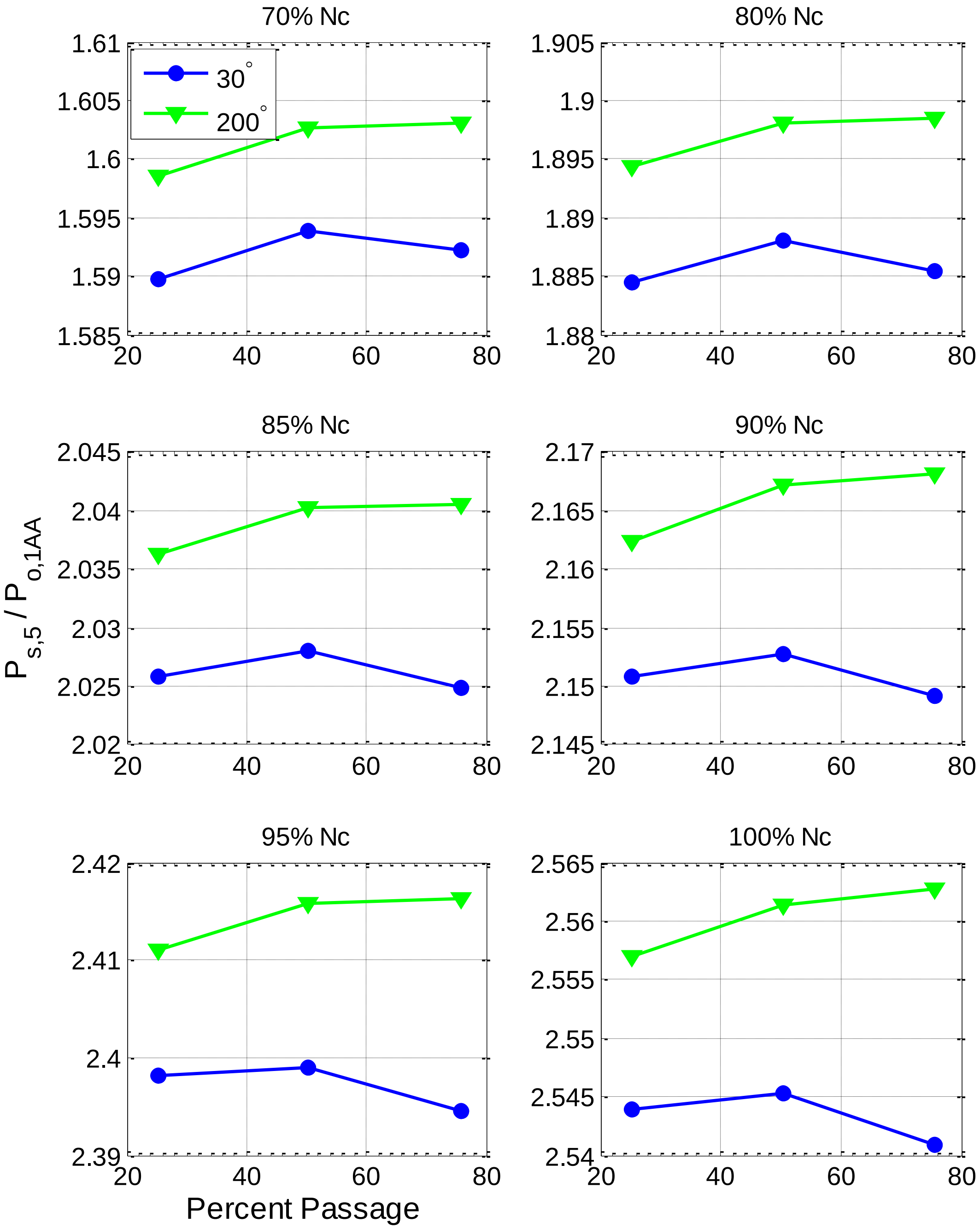

Figure 5.21: Diffuser Exit Static Pressure.

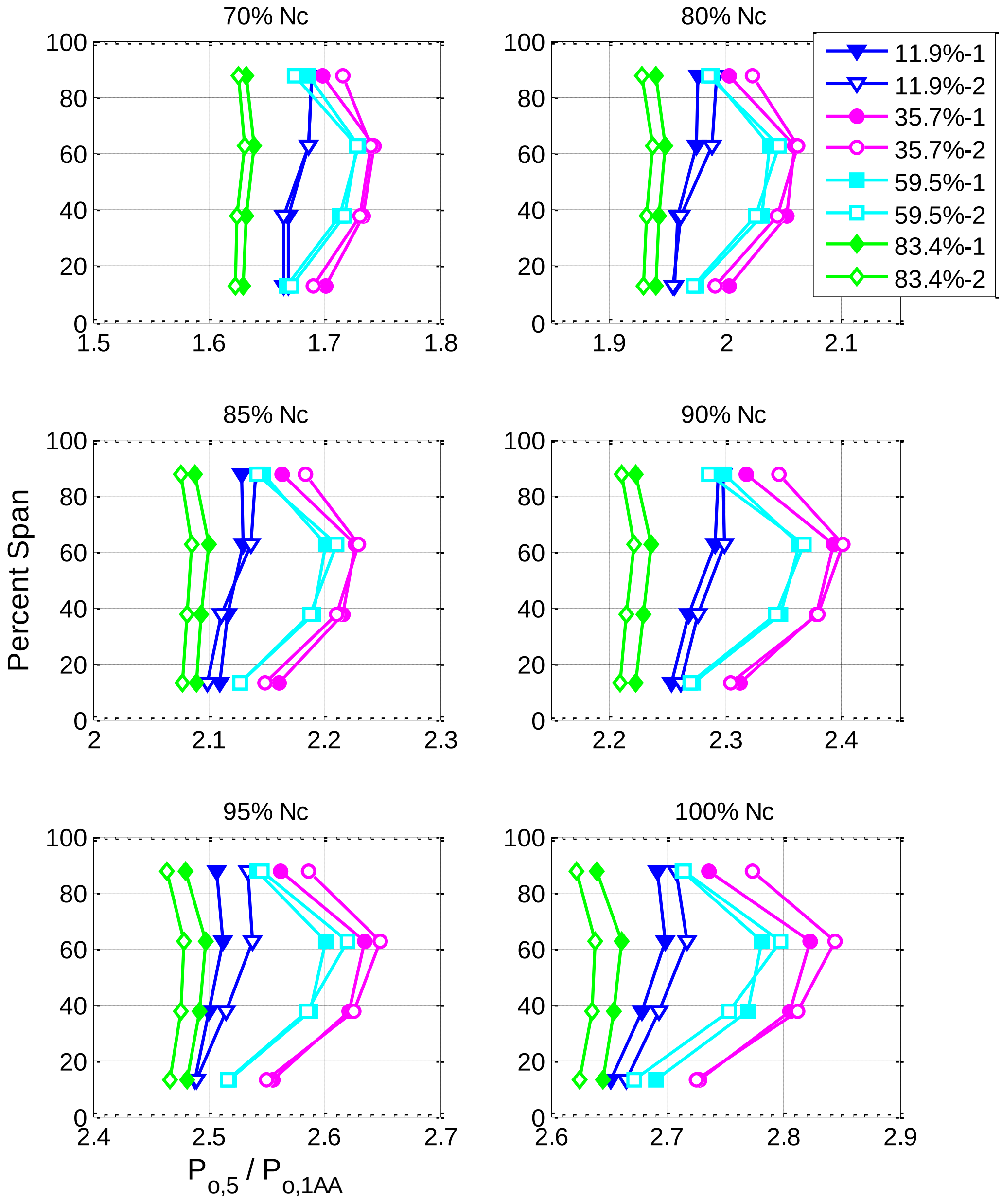

Figure 5.22: Diffuser Exit Total Pressure Profiles.

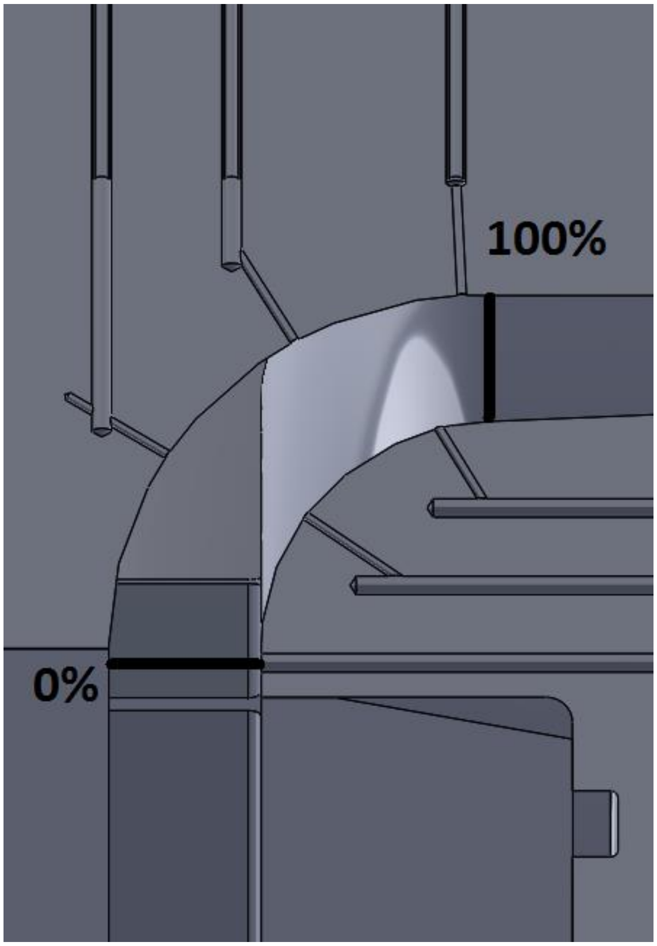

Figure 5.23: Definition of the Turn to Axial Percentage

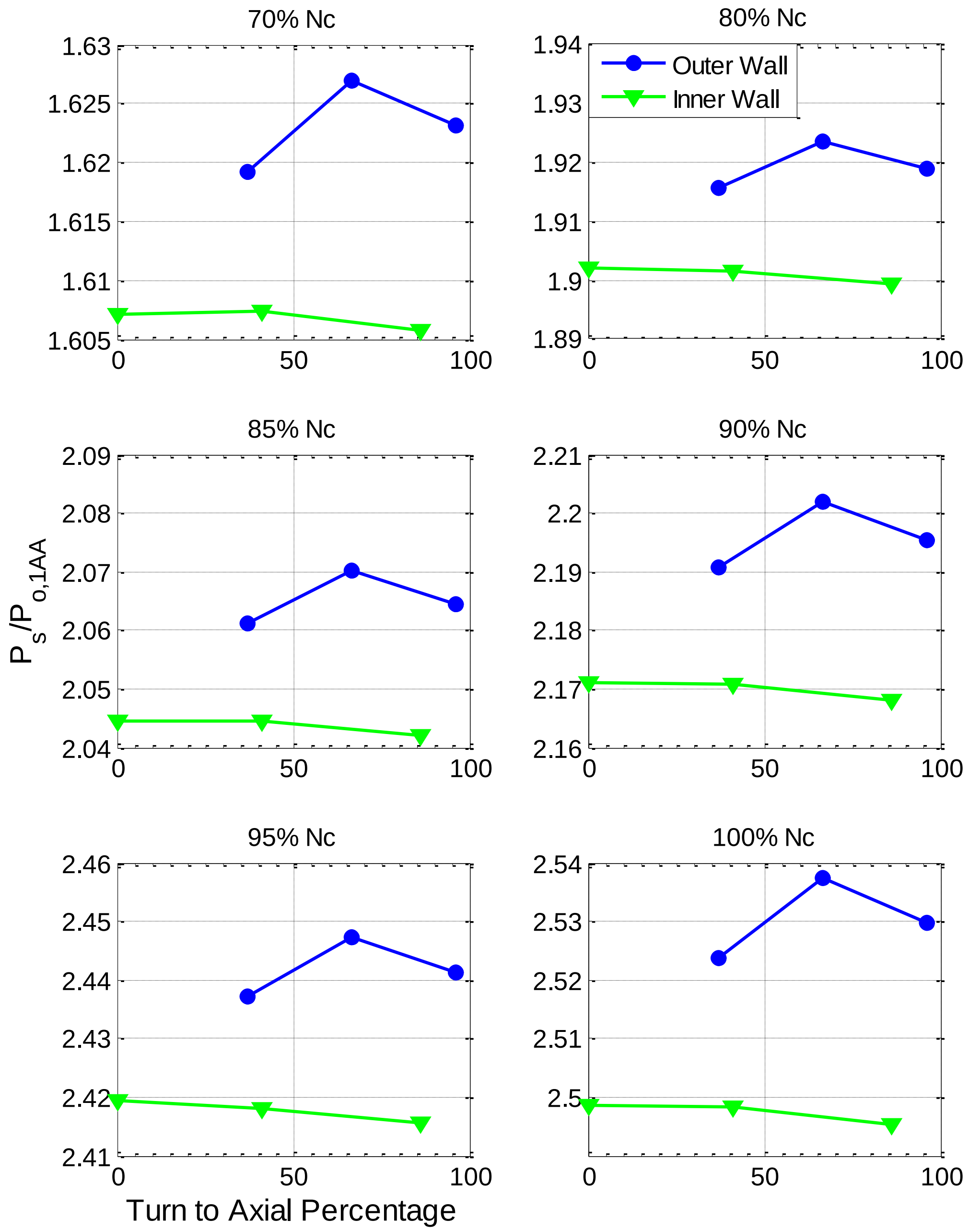

Figure 5.24: Turn to Axial Static Pressure Distribution.

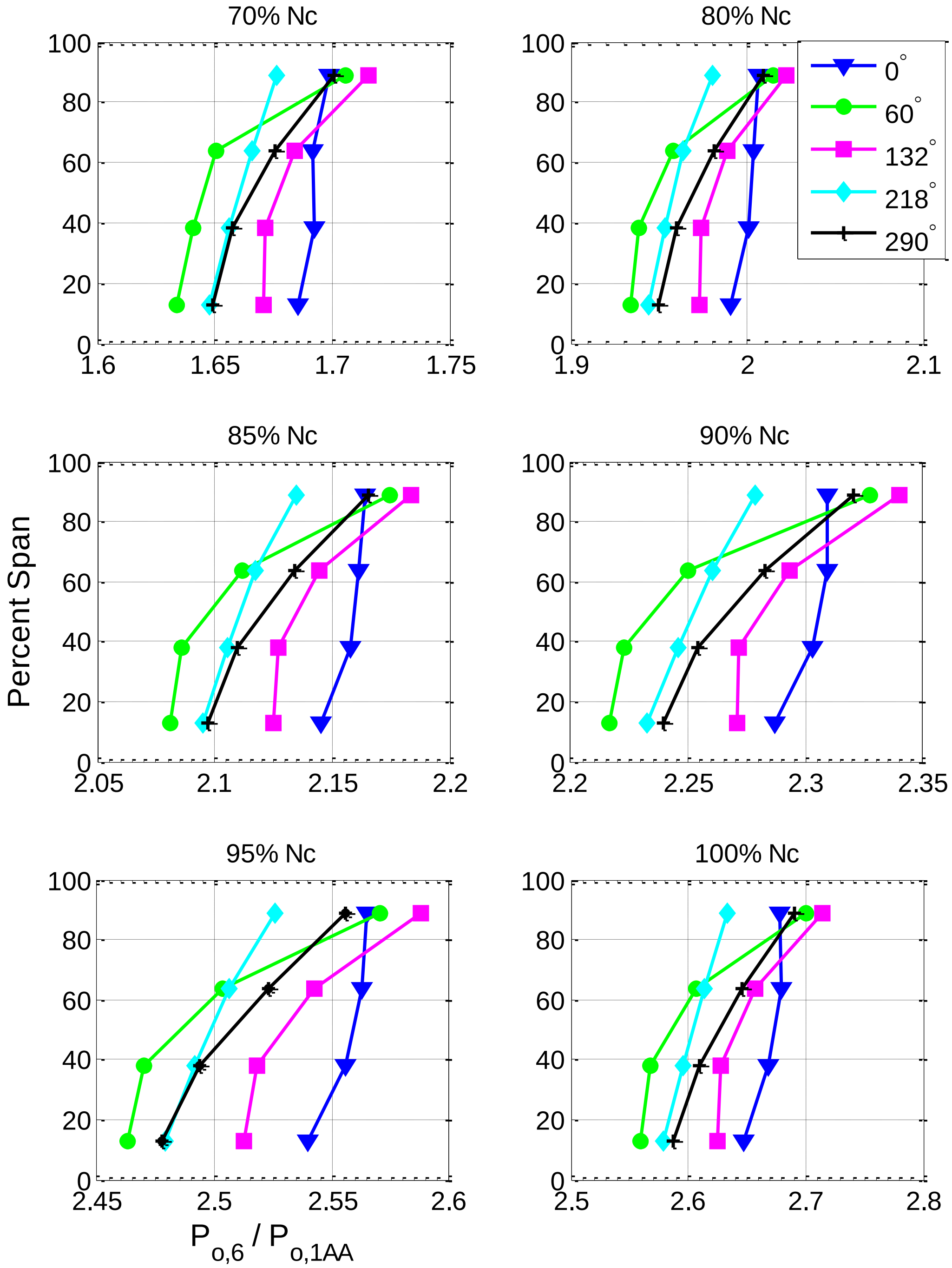

Figure 5.25: Deswirl Inlet Total Pressure Distribution.

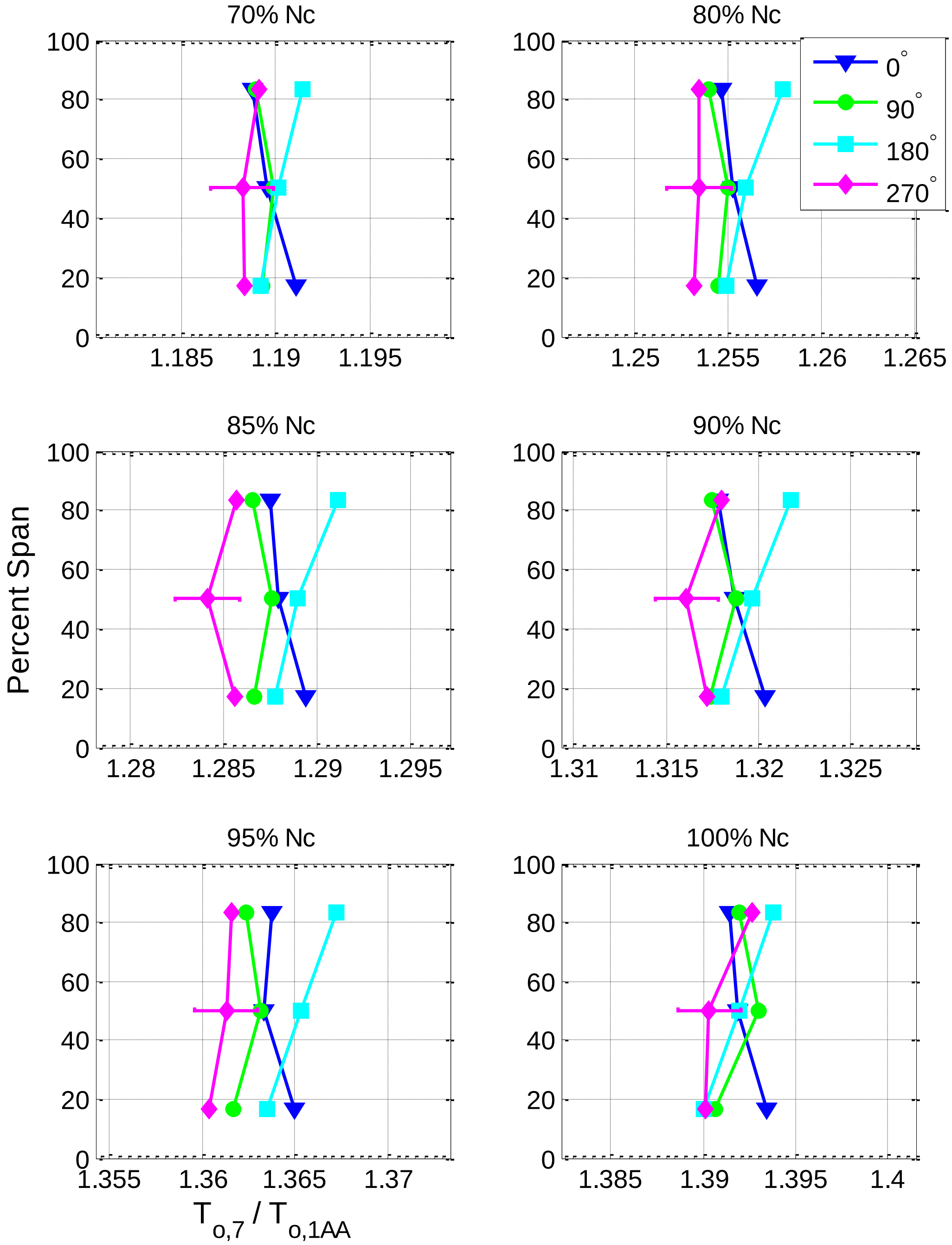

Figure 5.26: Deswirl Exit Total Temperature Distribution.

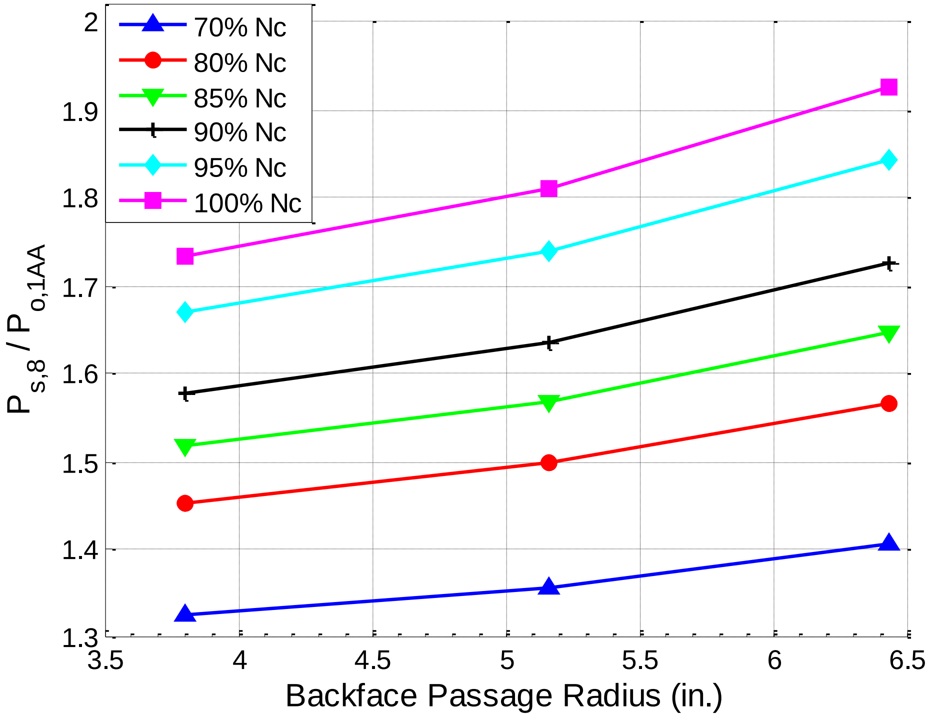

Figure 5.27: Backface Bleed Pressure at 90°.

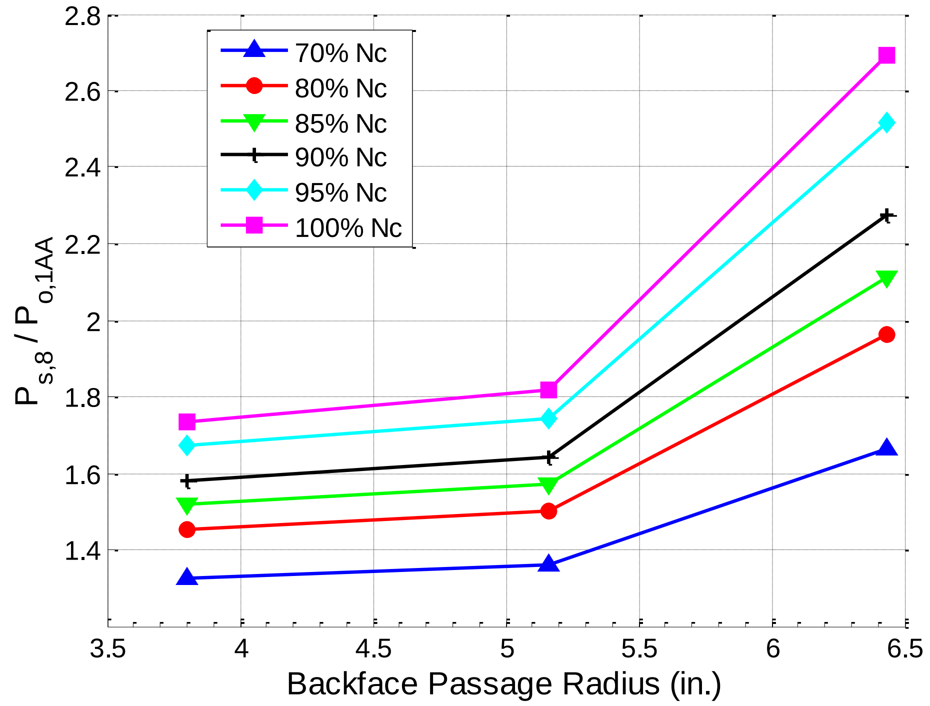

Figure 5.28: Backface Bleed Pressure at 270°.

CHAPTER 6: CONCLUSIONS AND RECOMMENDATIONS

6.1 Summary

Though CFD tools can be used to provide valuable insight and direction for modern compressor design, experimental results are needed to verify the efficacy of new designs and the accuracy of the computational methods. A new compressor research facility, the Centifugal STage for Aerodynamic Research compressor, has been designed and tested. The CSTAR facility located at Purdue's Zucrow Labs will support research investigations on centrifugal compressor performance.

The compressor is driven using a 1400 hp motor and an intermediate gearbox to reach the design speed of 22,500 RPM. The exit of the gearbox interfaces with the compressor's impeller through a driveline designed to mitigate any mechanical issues or vibrations.

At the inlet of the facility, air is settled and enters the inlet piping that leads to the compressor. Through this inlet piping, the mass flow rate is measured using an ASME-standard long-form venturi and is then conditioned, after passing through two bends to provide uniform inlet flow to the compressor. Once the fluid is directed through the impeller annulus, inlet rakes are used to determine the compressor inlet flow condition. Air then enters the impeller where static taps located along the shroud are used to measure the pressure rise as work is being done on the fluid. Additional static taps are located at the impeller exit that provide insight into the potential flow fields caused by the downstream diffuser vanes. Variations in static pressure show where the air is being slowed by the diffuser vanes and where it is accelerated through the passage.

Air then enters the diffuser, which is heavily instrumented to provide insight into the aerodynamics of the fluid deceleration and static pressure growth. Total temperature and pressure are measured at the vane leading edge to quantify the impeller’s performance and the diffuser spanwise profile. Static taps at the throat and exit also show the pressure distribution within the passage. Additionally, eight rakes at the exit placed at four different passage locations provide insight into the diffuser’s exit spanwise and vane-to-vane profiles. These rakes measure the total pressure distribution and indicate where losses are highest within the diffuser. The flow is then turned to axial, where taps along the inner and outer surfaces show how the pressure progresses through the turn. Finally, air enters the deswirl annulus which house both total temperature and pressure rakes. These rakes are used to quantify the overall performance of the compressor and determine its efficiency and pressure ratio. Air then moves into the collector and is exhausted to ambient.

In addition to these measurements, the compressor has been designed to house capacitance probes that measure the tip clearance throughout operation. To obtain trusted results, many factors of the capacitance probe installation and data processing were investigated. Because probe placement within the shroud was sensitive to subtle differences in installation procedures, a standard was established to repeatably install the instrumentation flush with the flow path. An in-situ calibration of all the probes was performed using a custom calibration stand. Development of these processes resulted in a system that can repeatably and accurately measure the impeller tip clearance.

Temperature fluctuations at the compressor inlet were also significantly reduced to keep the corrected speed within the designated tolerance. High winds outside of the test cell combined with shedding from the heat exchangers caused abrupt changes in incoming air temperature at the bellmouth. A large settling chamber was constructed to dampen the effects of the unstable ambient temperature on the compressor inlet conditions. In addition to allowing the air contained to equalize prior to ingestion, this chamber did not allow for ingestion of air passing over the heat exchangers, mitigating temperature oscillations caused by the structure’s hot exhaust air and shedding. The chamber has successfully reduced the fluctuations, making it possible to remain on a constant corrected speed line for long duration runs.

To facilitate future research that will utilize LDV measurements, a ray tracing analysis was performed on the shroud windows. Because of the compound curvature of the windows, the beam pairs for the probes do not align after passing through the window and significantly increase the size and uncertainty of the measurement volume. This can be corrected by using beam translators to adjust the angle of the lasers and will facilitate the corrections needed to realign of the beam pairs.

6.2 Recommendations

To facilitate future experiments in the compressor facility, some steps are recommended.

Some additional diagnostics should be performed to determine the source of the spanwise pressure nonuniformity at the 210 degree inlet total pressure rake. Though it looks as if a leak might be the cause, sealing the boot and bellmouth did not have an effect on the distribution. To determine if the flow is physical, the inlet rakes should be switched and the 30 degree rake should be placed at the 210 degree location. If the problem persists, the issue is physical and further investigation of the inlet should be performed. If the problem ceases, the rake itself was causing the issue and must be inspected.

With the backface bleed lines now only being routed and ejected to ambient, little control over their flowrate exists. Because the backface bleed mass flow rate effects the compressor performance, it is desirable to monitor and control them. Two miniature venturis and accompanying Rosemount pressure transducers have been purchased that can be used to determine the flowrate through each of the two bleed lines individually. In addition, regulators will be used throttle the impeller backface pressure and alter the exhaust mass flow. The regulators will be actuated from the control station so that multiple bleed line configurations can be tested in a continuous run.

Because of the consistent difficulties in setting corrected speed in the morning, it is recommended that testing primarily take place in the evening. Without the sun impinging on the inlet and causing sudden temperature fluctuations, it is much easier to remain on a constant compressor speed line. This will allow for collection of consistent compressor data and eliminate the issue of regularly changing mechanical speed to match the corrected speed line.

Finally, with a calibration of the capacitance probes established, the current minimum tip clearance should be determined. Following this, the shim on the shroud seat should be adjusted to reduce the smallest impeller tip clearance to the desired value of 0.005 in. By changing this thickness, a comparison of the different tip clearance configurations can be found and the clearance effect on the compressor performance can be quantified. In addition, the variations between the two sets of measurement points will shed light on how the tip clearance reduction alters the aerodynamics of the CSTAR compressor.

LIST OF REFERENCES

LIST OF REFERENCES

[1] M. Wan, “Forced Induction,” *Autozine*, 2011. [Online]. Available: http://www.autozine.org/technical_school/engine/Forced_Induction_1.html. [Accessed: 06-Jan-2015].

[2] J. J. Brasz, “Aerodynamics of Rotatable Inlet Guide Vanes for Centrifugal Comprssor.pdf,” 1996.

[3] D. Eckardt, “Detailed Flow Investigations Within a High-Speed Centrifugal Compressor Impeller,” *J. Fluids Eng.*, vol. 98, no. 3, p. 390, 1976.

[4] D. Eckardt, “Instantaneous Measurements in the Jet-Wake Discharge Flow of a Centrifugal Compressor Impeller,” *J. Eng. Power*, vol. 97, no. 3, p. 337, 1975.

[5] R. C. Dean, “Centrifugal Compressors and Pumps Losses an ¥ ane ! ess Dsffusers of,” *J. Eng. Gas Turbines Power*, 1996.

[6] H. Krain, “A Study on Centrifugal Impeller and Diffuser Flow,” *J. Eng. Power*, vol. 103, no. 4, p. 688, 1981.

[7] N. A. Cumpsty, “Compressor Aerodynamics,” p. 252, 2004.

[8] D. Japikse, *Centrifugal Compressor Design and Performance*. Concepts ETI, Inc., 1996.

[9] G. J. Skoch, “Aerodynamic Performance of a Compact, High Work - Factor Centrifugal Compressor at the Stage and Subcomponent Level,” pp. 1–19, 2014.

[10] R. Fleming, “The Design and Performance of Centrifugal Compressor Research Facility,” Purdue University, 2010.

[11] Y. Senoo and M. Ishida, “Pressure Loss Due to the Tip Clearance of Impeller Blades in Centrifugal and Axial Blowers,” *J. Eng. Gas Turbines Power*, vol. 108, no. 1, p. 32, 1986.

[12] G. J. Skoch and R. D. Moore, “Performance of two 10-lb/sec centrifugal compressors with different blade and shroud thicknesses operating over a range of Reynolds numbers,” 1987.

[13] G. Eisenlohr and H. Chladek, “Thermal Tip Clearance Control for Centrifugal Compressor of an APU Engine,” *J. Turbomach.*, vol. 116, no. 4, p. 629, 1994.

[14] D. (University of V. Sanadgol, “Active Control of Surge in Centrifual Compressors Using Magnetic Tip Clearance Actuation,” 2006.

[15] J. Brasz, “Investigation into the effect of tip clearance on centrifugal compressor performance,” *ASME, Gas Turbine Aeroengine Congr. Expo.*, no. ASME-Paper 88-GT-190, pp. 190–201, 1988.

[16] Y. Senoo and M. Ishida, “Deterioration of compressor performance due to tip clearance of centrifugal impellers.,” *Trans. Japan Soc. Mech. Eng. Ser. B*, vol. 52, no. 473, pp. 386–392, 1986.

[17] R. Kunte, P. Schwarz, B. Wilkosz, P. Jeschke, and C. Smythe, “Experimental and Numerical Investigation of Tip Clearance and Bleed Effects in a Centrifugal Compressor Stage With Pipe Diffuser,” *J. Turbomach.*, vol. 135, no. 1, p. 011005, 2013.

[18] a. Jaatinen-Varri, T. Turunen-Saaresti, P. Roytta, a. Gronman, and J. Backman, “Experimental study of centrifugal compressor tip clearance and vaneless diffuser flow fields,” *Proc. Inst. Mech. Eng. Part A J. Power Energy*, vol. 227, no. 8, pp. 885–895, 2013.

[19] M. Schleer, S. J. Song, and R. S. Abhari, “Clearance Effects on the Onset of Instability in a Centrifugal Compressor,” *J. Turbomach.*, vol. 130, no. 3, p. 031002, 2008.

[20] H. Ma, S. Li, and W. Wei, “Effects of probe support on the flow field of a low-speed axial compressor,” *J. Therm. Sci.*, vol. 23, no. 2, pp. 120–126, 2014.

[21] J. M. Filipenco, V, Johnston and E. M. Greitzer, “Unstead Flow Phenomena in Discrete Passage Diffusers for Centrifugal Compressors,” vol. 298, 1994.

[22] B. Heckaman, “Design of Optical Access for the Application of Laser Doppler Velocimetry in a Low Specific Speed Centrifugal Compressor,” Purdue University, 2014.

[23] ASME, “ASME PTC 19.5-2004 Flow Measurement,” 2005.

[24] M. O. Lemmon WE, Huber LM, “NIST reference fluid thermodynamic and transport properties-REFPROP,” 2007.

[25] Flatau, P.J., R. L. Walko, “Polynomial Fits to Saturation Vapor Pressure,” *J. Appl. Meteorol.*, no. 31, pp. 1507–1513, 1992.

[26] J. D. Wright, “Properties for Accurate Gas Flow Measurements,” in *15th Flow Measurement Conference (FLOMEKO)*, 2010.

[27] R. a. Berdanier, N. R. Smith, J. C. Fabian, and N. L. Key, “Humidity Effects on Experimental Compressor Performance—Corrected Conditions for Real Gases,” *J. Turbomach.*, vol. 137, no. 3, p. 031011, 2014.

[28] F. Lou, R. Fleming, and N. L. Key, “Calculating high speed centrifugal compressor performance from averaged measurements,” *Int. J. Turbo Jet Engines*, vol. 29, no. 4, pp. 289–298, 2012.

APPENDICES

APPENDIX: START-UP CHECKLISTS

List of Checklists

Checklist Rev. Data: 06/20/15

☐ A.1 Oil System Checklist

☐ A.2 Instrumentation Check List

☐ A.3 Miscellaneous Test Cell Start-Up Checklist

☐ A.4 Variable Frequency Drive (VFD) Start-Up Checklist

☐ A.5 Control Stand Start-Up Checklist

☐ A.6 Final Rig Start-Up Checklist

☐ A.7 Running Rig Checklist

☐ A.8 Rig Shut-Down Checklist

Oil System Checklist

Checklist Rev. Date: 06/20/15

☐ 1. Gearbox oil reservoir level at mid-level of indicator?

☐ 2. Gearbox oil system path fully assembled and tightened (follow pipes & check for open ports…)

☐ 3. Compressor oil system path fully assembled and tightened (follow pipes and tubes & check for open ports…)

☐ 4. Boost Pump Valve – Upstream **CLOSED**

☐ 5. Boost Pump Valve – Downstream **CLOSED**

☐ 6. Bottom Heat Exchanger Valve – Upstream **CLOSED**

☐ 7. Bottom Heat Exchanger Valve – Downstream **CLOSED**

☐ 8. Compressor Oil System Manual **OPEN**

☐ 9. Compressor Oil System 2-way valve **CLOSED**

☐ 10. Gearbox Oil Filters tightened down

☐ 11. Compressor Oil Filter tightened down

☐ 12. Heat Exchanger Type K Thermocouple 1 & 2 installed

☐ 13. Gearbox journal bearing type T thermocouples installed (Qty 4)

☐ 14. Gearbox manifold type K thermocouple installed

☐ 15. Gearbox manifold pressure sensor installed

☐ 16. Compressor manifold pressure sensor installed

☐ 17. Three pressure sensors installed on the compressor oil lines

☐ 18. Compressor exit oil type K thermocouple installed

☐ 19. Compressor bearing chip detector installed and wired

☐ 20. Secondary Tank level sensor installed, with it loosely tightened at top

☐ 21. Thermostat set at 110° F and installed in the gearbox

Instrumentation Checklist

Checklist Rev. Data: 06/20/15

☐ 1. Pitot probe pressure tubes installed
☐ 2. Pitot probe type T thermocouple installed
☐ 3. Hygrometer wired and mounted flush with inlet piping
☐ 4. Venturi meter pressure taps and tubes installed
☐ 5. Inlet plenum probes installed with O-Rings and bolts tightened
☐ 6. Inlet plenum pressure tubes installed
☐ 7. Inlet plenum type K thermocouples installed
☐ 8. Inlet rake and inlet static tap pressure tubes installed
☐ 9. Inlet rake type T thermocouples installed
☐ 10. Shroud static tap pressure tubes installed
☐ 11. Diffuser inlet rakes pressure tubes installed
☐ 12. Diffuser inlet rakes type T thermocouples installed
☐ 13. Diffuser static tap pressure tubes installed
☐ 14. Diffuser exit rakes pressure tubes installed
☐ 15. Turn to axial static taps installed
☐ 16. Deswirl inlet rakes pressure tubes installed
☐ 17. Deswirl exit rakes type T thermocouples installed
☐ 18. Knife seal static taps pressure tubes installed
☐ 19. Backface bleed static taps pressure tubes installed
☐ 20. Capacitance probes installed flush with the flow path
☐ 21. Surface temperature monitoring type T thermocouples installed
☐ 22. Exhaust throttle wired
☐ 23. 3-way valve wired

☐ 24. ETI throttle wired
☐ 25. Secondary tank level sensor wired
☐ 26. Compressor vertical and lateral front bearing accelerometers installed
☐ 27. Compressor vertical and lateral rear bearing accelerometers installed
☐ 28. Gearbox vertical, lateral, and axial accelerometers installed
☐ 29. Surge monitoring pressure sensor installed and wired
☐ 30. Once-per-rev mounted on the compressor inlet

Miscellaneous Test Cell Start Up Checklist

Checklist Rev. Data: 06/20/15

☐ 1. Single test cell door on South side of cell **OPEN & HELD IN PLACE**

☐ 2. Chained enclosure set placed outside

☐ 3. Caps on compressor exhaust pipes **OFF**

☐ 4. Inlet nozzle air filter and wire screen **ON**

☐ 5. Inlet pipe bolts connected and tightened, with gaskets installed

☐ 6. Inlet plenum roll preventers installed and locked in place

☐ 7. Inlet plenum/bellmouth rubber flange installed

☐ 8. Compressor bolts installed and tightened to gearbox

☐ 9. Exhaust bolts installed and tightened to compressor, with gaskets installed

Variable Frequency Drive (VFD) Start-Up Checklist

Checklist Rev. Data: 06/20/15

☐ 1. Control Voltage Disconnect Switch **ON**

☐ 2. Pump selection switch **AUTO**

☐ 3. Pump power **ON**

☐ 4. Reset the emergency stop by pushing the Emergency Stop Reset button (blue LED)

☐ 5. Supply Unit Main Breaker Control **START** (breaker in glass window will close)

☐ 6. Drive Unit Charging Switch **ON**

☐ 7. Drive Unit Disconnection Switch **UNLOCK AND CLOSE**

☐ 8. Drive Unit Charging Switch **OFF**

☐ 9. Liquid coolant outlet temperature (temperature meter at the Supply Unit) **<90°F**

☐ 10. Coolant monitoring type K thermocouple wired at cabinet

Control Stand Start-Up Checklist

Checklist Rev. Data: 06/20/15

☐ 1. Performance data PC **ON**

☐ 2. Health monitoring PC **ON**

☐ 3. Data acquisition power switch **ON**

☐ 4. Agilent measuring units should be powered **ON**

☐ 5. DC power supply **ON**

☐ 6. Performance data LabVIEW program opened

☐ 7. Filename in LabVIEW program set to corresponding date with format YYYYMMDD

☐ 8. # of Data points in the DAQ Control/Monitor tab should be at least 1 (this input determines the number of data points collected when the Collect Data button is selected once the desired operating point is reached).

☐ 9. Health Monitoring LabVIEW program opened

☐ 10. Filename in LabVIEW program set to corresponding date with format YYYYMMDD

☐ 11. Monitor interval input (seconds): 5

☐ 12. Test cell cameras turned on with displays on the secondary oil tank level and the compressor oil flow meters

☐ 13. Controllable test cell camera connected via web browser

☐ 14. Hand spin the compressor and monitor clearances on the capacitance probe cart

☐ 15. Take one manually collected point on the capacitance probe cart. The first point manually recorded includes results from the beginning of the program start which is undesirable for data collection

Final Rig Start-Up Checklist

Checklist Rev. Data: 06/20/15

☐ 1. Final inspection in test cell

☐ 2. Start health monitor DAQ LabVIEW program

☐ 3. Two heat exchanger motor start boxes **HAND**

☐ 4. Scavenge pump **AUTO**

☐ 5. Ejector heating coil plugged in

☐ 6. Ejector **ON**

☐ 7. Boost pump motor starter **HAND**

☐ 8. Gearbox manifold oil pressure should be ≈35 psi

☐ 9. Start performance data LabVIEW program

☐ 10. Start motor by pressing ref, putting brackets around Speed on the list of parameters on the motor controller. Increase initially to a compressor speed of 2000 rpm by pressing the green button

Running Rig Checklist

Checklist Rev. Data: 06/20/15

☐ 1. At 750 RPM, open the 2-way valve to the compressor manifold

☐ 2. Ensure that the manifold pressure reads ≈165 psi

☐ 3. Ensure that the compressor spline, gearbox, and squeeze film lines read ≈75, 40, and 60 psi, respectively

☐ 4. Remain at a compressor speed of 5,000 rpm and turn the heater on until oil temperature is over 105°F

☐ 5. Once this temperature is reached, accelerate to 8000 rpm to avoid shaft mode

☐ 6. Turn off the heater

☐ 7. Ensure that throughout the run the knife seal pressure remains ≈2 psi by using the ETI throttle

☐ 8. Once a data point is collected, collect 10 seconds of data on the capacitance probe cart

Rig Shut Down Checklist

Checklist Rev. Data: 06/20/15

☐ 1. When data collection is completed, decelerate to 50% corrected speed and open the throttle to 100%

☐ 2. Once the compressor speed reaches 750 rpm, turn off the 2-way valve

☐ 3. Bring the compressor to a stop by first slowly reducing the motor speed to 0 rpm.

☐ 4. Once the motor is at 0 rpm, shut the motor down by pushing the red triangle on the motor controller

☐ 5. Allow the boost pump and scavenge pump to run to cool the oil to at least 80°F

☐ 6. Turn the boost pump and scavenge pump motor off

☐ 7. Turn the two heat exchanger motor starts to off

☐ 8. Stop the LabVIEW codes for the performance data and health monitoring data

☐ 9. At the motor drive, Drive 2 Room 114A cabinet, Drive Unit Disconnection Switch **OPEN & LOCKED**

☐ 10. At IGBT Supply Unit cabinet, Pump power switch to off

☐ 11. At IGBT Supply Unit cabinet, Control Voltage Disconnection Switch to off

☐ 12. Instrumentation power switch to off

☐ 13. Turn off the Agilent measurement units

☐ 14. Turn off the power supply

☐ 15. Enter test cell and turn off the ejector

☐ 16. Turn the compressor manual valve **CLOSED**

☐ 17. Unplug the ejector airline heating element

☐ 18. Turn off the DSA air supply and eject the air in the line

☐ 19. Take down enclosure outside of test cell

☐ 20. Check facility for any oil leaks or other damage

☐ 21. Place caps on compressor exhaust pipes

☐ 22. Close all of the doors in the test cell to the outdoors

☐ 23. Email Rob the testing time and let him know that air was used

☐ 24. Post-process the capacitance probe data and shut down the cart